Field-Dependent Magnetic and Transport Properties and Anisotropic Magnetoresistance in Ceramic $La_{0.67}Pb_{0.33}MnO_3$

by

Amra Peles

A Thesis
Submitted to the Faculty of Graduate Studies
in Partial Fulfillment of the Requirements
for the Degree of

MASTER of SCIENCE

Department of Physics and Astronomy
University of Manitoba
Winnipeg, Manitoba

THE UNIVERSITY OF MANITOBA

FACULTY OF GRADUATE STUDIES

*****

COPYRIGHT PERMISSION PAGE

Field-Dependent Magnetic and Transport Properties and Anisotropic Magnetoresistance in Ceramic $La_{0.67}Pb_{0.33}MnO_3$

BY

Amra Peles

A Thesis/Practicum submitted to the Faculty of Graduate Studies of The University of Manitoba in partial fulfillment of the requirements of the degree

of

Master of Science

Abstract

Detailed measurements of the field and temperature dependence of the ac susceptibility, magnetization and the transverse and longitudinal magnetoresistivities of ceramic $La_{0.67}Pb_{0.33}MnO_3$ has been made, and are presented. Detailed analysis of the magnetic data provide an estimate of 340.5 $\pm$ 0.5 K for the paramagnetic to ferromagnetic temperature T_c, with data closest to the critical point yielding the set of critical exponent values i.e. $\gamma = 1.39 \pm 0.06$, $\beta = 0.41 \pm 0.2$ and $\delta = 4.20 \pm 0.15$. The presence of disorder, that is, a variance in the distribution of spin - spin coupling strength, means that Heisenberg model asymptotic exponents cannot be excluded; the universality class for this system cannot therefore be definitely identified.

The transport data yield $T_c = 339.6 \pm 0.4$ K, and while the isotropic magnetoresistance peaks near T_c, as expected, the magnitude of the spontaneous resistive anisotropy (SRA) increases linearly with decreasing temperature below T_c, peaks near 30 K, and then falls to a smaller value (-0.2 $\pm$ 0.03 %) in the liquid helium temperature region. The latter value is in reasonable agreement with itinerant model predictions, while the temperature variation in the SRA above about 30 K is more convincingly reproduced by a localized model. Furthermore, the mechanism controlling the isotropic magnetoresistance and the SRA in this system appear to be different.

Contents

List of Figures

List of Tables

Acknowledgements

I want to express my deepest appreciation to my advisor, Dr. Gwyn Williams for his permanent guidance, counsel and support during the course of this work. As well, I would like to thank my committee members, Dr. R. Roshko and Dr. A. Chow. I would like to thank Dr. H.P. Kunkel and Dr. X.Z. Zhou for their assistance with various area of my research.

Chapter 1

Introduction

In the early 1950s Jonker and van Santen synthesized and characterized [1] a series of compounds with the general formula $T_{1-x}A_xMnO_3$ where T is a trivalent and A is a divalent ion. These compounds form in the perovskite structure, $CaTiO_3$. Certain compositions of doped manganites ($0.2 \leq x \leq 0.5$) exhibit both a paramagnetic to ferromagnetic and a metal-insulator transition at the same temperature. The basic theoretical ideas to describe these systems were developed by Zener (1951), Anderson and Hasegawa (1955), and de Gennes (1960). Recently, interest in these materials has been renewed as result of their displaying a "Colossal Magnetoresistance" (CMR) i.e. a large fractional change between zero-field $\rho(0)$ and finite field $\rho(H)$ resistivity. These rather unusual magnetic and transport properties had been initially explained by a double exchange mechanism linked to the presence of an inhomogeneous mixed valence state (Mn^{3+}/Mn^{4+}) where holes at the tetravalent Mn site become mobile

and hopping of such holes between nearest neighbour Mn sites becomes possible for $x \geq 0.1$. However, recently it was shown that double exchange theory alone cannot explain the physical properties of these perovskites as they depend on a strong interplay of charge, spin, orbital and lattice degrees of freedom. It is presently believed that the metal-insulator transition and CMR in these compounds are caused by a combination of the double exchange interaction between ferromagnetically coupled Mn^{3+} and Mn^{4+} ions and Jahn-Teller effects, involving a lattice distortion associated with the differing ionic size of the dopant (static Jahn-Teller effect) and a coupling of charge carriers and vibration of the crystal lattice (dynamic Jahn-Teller effect).

In present study we are particularly interested in the critical phenomena, or the thermodynamic behaviour of a system in the vicinity of the critical temperature at which it undergoes a continuous phase transition. Attempts to understand systems of interacting magnetic moments lead to the development of various models which allow calculation of the exact values of critical exponents describing the asymptotic behaviour of the thermodynamic variables in the vicinity of the critical point. Besides models which predict exact values for critical exponents, a second approach, concerned more with the functional form of a free-energy of the system or with the equation of state, was introduced for better understanding critical phenomena. This approach is known as the static scaling hypothesis or homogeneous function approach. It predicts relationships amongst the critical exponents and also provides insights into possible forms for the magnetic equation of state.

The similarities that often exist between critical exponents describing seemingly very different systems and supported with a huge number of empirical examples lead to the formulation of the Universality hypothesis. This hypothesis states that the critical behaviour of a system depends only on the spatial dimensionality of the system and dimensionality of the order parameter (in the case of a magnetic transition, a spin space dimensionality), so that each system with the same critical exponents can be assigned to a particular universality class.

The other main concerns of the present study are transport properties and the magnetoresistive anisotropy. Traditionally the basic transport properties of magnetic materials were explained by the existence of an exchange interaction between the magnetic moments or spins of conduction electrons and magnetic atoms, of the simple form, $J\vec{\sigma} \cdot \vec{S}$. The existence of a magnetoresistive anisotropy requires a non zero orbital moment present at the magnetic site, and consequently the presence of spin-orbit coupling, which is qualitatively expected for Mn^{3+} ions in the perovskites. Two different models attempt to describe the anisotropic magnetoresistivity. One is based on an itinerant picture, the so-called two current model, and the other, a localized model, is based on the picture of the magnetic moments localized at lattice sites.

The present study was motivated by both technological considerations,since the properties of the manganites appear useful in a variety of field sensing applications, and by interest in the fundamental processes underlying these phenomena. This thesis assembles the experimental results of the investigation of the critical behaviour at

the magnetic phase transition, the transport properties and anisotropic magnetoresistance of a $La_{0.33}Pb_{0.67}MnO_3$ compound. The purpose of this work was to examine the magnetic transition, the nature of which in general is not fully understood in the manganites. Moreover, a study of critical phenomena in these materials is of interest as the double exchange interaction responsible for ferromagnetic order in the manganites depends on $\cos(\theta/2)$, as opposed to the Heisenberg exchange interaction which depends on $\cos(\theta)$ and is responsible for ferromagnetic order in conventional magnetic materials (θ is the angle between the directions of the ionic spins). This, presumably, may result in different critical exponents for double exchange ferromagnets [50].

The review of the properties of the perovskites and relevant background material is discussed in more detail in the following two chapters. The experimental details, including a description of sample preparation techniques, a description of the experimental apparatus used and the measurement methods and procedures are summarized in chapter 4. The data and their analysis are presented in chapter 5, together with a discussion and comparison with existing measurements and results. Concluding remarks on the present work on $La_{0.33}Pb_{0.67}MnO_3$ are presented in chapter 6.

Chapter 2

Introduction to the Properties of the Perovskites

Much recent research effort has been put into investigating doped lanthanum manganites, $La_{1-x}A_xMnO_3$, where A is a divalent ion, such as Ca, Sr, Ba, Pb, etc. [2, 3]. In the interesting doping range $0.2 \leq x \leq 0.5$ these materials exhibit a phase transition from a high-temperature paramagnetic insulator to a low-temperature poorly conducting ferromagnet [1]. Furthermore, these materials exhibit "Colossal Magneto Resistance" (CMR), that is, the application of a magnetic field causes a dramatic decrease in the resistivity close to the transition. The observed CMR is an attractive feature for technology. These compounds may have several potential applications, in particular near $x \sim 0.3$ these systems behave as half metallic ferro-magnets in which the conduction process is accomplished within a completely spin polarized band [4],

thus raising the possibility of fabricating devices based on spin - rather then charge - transport. These perovskites also provide an interesting possibility for studying the fundamental behavior of strongly correlated electronic systems.

2.1 Double Exchange

The correlation between the resistivity and the magnetization in these compounds was originally explained by "double exchange" theory (DE) [5, 6, 7]. The double exchange approach suggests that the mechanism of electronic spin interaction is responsible for the ferromagnetic order observed in mixed-valency (Mn^{4+}/Mn^{3+}) manganites with a perovskite structure, allowing hopping of the electrons between neighbouring ionic sites. This model assumes that the exchange coupling between carrier spins and "ionic" spins is so strong that the only important configuration is that where the spin of each carrier is parallel to the local ionic spin . Furthermore, the carriers do not change their spin orientation during hopping; consequently the possibility of carrier hopping from one ionic site to another is non-zero only if the two ionic spins are parallel. Thus the increase in kinetic energy accompanying carrier delocalization in the "metallic" state is compensated by the free energy decrease accompanying the establishment of magnetic order - in this case, ferromagnetic order. In a simplified model [7] the hopping can be described by the so called transfer integral t_{ij} between ions situated on site (i) and (j). t_{ij} represents a matrix element of the one carrier

Hamiltonian and is given as follows,

$$t_{ij} = \langle \varphi_i | H | \varphi_j \rangle \,. \tag{2.1}$$

Here the φ's are elements of a set of the orthogonal functions $\{\varphi_i\}$ localized on each magnetic site (i). The transfer integral connects only neighbouring magnetic sites. It has a maximum value equal to some constant b_{ij} when spins $\mathbf{S}_i$ and $\mathbf{S}_j$ are parallel. For an antiparallel configuration of neigbouring spins $\mathbf{S}_i$ and $\mathbf{S}_j$, the transfer integral t_{ij} is zero. More generally, for carriers of spin 1/2, t_{ij} can be expressed as [6]

$$t_{ij} = b_{ij} \cos(\frac{\theta_{ij}}{2}) \tag{2.2}$$

where θ_{ij} is the angle between $\mathbf{S}_i$ and $\mathbf{S}_j$. This approach assumes that ions are localized at their equilibrium positions, and neglects any coupling between carriers and lattice vibrations as well as the fivefold degeneracy of the Mn d levels. Later developments of models based on the double exchange mechanism consider some of these effects, giving a microscopic picture of these processes and attempt to provide better understanding of these manganese perovskites. The parent compound $LaMnO_3$ is an anti-ferromagnetic insulator [8]. It contains Mn^{3+} ions with four electrons in the outermost 3d energy levels. The crystal field, with octahedral local symmetry, splits the five 3d levels into three low energy t_{2g} orbitals and two higher energy e_g orbitals. The latter can overlap strongly with oxygen p orbitals, this overlap being controlled by the angle of the Mn-O-Mn bond, which is a maximum (180^0) in the ideal (undistorted) perovskite structure. The strong crystal field splitting of levels and the

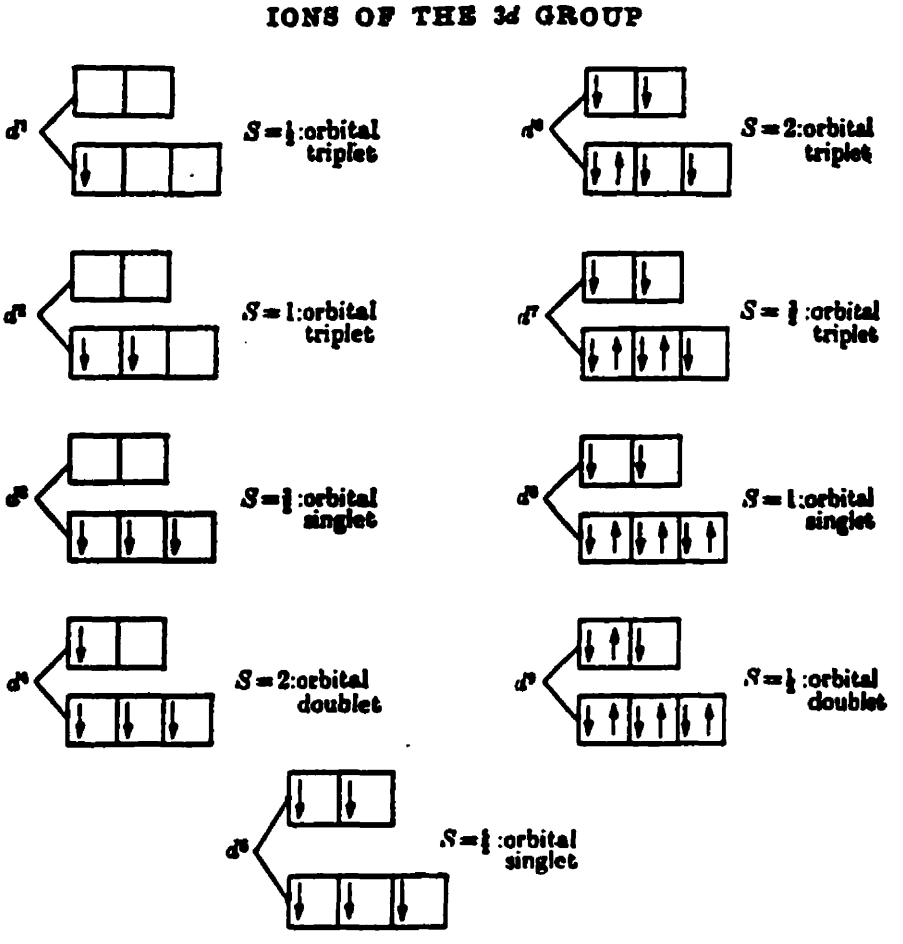

Figure 2.1: Construction of the ground states of the d-configurations in an octahedral field using the strong crystal field approach, but assuming a spin coupling to be stronger than the crystal field energy [9].

ground states of the d-configuration for various spins are presented in figure (2.1). In constructing a ground state, besides minimizing the crystal field energy, Hund's rule coupling between the electron spins must be considered. The latter requires the ground state configuration be one of maximum possible spin. Assuming that the spin coupling energy is larger than the crystal field energy, then only three electrons can be placed in t_{2g} orbitals with parallel spin because of the exclusion principle, while

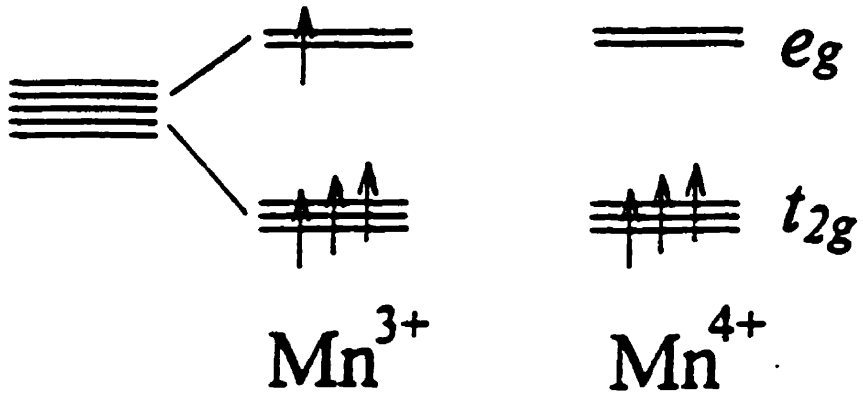

Figure 2.2: The schematic representation of the electronic states of Mn^{3+} and Mn^{4+} ions [10].

orbitals can be occupied with up to two electrons, with spins parallel to the t_{2g} spins [9]. Consequently, in the case of the manganites, the on-site Coulomb repulsion is strong enough that each orbital is occupied by only one electron, and the large Hund's rule coupling aligns all spins of a single Mn ion parallel. Thus three Mn^{3+} electrons fill up the t_{2g} orbitals, forming an electrically inert "core" of spin $S = 3/2$ while the remaining e_g electron is aligned parallel to the core state by the strong Hund's rule coupling. The substitution of trivalent La ions by divalent alkaline earths, of the type indicated above, convert proportional numbers of Mn^{3+} (t_{2g}^3, e_g^1) into Mn^{4+} (t_{2g}^3, e_g^0) ions to ensure charge neutrality. The schematic representation of the electronic states of Mn^{3+} and Mn^{4+} ions are given in figure (2.2).

The creation of the holes at Mn^{4+} ion sites changes the character of the outer-shell

e_g electrons as these electrons become itinerant beyond $x \simeq 0.1$, allowing hopping along Mn-O-Mn bonds, due presumably to the emergence of a Mn e_g-O(2p) band near this composition. Because of the large Hund's rule coupling this hopping of the e_g electrons is affected by the relative alignment of the core spins on the neighbouring sites, being maximal when core spins are parallel and minimal when they are antiparallel. The latter can be quantitatively described by an effective transfer integral, which depends on the angle between spins on neigbouring sites (eq:2.2), as was discussed previously. As a consequence, motion of the electrically active e_g electrons spin polarize the localized Mn core spins, leading to the ferromagnetic order. In such a physical scheme it is clear that the application of a magnetic field enhances carrier mobility by reducing spin disorder, especially near T_c, giving a qualitative explanation of the observed CMR. A naive explanation of CMR in terms of the double exchange interaction is depicted in figure (2.3). The random spin distribution in the paramagnetic state in a zero applied field and a strong Hund's rule coupling prevent e_g electrons from hopping to neighbouring vacant e_g sites. However the application of magnetic fields strong enough to align the localized "core" spins parallel to each others allows a hopping of e_g electrons without violating the Hund's rule coupling. Thus the "double exchange" mechanism accounts qualitatively for ferromagnetic ordering and enhanced carrier mobility.

Historically, the concept of the DE interaction was introduced by Zener [5]. In order to explain ferromagnetism in the metallic region in manganites $La_{1-x}A_xMnO_3$ Zener

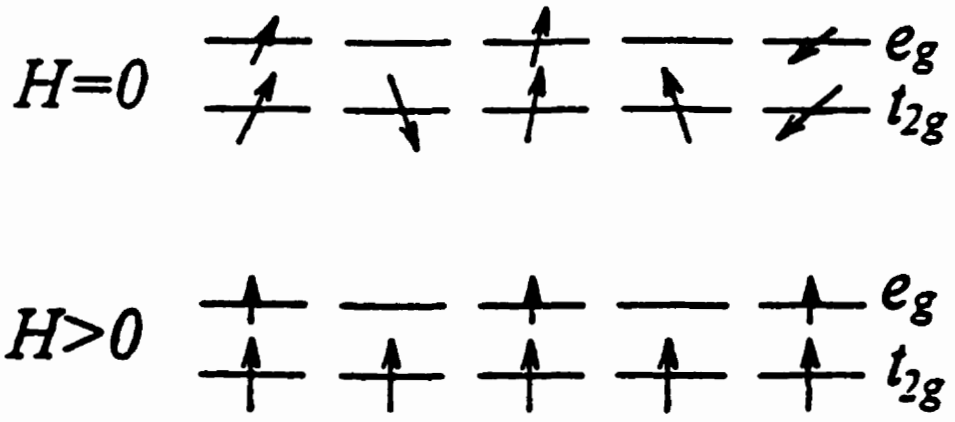

Figure 2.3: The naive explanation of the CMR effect in terms of the double exchange interaction [10].

considered a Hamiltonian of the form

$$H = -\sum_{i,j,\sigma} t_{ij}(a^{+}_{i\sigma}a_{j\sigma} + h.c.) - J_H \sum_{i} \vec{\sigma}_i \vec{S}_i \tag{2.3}$$

with strong Hund's rule coupling i.e. $J_H \gg t$. Here J_H is a ferromagnetic spin exchange between e_g and t_{2g} electrons (Hund's coupling) and t_{ij} is the electronic hopping coupling. In manganites, the Hund's coupling J_H is estimated to be a few eV and the electron hopping t is estimated at about 0.1 eV. Anderson and Hasegawa [6] introduced an effective Hamiltonian for the limiting case $J_H \to \infty$ given as

$$H = -\sum_{i,j} t(\vec{S}_i \vec{S}_j)(\tilde{a}^{\dagger}_i \tilde{a}_j + h.c.) \tag{2.4}$$

In the limit $JS \rightarrow \infty$ the effective Hamiltonian can be written as

$$H = -t \sum_{i,j} \cos(\frac{\theta_{ij}}{2}) a_i^+ a_j \tag{2.5}$$

giving a dependence of the hopping matrix element on the half angle $(\theta_{ij}/2)$ between spins localized on site (i) and (j), given in expression (2.2) and discussed previously. These models give a qualitative explanation of the coexistence of ferromagnetism and metallic conduction in these perovskites. However a detailed analysis shows that the increase in resistivity due to electron scattering by disordered spins in the paramagnetic phase is not sufficient to explain the insulating behavior of these perovskites, nor is the observed correlation between the magnetoresistance and the magnetization accounted for. In addition to "double exchange", other degrees of freedom should be included for a better understanding of the phenomena exhibited by these materials, such as the dynamic Jahn-Teller interaction, an orbital degree of freedom, and superexchange interactions. Next the coupling between the crystal lattice and the electrons is discussed. These include effects caused by the different ionic size of dopants (a static Jahn-Teller effect) and those due to the coupling of electrons and lattice vibrations (the dynamic Jahn-Teller effect), both of which are summarized in next section.

2.2 Electron-Lattice Coupling

There are two different kinds of electron-lattice coupling that affect carrier mobility. One involves changes in the angle of the Mn-O-Mn bond when lanthanum is replaced by a smaller ion. This introduces internal stress and buckling of the Mn-O-Mn bond, and such changes in bond angle decrease the overlap of orbitals and narrows the energy band for conduction electrons. This effect can be described quantitatively by the "tolerance factor" (t), a quantity which is equal to unity for ideal perovskite structures though for most of these perovskites $t \leq 1$, indicating a deviation from the ideal structure. The tolerance factor is defined as

$$t = (r_A + r_O)/\sqrt{2}(r_B + r_O). \tag{2.6}$$

Here r_A, r_B and r_O denote respectively the radii of La or A, Mn, and O ions, the specific crystallographic positions of which are depicted in figure (2.4). The second form of coupling is that between charge carriers and the vibration of the crystal lattice. This links the instantaneous deviation of the atoms from their ideal crystallographic positions to the instantaneous deviations of the electron configurations from their average values [11]. Of particular importance is Jahn-Teller lattice distortion and splitting of the energy levels due to vibration of oxygen ions, as indicated in figure (2.4). Such a lattice distortion lowers the orbital energy (when the e_g state is occupied by an electron), and if the electron-phonon coupling is strong enough it tends to localize the carriers by trapping electrons in the low energy orbitals. This self-

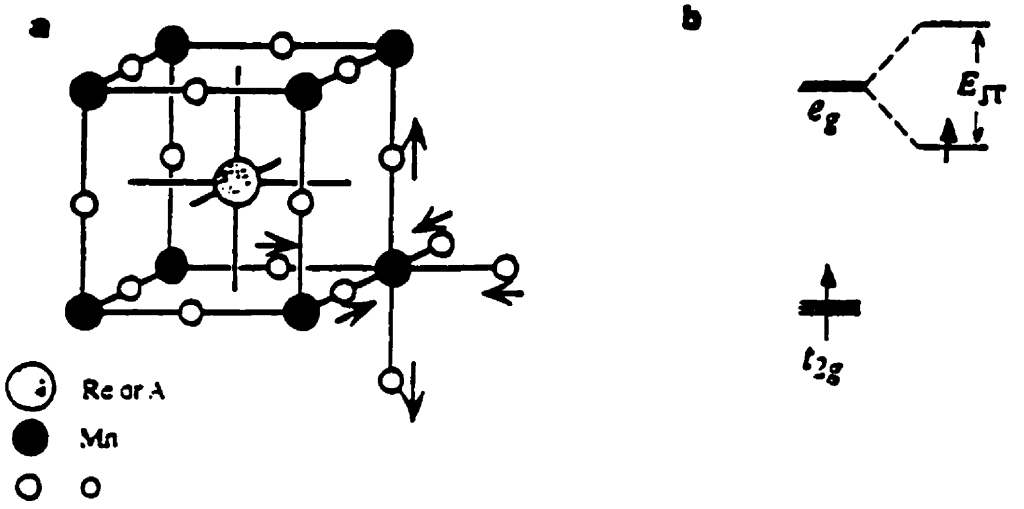

Figure 2.4: Crystal structure and electronic structure of manganite perovskite. a.The basic perovskite structure, with oxygen motions in one Jahn-Teller distortion indicated by arrows. b.Schematic energy levels of the Mn ion. Left-hand portion correspond to the undistorted lattice; it shows the low-lying t_{2g} levels occupied by three parallel-spin electrons forming a $S_c = 3/2$ core spin, and a higher-lying doubly degenerate e_g level. The right-hand portion shows a splitting of the doublet by an energy E_{JT} caused by Jahn-Teller distortion of the surrounding O_6 octahedron (see a.) for a singly occupied e_g level [11].

trapped state is called a "polaron" and is believed to be present only above T_c. Below T_c self-trapping disappears due to growing ferromagnetic order and the electrons are much more mobile.

Much recent work on these doped perovskites has concentrated on Ca substitution. This has resulted in the publication of a comprehensive phase diagram for this system (fig:2.5), which exhibits rich structure as a function of both Ca composition x and temperature T [12, 13]. Indeed, the term "optimal doping" was first applied to this system, a consequence of the ferromagnetic ordering temperature T_c peaking (at about 250 K) close to $x \simeq 1/3$. In the present work measurements on a ceramic sample doped with Pb at $x \simeq 1/3$ are reported. These measurements include field - and temperature - dependent magnetic and transport measurements as well as anisotropic magnetoresistance studies. The measured sample exhibits a ferromagnetic-to-paramagnetic transition accompanied by a metal-to-insulator transition. The result of such measurements and a discussion of results and their analysis will be presented in the following sections.

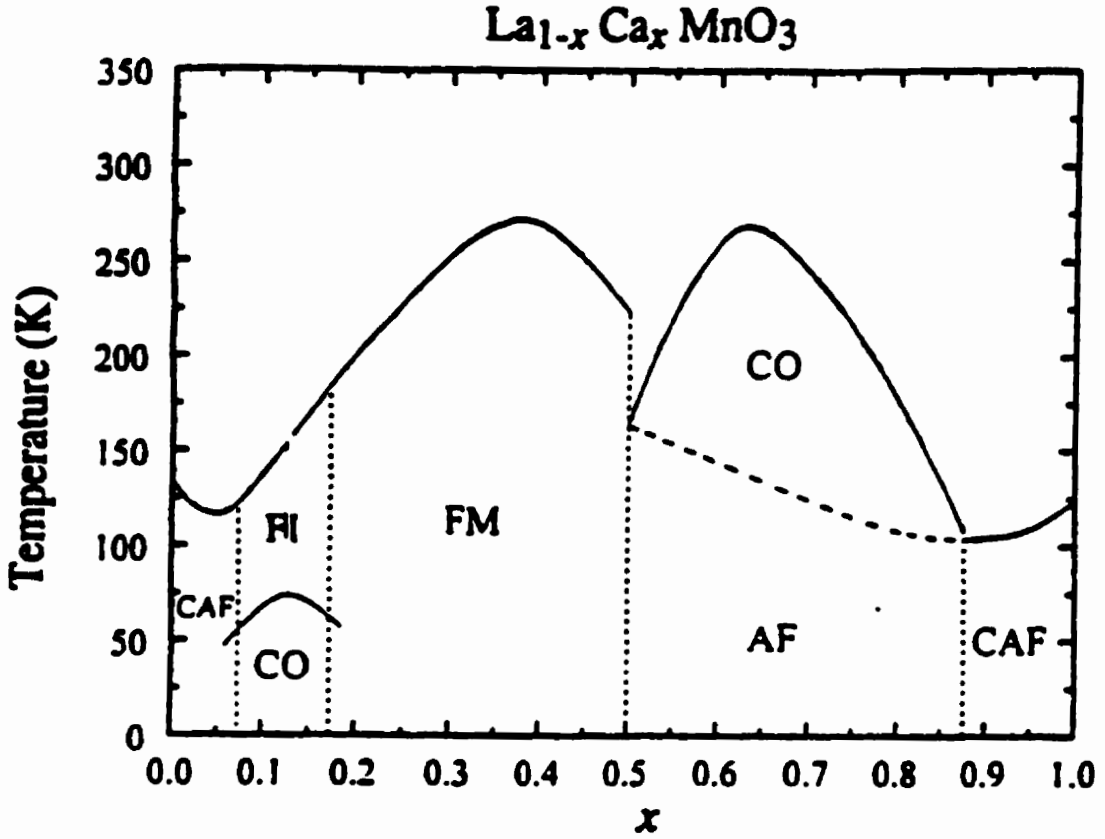

Figure 2.5: Phase diagram of $La_{1-x}Ca_xMnO_3$ showing magnetic and structural phase boundaries. Phases include charge-ordered (CO), antiferromagnet (AF), canted antiferromagnet (CAF), ferromagnetic metal (FM), ferromagnetic insulator (FI).

Chapter 3

Theoretical Background:

Magnetic and Transport Behaviour

3.1 Magnetic Ordering and Phase Transition

The orientation of permanent magnetic moments localized on the atomic (ionic) sites results in different overall magnetic moment (magnetization) and different kinds of magnetic order in various systems, reflecting differences in the underlying interactions between such moments.

When magnetic moments are randomly oriented due to thermal fluctuation, resulting in zero net magnetization, the material is said to be paramagnetic. However on cooling all materials exhibit long range order of their magnetic moments due to their mutual interactions. In ferro-magnets these moments are aligned parallel to

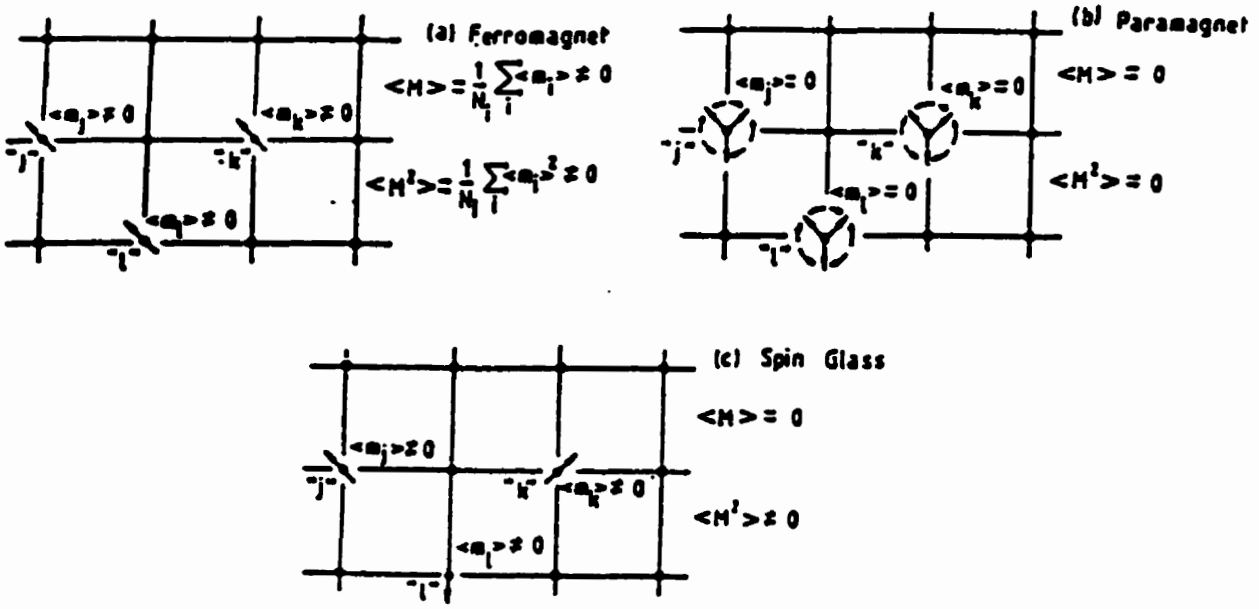

Figure 3.1: An illustration of the difference between a. a ferromagnet below T_c b. a paramagnet and c. a spin glass below T_{sg} [14].

each other on passing below a critical temperature T_c, resulting in a non zero (spontaneous) magnetization (at least within a single domain), while in antiferomagnets moments are aligned anti-parallel and the net magnetization is zero. Figure (3.1) gives an illustration of different kinds of magnetic order.

3.1.1 Order Parameter

The change in magnetic state through the critical point is often referred to as a critical phase transition. In fact, these transitions are called continuous when

they do not involve a latent heat. Transitions from ordered to disordered states are characterized by an order parameter, a quantity whose thermal average vanishes in the disordered phase above the transition and has a non zero value in the ordered region below the transition. In the case of a ferromagnetic-to-paramagnetic transition, the conventional order parameter is the zero field spontaneous magnetization, which is a continuous function of temperature, changing from a non zero value for $T < T_c$ and falling to zero at T_c, remaining zero for $T > T_c$.

3.2 Critical Point Exponents

The basic problem in the theory of phase transitions is to study the behavior of a given physical system in the neighbourhood of the critical point. Many experimental results suggest that measurable quantities such as the susceptibility, the specific heat, or the correlation length, in fact, "diverge" (in the sense of anomalous fluctuations of the order parameter) at the critical point, often obeying simple power laws near the phase transition. Critical exponents are a set of indices which describe the singular behaviour of such quantities in the neighbourhood of the transition.

3.2.1 Definition of Critical Point Exponents

The assumed power law behaviour of an arbitrary state function near a critical point $x = 0$ usually may be represented by a general function [15]

$$f(x) = Ax^{\lambda}(1 + a_y x^y + \ldots), \quad y > 0. \tag{3.1}$$

Here λ is a critical point exponent and the added polynomial represents correction terms. The correction terms limit the range of x over which a simple power law holds and often reduce the accuracy with which critical point exponents can be determined experimentally.

The exponent λ is defined by the asymptotic behaviour, i.e. close to the critical point, namely

$$\lambda = \lim_{x \to 0^+} \frac{\ln f(x)}{\ln x} \tag{3.2}$$

and,

$$\lambda' = \lim_{x \to 0^-} \frac{\ln f(x)}{\ln x} \tag{3.3}$$

when the critical point $x = 0$ is approached from the positive (+) or the negative (-) side respectively. The two exponents λ and λ' are not necessarily equal; however theory and experimental evidence suggest that in many cases they are. In the analysis of magnetic phase transitions the argument of the general function f is a dimensionless variable, usually involving the reduced temperature t, defined as $t = (T - T_c)/T_c$, or magnetic field $h \sim H/T_c$.

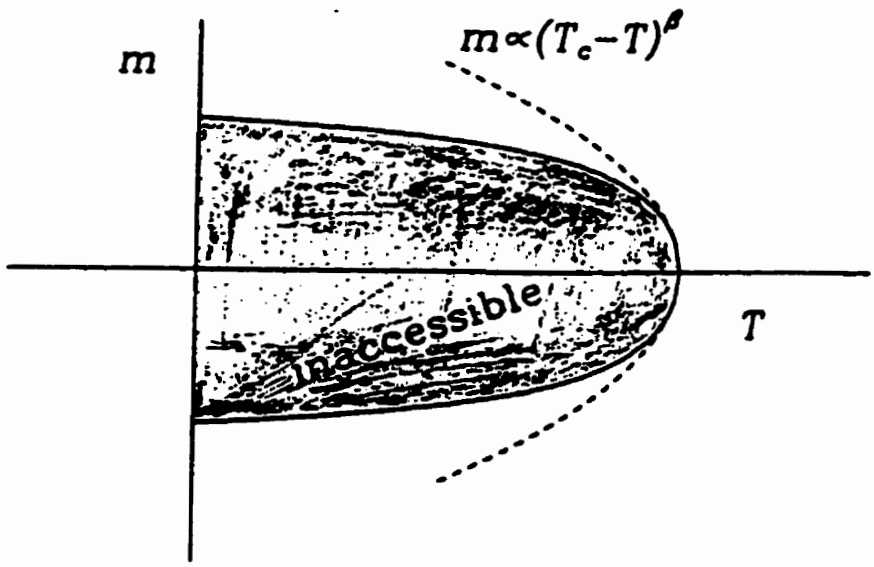

Figure 3.2: Definition of the critical exponent β.

Zero-field magnetic exponent β

The exponent β describes how the magnetization in zero applied field varies with temperature immediately below T_c, i.e. the spontaneous magnetization $m(t)$, as shown in figure (3.2), varies as $(T_c - T)^\beta$ when T_c is approached from below; thus while $m(t \to 0) \to 0$, its slope changes discontinuously at $T = T_c$ $(t = 0)$. While it is clear that a state of higher magnetization can be achieved by applying an external magnetic field below T_c, states inside the shaded region of the $M - T$ plane in the phase diagram of figure (3.2) are inaccessible. Referring to the general function and the definition of critical point exponents, the spontaneous magnetization and its

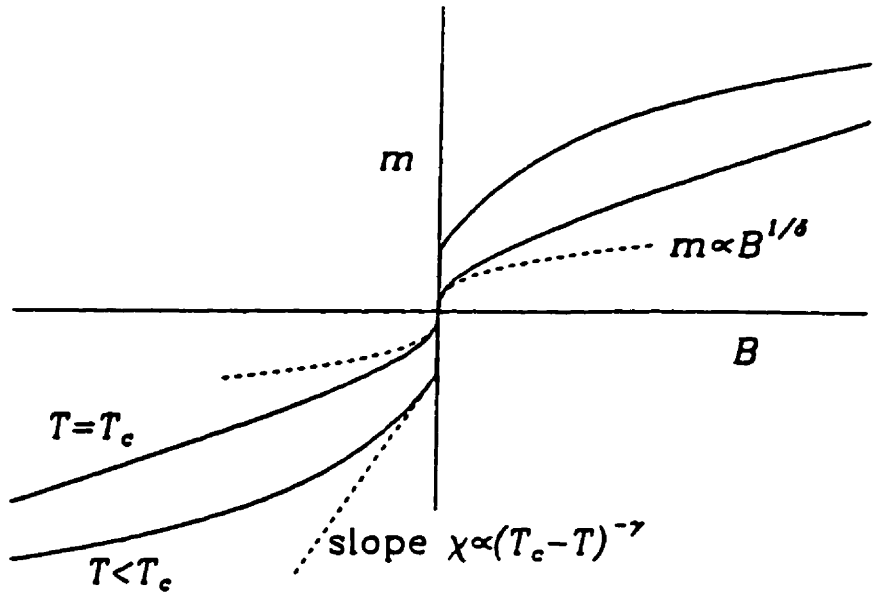

Figure 3.3: Definition of the critical exponents γ and δ.

associated critical exponent β are given as,

$$\frac{M(T)}{M_0(T)} = B(-t)^{\beta}(1 + \ldots) \qquad T \leq T_c \tag{3.4}$$

and,

$$\beta = \lim_{t \to 0^-} \frac{\ln M(T)}{\ln(-t)}. \tag{3.5}$$

Isothermal magnetic susceptibility exponent γ

The critical exponent γ describes the singular behaviour of the magnetic susceptibility near the critical point. The susceptibility near the critical point in the limit of a small magnetic field is given by

$$\chi = \left(\frac{\partial M}{\partial H}\right)_T \sim (T - T_c)^{(-\gamma)} \tag{3.6}$$

which is the slope of the isotherm "$T < T_c$" in figure (3.3). The susceptibility diverges when the critical point is approached from the low or the high temperature side according to the following power law,

$$\frac{\chi(T)}{\chi_0(T)} = \begin{cases} C'(-t)^{-\gamma'}(1+\ldots) & T < T_c, H = 0 \\ C(t)^{-\gamma}(1+\ldots) & T > T_c, H = 0 \end{cases} \tag{3.7}$$

Critical isotherm exponent δ

The critical isotherm in figure (3.3) indicates that the magnetization at T_c has a nonlinear behaviour for small applied fields. This variation of magnetization with small fields at T_c is described by critical point exponent δ, viz

$$M \sim H^{\frac{1}{\delta}}, \quad H \to 0, \quad T = T_c \tag{3.8}$$

Specific heat critical exponent α

The specific heat, like the magnetic susceptibility, exhibits a divergence at the critical point. The specific heat C_H at constant field H is given by

$$C_H = \begin{cases} A'(-t)^{-\alpha'}(1+\ldots) & T < T_c \\ A(t)^{-\alpha}(1+\ldots) & T > T_c \end{cases} \tag{3.9}$$

The exponents α and α' are both positive, and vanishingly small α's imply a logarithmic rather than an algebraic singularity. Power law behavior and the definitions of associated critical point exponents of the different quantities are summarized in table (3.1).

3.2.2 Inequality Relationship among Critical Exponents

Inequality relationships among critical-point exponents may be derived by consideration of thermodynamic stability and statistical physics. For example, the specific heat of magnets and the isothermal susceptibility are related by the equation, [15]

$$\chi_T(C_H - C_M) = T\left(\frac{\partial M}{\partial T}\right)_H^2 \tag{3.10}$$

C_H and C_M are the specific heats at constant applied field and magnetization, respectively. Thermodynamic stability requires that χ_T, C_H, C_M all be greater than or equal to zero [16]. Then,

$$C_H > T\chi_T^{-1}\left(\frac{\partial M}{\partial T}\right)_H^2 \tag{3.11}$$

when $T \to T_c^-$; χ_T, and C_H obeys the power laws given in table (3.1), so that

$$(T_c - T)^{-\alpha'} > const.(T_c - T)^{\gamma'+2(\beta-1)} \tag{3.12}$$

which leads to the Rushbrooke inequality

$$\alpha' + 2\beta + \gamma' \geq 2. \tag{3.13}$$

Other inequalities can be derived, some of which are summarized as follows

$$\alpha' + \beta(1+\delta) \geq 2 \qquad \text{(Griffiths)}; \tag{3.14}$$

$$\gamma' \geq \beta(\delta - 1) \qquad \text{(Widom)}, \tag{3.15}$$

$$(2 - \eta)\nu \geq \gamma \qquad \text{(Fisher)}. \tag{3.16}$$

Exponent Definition	Condition	Quantity
$M \sim (-t)^{\beta}$	$t \to 0^-, H = 0, M \neq 0$	zero-field magnetization
$\chi_T \sim t^{-\gamma}$	$t \to 0^+, H = 0, M \neq 0$	zero-field isothermal susceptibility
$\chi_T \sim t^{\gamma}$	$t \to 0^-, H = 0, M = 0$	zero-field isothermal susceptibility
$M \sim H^{\frac{1}{\delta}}$	$t = 0, H \neq 0, M \neq 0$	critical isotherm
$C_H \sim t^{-\alpha'}$	$t \to 0^-, H = 0, M \neq 0$	specific heat at constant magnetic field
$C_H \sim t^{-\alpha}$	$t \to 0^+, H = 0, M = 0$	specific heat at constant magnetic field

Table 3.1: Critical-point exponent definitions for magnetic system.

3.3 Mean Field Theory

3.3.1 Classical Mean Field Approach

Mean field theory (MFT) gives a qualitative description of physical systems and phenomena of interest. Historically, the classical mean field method was introduced by Weiss and was the first and only theory of phase transitions for a considerable time. Classical MFT is a phenomenological approach in which the strong interactions that tend to align magnetic moments parallel to each other are represented by an internal molecular field, proportional to the order parameter, namely

$$H_m = \lambda M(T, H) \tag{3.17}$$

Here the proportionality constant λ is referred to as the molecular field constant. An estimate of the molecular field yields $H_m \sim 10^7$ Oe and gives an indication of the strength of coupling between magnetic moments in ferromagnets[17]. The effective or total field acting upon each magnetic dipole in the presence of an applied external field H_a is then

$$H_{eff} = H_a + \lambda M(T, H). \tag{3.18}$$

The effects of dipole - dipole and demagnetizing fields are usually small compared to the molecular field and are neglected. The Hamiltonian of an N - atom interacting system can thus be replaced by an N - atom non - interacting system in an external

effective field, and is given by

$$H = -g\mu_B \sum_{i=1}^{N} \mathbf{J}_i \cdot \mathbf{H}_{eff} \tag{3.19}$$

where J_i is the total magnetic moment of the i-th atom. Using the above equation one can determine the partition function Z, defined to be,

$$Z = \sum_i e^{\frac{E_i}{kT}}, \tag{3.20}$$

and the related Gibbs potential,

$$G(T, H) = kT \ln Z. \tag{3.21}$$

The magnetization is related to the Gibbs free energy by

$$M(T, H) = -\left(\frac{\partial G}{\partial H}\right)_T \tag{3.22}$$

which can be expressed as

$$M(T, H) = NkT\frac{\partial \ln Z}{\partial H_{eff}} = M_0 B_J\left[\left(\frac{g\mu_B J}{kT}\right)(H_a + \lambda M(T, H))\right] \tag{3.23}$$

where M_0 is the magnetization of completely aligned magnetic moments i.e. the maximum value of the spontaneous magnetization,

$$M_0 \equiv M(T = 0, H = 0) = NJg\mu_B \tag{3.24}$$

and $B_J(x)$ is the Brillouin function, defined as

$$B_J(x) = \frac{2J+1}{2J}\coth\left(\frac{2J+1}{2J}x\right) - \frac{1}{2J}\coth\left(\frac{1}{2J}x\right) \tag{3.25}$$

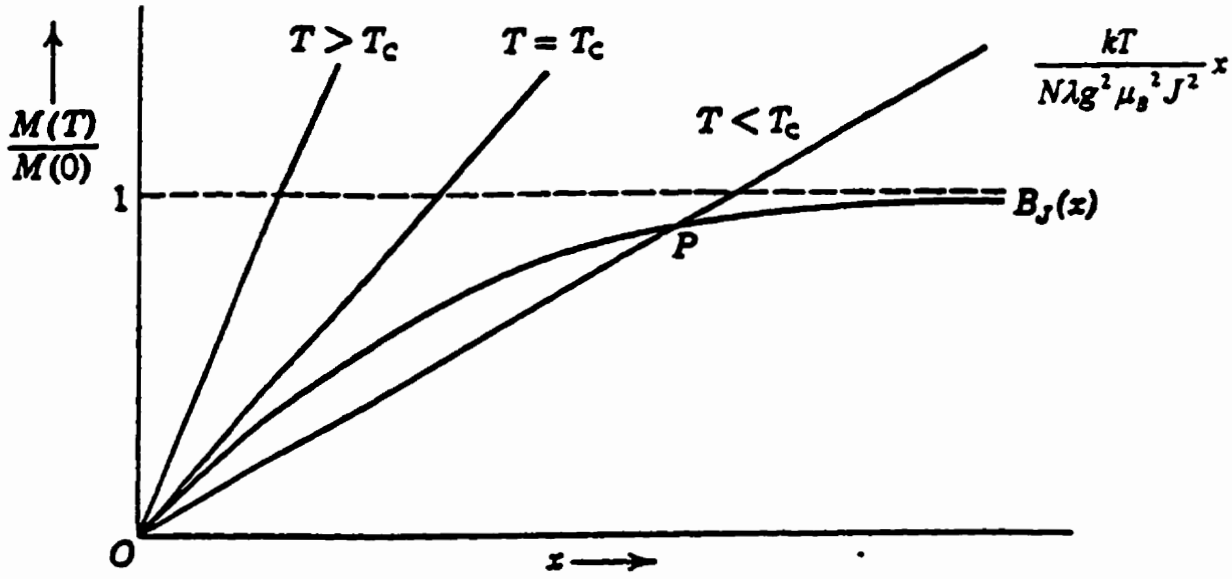

Figure 3.4: Illustration of a graphical method for the determination of the spontaneous magnetization at temperature T. The plotted straight lines (eq:3.26) illustrate a nature of the results for different temperatures.

with

$$x = \frac{g\mu_B J H_{eff}}{kT} \tag{3.26}$$

The Brillouin function is an explicit function of the magnetization, so that it is possible to find a graphical solution for equation (3.23). A trivial solution $M = 0$ exists for all temperatures T, and there is also a non zero solution for $T < T_c$, as depicted in figure(3.4). The solution $M = 0$ for $T < T_c$ does not have a real physical meaning, while the solution $M \neq 0$ represents the stable state, indicating the existence of a spontaneous magnetization for $T < T_c$. At $T = T_c$ a transition occurs and the magnetization disappears above T_c. For small argument x, i.e. when

the magnetization is small, the Brillouin function can be expanded and becomes

$$B_J(x) = \frac{J+1}{3J}x - \frac{J+1}{3J}\ \frac{2J^2+2J+1}{30J^2}x^3 \qquad (x \ll 1) \tag{3.27}$$

In the limit $x \to 0$, the initial slope of the Brillouin function approaches $(J+1/3J)$ which is equal to the slope of the straight line for $T = T_c$ (eq:3.26) plotted in the figure (3.4). Equating these two slopes provides a connection between T_c and the molecular field constant λ, namely,

$$T_c = \frac{Ng^2\mu_B^2 J(J+1)}{3k}\lambda = C\lambda. \tag{3.28}$$

C is known as the Curie constant. T_c is proportional to the molecular field constant λ and when $\lambda = 0, T_c = 0$ corresponding to a non-interacting, paramagnetic system. In the paramagnetic region, classical MFT leads to the so called Curie-Weiss law, namely,

$$\chi = \frac{C}{T-\Theta} \tag{3.29}$$

in which T_c and Θ are equivalent.

3.3.2 Critical Point Exponents for MFT

In the limit $T \to T_c$ from below, the spontaneous magnetization $M(T,0)$ decreases and one may use the small argument expansion of the Brillouin function (3.27) to obtain the asymptotic dependence of the magnetization (3.23), namely,

$$M = \left(M_0\frac{J+1}{3J}x\right) - \frac{3}{10}\frac{J^2+(J+1)^2}{(J+1)^2M_0^2}\left(M_0\frac{J+1}{3J}x\right)^3 + \ldots \tag{3.30}$$

where,

$$x = \frac{Jg\mu_B}{kT}(H_a + \lambda M) \tag{3.31}$$

Zero field magnetization exponent β

With $x = Jg\mu_B\lambda M/kT$ when $H_a = 0$ and incorporating equation (3.28) in the expression for the asymptotic dependence of the magnetization(3.30) when $T \to T_c$ from below gives

$$\frac{M}{M_0} = \left[\frac{10}{3}\frac{(J+1)^2}{J^2+(J+1)^2}\right]^{\frac{1}{2}} \frac{T}{T_c}\left[1 - \frac{T}{T_c}\right]^{\frac{1}{2}} \tag{3.32}$$

As expected the zero field magnetization shows a power law behavior in the vicinity of T_c with critical exponent value $\beta = 1/2$.

Susceptibility exponent γ

The isothermal susceptibility is given by

$$\chi_T = \left(\frac{\partial M}{\partial H_a}\right)_T. \tag{3.33}$$

The asymptotic expansion for the magnetization to first order leads to

$$M = \frac{Ng^2\mu_B^2 J(J+1)}{3kT}(H_a + \lambda M) = \frac{CH_a}{T - T_c} \tag{3.34}$$

and may be used to get the expected power law dependence of the susceptibility,

$$\chi_T = \frac{C}{T - T_c} = \frac{t^{-1}}{\lambda}. \tag{3.35}$$

Apparently, from expression (3.35), the susceptibility diverges as the critical point is approached from either the low or high temperature side. The numerical value for the critical exponent γ in MFT is, clearly, one.

Critical isotherm exponent δ

The critical isotherm exponent can be determined by evaluating the expression for the asymptotic expansion of the magnetization (3.30) at T_c given by equation (3.28). The result is as follows,

$$M \approx \left(M + \frac{H_a}{\lambda}\right) - \frac{3}{10}\frac{J^2 + (J+1)^2}{(J+1)^2 M_0^2}\left(M + \frac{H_a}{\lambda}\right)^3. \tag{3.36}$$

For small values of H_a, the above expression becomes,

$$H_a = \frac{3}{10}\frac{J^2 + (J+1)^2}{(J+1)^2 M_0^2} M^3. \tag{3.37}$$

Comparing this with the expected power law dependence $M \sim H^{\frac{1}{\delta}}$, it follows that $\delta = 3$ in MFT.

3.4 Heisenberg and Ising Model

The mean field approach predicts a phase transition, assuming the interaction of magnetic moments occurs through a "molecular field", the origin of which is undefined in this theory. Many other models have been put forward to interpret and give a microscopic understanding of this interaction. Four of the most commonly studied models employ a quantum mechanical approach and they are based on a single model

Hamiltonian, differing primarily in the dimensionality of spin space.The single model Hamiltonian is given as [15]

$$H^D = -\sum_{i,j} J_{ij} \vec{S}_i^D \vec{S}_j^D \tag{3.38}$$

J_{ij} is the "exchange coupling constant" [17] which determine the strength of the nearest neighbour interaction of the magnetic moments, localized at the lattice sites (i) and (j). According to convention, for positive J_{ij} a parallel spin configuration (ferromagnetic order) is energetically favoured while for negative J_{ij} an antiparallel spin configuration (antiferromagnetic order) is favoured . The exchange energy has no classical analogue and expresses the difference in the Coulomb interaction energy for different orientations of the magnetic moments, a consequence of the Pauli exclusion principle. D represents the dimensionality of the spin space, and $D = 1, 2, 3$, and ∞ corresponds to the Ising, Planar, Heisenberg and Spherical model respectively. Thus, in the Ising model, magnetic moments can be taken to be classical 'vectors' with only two possible orientations, up or down. This model can be solved exactly for a one dimensional lattice and exhibits no phase transition. The Ising model for a two dimensional lattice in zero field was solved by Onsager and Yang [18] , and shows a continuous paramagnetic-to-ferromagnetic transition at a finite critical temperature (T_c), but the critical exponents it yields do not agree very well with experimental values. The Ising model for a three-dimensional lattice has not been solved exactly. The model for three-dimensional magnetic moments in the classical limit of quantum theory is called the classical Heisenberg model. In this model spins are not restricted

to the $(2S + 1)$ discrete orientations allowed in quantum mechanics, but may have any orientation equivalent to $S \to \infty$. The classical Heisenberg model assumes completely isotropic interactions, well localized spins and short range interactions. This model cannot be solved exactly for a three-dimensional lattice and various numerical approaches, such as the renormalization group method and series expansion techniques, have been used in an attempt to determine the predictions of this model and compare them with experimental results. The critical point exponents predicted by the Heisenberg and other models are summarized in the table (3.2).

3.5 Scaling Theory

Scaling theory is an heuristic approach to critical phenomena, based on the simple assumption that the thermodynamic potential is a generalized homogeneous function of its argument. Scaling theory does not predict a specific numerical value for any of the critical-point exponents, but leads to functional relationships among the exponents, known as the scaling laws. Historically these laws were supported not only by considerable experimental evidence, but also by the way that all inequalities given in section (3.2.2) may be replaced by equalities.

Critical Exponent	γ	γ'	β	δ
Mean Field Theory	1	1	0.5	3
2-D Ising	1.75	1.75	0.125	15
3-D Ising	1.238	1.25	0.326	4.78
3-D Heisenberg	1.386	—	0.365	4.78
3-D Spherical	2	—	0.5	5
Experimental Results	$1.2 \sim 1.4$	—	$0.2 \sim 0.4$	$3 \sim 6$

Table 3.2: Critical-point exponent values predictions for various models.

3.5.1 Static Scaling Hypothesis

Consider a magnetic system in which the Gibbs free energy $G(t, H)$ is function of reduced temperature $t = (T - T_c)/T_c$ and magnetic field H. The scaling hypothesis asserts that the Gibbs free energy changes under a change of scale according to

$$G(\lambda^{a_t} t, \lambda^{a_H} H) = \lambda G(t, H) \tag{3.39}$$

for any value of the number λ[1]. In general, the scaling hypothesis does not specify the parameters a_t and a_H, but relates the various critical exponents to these two independent scaling parameters. However, the parameters a_t and a_H may be determined if the homogeneous function is known at some point (t_0, H_0), and subsequently all of the critical-point exponents can be related to a_t and a_H.

3.5.2 Scaling Theory: Critical Point Exponents

The scaling of the Gibbs free energy (3.39) implies that the magnetization

$$M(t, H) = -\left(\frac{\partial G}{\partial H}\right)_t \tag{3.40}$$

scales as

$$M(t, H) = \lambda^{a_H - 1} M(\lambda^{a_t} t, \lambda^{a_H} H) \tag{3.41}$$

while the susceptibility

$$\chi_t \equiv \left(\frac{\partial M}{\partial H}\right)_t = -\left(\frac{\partial^2 G}{\partial H^2}\right)_t, \tag{3.42}$$

[1]This λ is arbitrary number and should be distinguish from mean-field coefficient λ.

and the specific heat

$$C_H \equiv -T \left(\frac{\partial^2 G}{\partial T^2} \right)_H , \tag{3.43}$$

scale according to

$$\chi_t(t, H) = \lambda^{2a_H - 1} \chi_t(\lambda^{a_t} t, \lambda^{a_H} H) \tag{3.44}$$

$$C_H(t, H) = \lambda^{2a_t - 1} C_H(\lambda^{a_t} t, \lambda^{a_H} H) \tag{3.45}$$

These scaling expressions for the magnetization, the susceptibility and the specific heat can be used to indicate how the critical exponents are related to the scaling parameters a_t and a_H.

Zero field magnetization exponent β

When $H = 0$ and for the particular choice of $\lambda = (-1/t)^{1/a_t}$, equation (3.41) becomes

$$M(t, 0) = (-t)^{\frac{1-a_H}{a_t}} M(-1, 0) \tag{3.46}$$

The comparison of the latter with the power law behavior of the magnetization

$$M(t, 0) \sim (-t)^{\beta}, \qquad t < 0 \tag{3.47}$$

near the critical point yields an expression for the exponent β in terms of scaling parameters a_t and a_H, as follows,

$$\beta = \frac{1 - a_H}{a_t} \tag{3.48}$$

Critical isotherm exponent δ

The critical-point exponent δ can be found by letting $t = 0$ and choosing $\lambda = H^{-1/a_H}$ in equation (3.41), which gives

$$M(0, H) = H^{\frac{1-a_H}{a_H}} M(0, 1) \tag{3.49}$$

Recalling the power law dependence for the critical isotherm in a region of small field H, namely

$$M(0, H) \sim H^{\frac{1}{\delta}}, \qquad t < 0 \tag{3.50}$$

and comparing with equation (3.49) it becomes apparent that

$$\delta = \frac{a_H}{1 - a_H}. \tag{3.51}$$

Susceptibility exponents γ and γ'

The relation of the exponents γ and γ' to the scaling parameters a_H and a_t can be found by a suitable choice of the arbitrary parameter λ when $H = 0$. For $T < T_c$ $(t \to 0^-)$ and choosing $\lambda = (-t)^{-1/a_t}$ in equation (3.44) gives

$$\chi_t(t, 0) = (-t)^{\frac{-(2a_H - 1)}{a_t}} \chi_t(-1, 0) \sim (-t)^{\frac{-(2a_H - 1)}{a_t}}. \tag{3.52}$$

When $t \to 0^-$, $\chi_t \sim (-t)^{-\gamma'}$. Comparing this with the above equation indicates that

$$\gamma' = \frac{2a_H - 1}{a_t}. \tag{3.53}$$

Similarly, setting $\lambda = t^{\frac{-1}{a_t}}$ for temperatures above critical point, results in

$$\gamma = \frac{2a_H - 1}{a_t} \tag{3.54}$$

Evidently, the primed and unprimed critical exponents are identical in this approach.

Specific heat exponents α and α'

The critical exponents α and α' which describe the behavior of the specific heat in a constant magnetic field H, may also be related to the scaling parameter a_t. Inserting $H = 0$ and $\lambda = (-t)^{-1/a_t}$ into equation (3.45) gives

$$C_H(t,0) = (-t)^{-\frac{2a_t-1}{a_t}} C_H(-1,0) \sim (-t)^{-\frac{2a_t-1}{a_t}}, \tag{3.55}$$

when $t < 0$. By comparing this with the power law form of the specific heat, $C_H \sim (-t)^{-\alpha'}$ gives

$$\alpha' = 2 - \frac{1}{a_t} \tag{3.56}$$

A similar technique yields an identical exponent α for $T > T_c$.

Derivations of the critical point exponents from scaling theory shows that all of the critical-point exponents can be expressed in terms of two independent indices a_t and a_H. This leads to the relationships among critical exponents listed in table (3.3).

3.5.3 Scaling Law Equation of State and Crossover Exponent

Besides predicting relationships between the critical point exponents, scaling theory also makes predictions concerning the functional form of the magnetic equation of state. The scaling approach leads to a "scaled magnetization" expressed in terms of scaling parameters a_H and a_t (3.41). The choice of the parameter $\lambda = t^{-1/a_t}$ in

Rushbrooke	$\alpha + 2\beta + \gamma = 2$
Griffiths	$\alpha + \beta(\delta + 1) = 2$
Griffiths	$\gamma(\delta + 1) = (2 - \alpha)(\delta - 1)$
Widom	$\gamma = \beta(\delta - 1)$
Fisher	$(2 - \eta)\nu = \gamma$

Table 3.3: Equality relations among critical exponents.

equation (3.41) gives

$$M(t, H) = t^{\frac{1-a_H}{a_t}} M\left(1, \frac{H}{t^{\frac{a_H}{a_t}}}\right) \tag{3.57}$$

By recalling the definition of the critical exponents β and δ in terms of the scaling parameters a_t and a_H and providing that the Widom equality, $\gamma = \beta(\delta - 1)$ holds, equation (3.57) can be written in a more simple form, [15] as follows

$$M(t, H) = t^{\beta} M\left(1, \frac{H}{t^{\beta\delta}}\right) = t^{\beta} M\left(1, \frac{H}{t^{\beta+\gamma}}\right) = t^{\beta} F\left(1, \frac{H}{t^{\beta+\gamma}}\right) \tag{3.58}$$

Clearly, in the equation above only the argument of the scaling function F is specified but not its general form. Consequently, the scaled isothermal susceptibility, expressed in terms of scaling function F is given as

$$\chi(t, H) \equiv \left(\frac{\partial M}{\partial H}\right)_t = t^{-\gamma} F'\left(\frac{H}{t^{\beta+\gamma}}\right) \tag{3.59}$$

where $F'\left(H/t^{\beta+\gamma}\right)$ represent the first derivative of F with respect to its argument. This can be simplified by rearranging the above expression [14]

$$\chi(t,H) = \left(\frac{1}{t^{\gamma+\beta}}\right)^{\frac{\gamma}{\gamma+\beta}} F'\left(\frac{H}{t^{\gamma+\beta}}\right) = \tag{3.60}$$

$$= H^{\frac{-\gamma}{\gamma+\beta}} \left(\frac{H}{t^{\gamma+\beta}}\right)^{\frac{\gamma}{\gamma+\beta}} F'\left(\frac{H}{t^{\gamma+\beta}}\right) = \tag{3.61}$$

$$= H^{(\frac{1}{\delta})-1} G\left(\frac{H}{t^{\gamma+\beta}}\right) \tag{3.62}$$

using $G(x) = x^{\gamma/\gamma+\beta}F'(x)$; and $x = H/t^{\gamma+\beta}$. The susceptibility of a system that undergoes a ferromagnetic-to-paramagnetic phase transition exhibits so called "critical peaks" near the critical temperature when small fields are applied. This is shown in figure (3.5). Such peaks are a direct manifestation of critical fluctuations in a system which undergoes a continuous phase transition; they also exhibit a shift in temperature with increasing applied field (fig:3.5). At the peak temperature t_p, the susceptibility in constant applied field H has a maximum, thus satisfying the condition

$$\left(\frac{\partial\chi}{\partial t}\right)_{H,t=t_p} = H^{\frac{1}{\delta}-1}\frac{(\gamma+\beta)H}{t^{(\gamma+\beta+1)}} G\left(\frac{H}{t^{\gamma+\beta}}\right)_{t=t_p} = 0. \tag{3.63}$$

Obviously, this is true only if $G'\left(H/t^{\gamma+\beta}\right)_{t=t_p} = 0$, or $(G)_{t=t_p} = const.$, requiring in turn that G has a constant argument i.e. $H/t_p^{\gamma+\beta} = const.$ Thus, the susceptibility maxima $\chi(H,t_p)$ move upward in temperature with increasing field along a "cross-over" line, given by

$$T_p \propto H^{\frac{1}{\gamma+\beta}}, \tag{3.64}$$

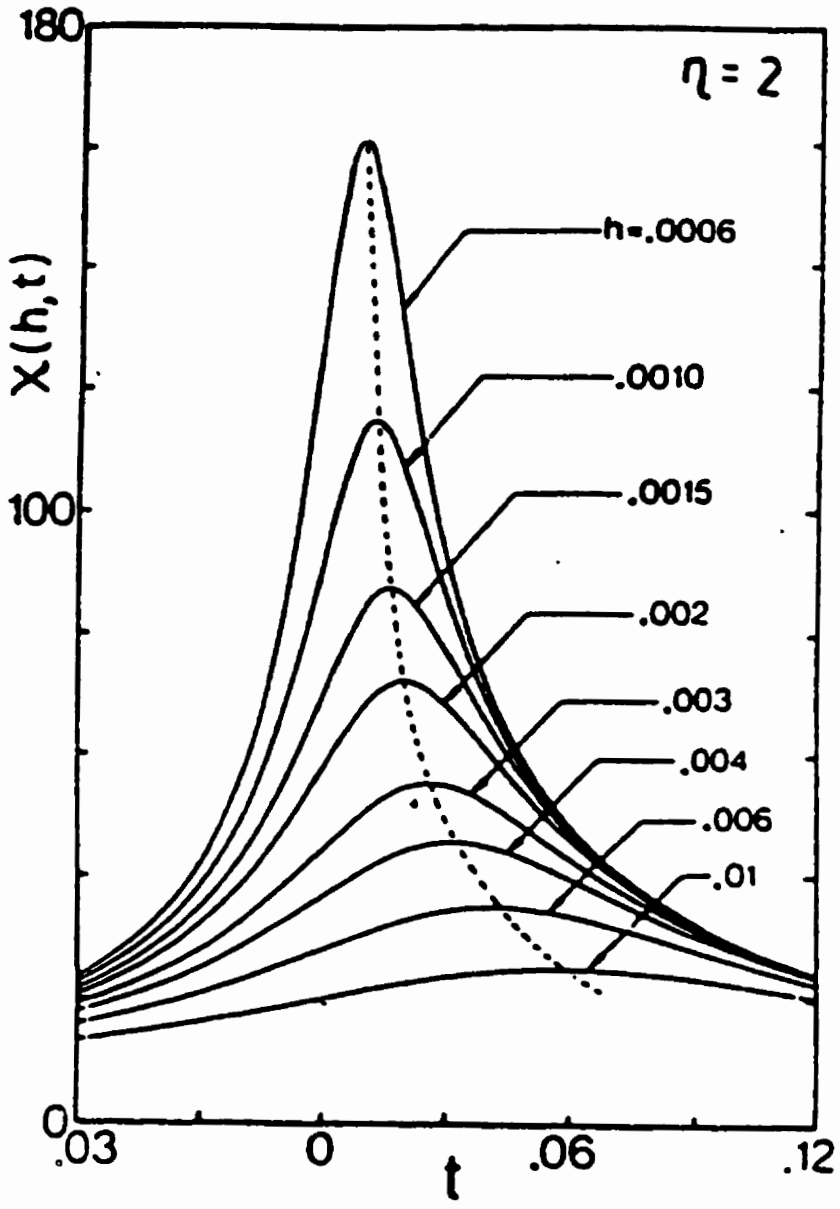

Figure 3.5: The susceptibility $\chi(h, t)$ in various fixed fields h; the dotted line represents the cross-over line [14]

where $\gamma + \beta$ is known as the "cross-over" exponent. Moreover, since the scaling function G is constant at t_p, χ at t_p depends on field alone, and is given by

$$\chi(t_p, H) \propto H^{(\frac{1}{\delta}-1)} \qquad (\delta > 1) \tag{3.65}$$

The susceptibility amplitude at t_p decreases with increasing H ($\delta > 0$), reproducing the experimentally observed behaviour of the susceptibility in the vicinity of T_c Equation (3.65) can be used to determine the exponent δ experimentally and has the advantage over the critical isotherm measurement that it does not require a precise determination of T_c. However, to find the "cross-over" exponent experimentally, T_c must be known.

3.6 Sherrington - Kirkpatrick Model

This model is concerned with the problem of describing a system with spatially randomly distributed spins. It is assumed that such site disorder may be replaced by an exchange bond disorder. Sherrington and Kirkpatrick examined an Ising model with infinite - range exchange interactions. The Hamiltonian of such a system is given by

$$H = -\frac{1}{2}\sum_{i \neq j} J_{ij} s_i s_j; \qquad s_i = \pm 1 \tag{3.66}$$

in which the exchange coupling constant J_{ij} was assumed to have a Gaussian probability density $p(J_{ij})$ centered about some point J_0 with distribution width of J.

$$p(J_{ij}) = \frac{1}{\sqrt{2\pi}J} \exp\left[\frac{-(J_{ij} - J_0)^2}{2J^2}\right] \tag{3.67}$$

J_0 and J are scaled according to $J_0 = \tilde{J}_0/N$ and $J = \tilde{J}/\sqrt{N}$ in order to become intensive parameters; clearly the magnitude of J_0 gives the mean strength of the interaction while the width J measures the amount of disorder. Thus, for a system without disorder, $J = 0$ and with $J_0 > 0$ one has a pure ferromagnet. The presence of disorder is often characterized by the parameter $\eta = J_0/J$, in mean field theory if $\eta > 1$ a ferromagnetic ground state results but if $\eta < 1$ a state of frozen spins, called a "spin-glass" emerges at low temperature. In order to characterize these magnetic phases two order parameters are needed; namely

$$m = \langle \langle S_i \rangle_T \rangle_J \tag{3.68}$$

$$q = \langle \langle S_i \rangle_T^2 \rangle_J \tag{3.69}$$

where $\langle\ \rangle_T$ represents an average over thermal fluctuations, while $\langle\ \rangle_J$ is an average over the exchange distribution. These quantities were obtained from the free energy calculated using the "replica trick" method for $s = 1/2$ [19]. The same results for m and q were derived using an effective field approach [20]. The expressions for m and q were generalized to a system of arbitrary spin S [21], yielding

$$m = \frac{1}{\sqrt{2\pi}} \int_{-\infty}^{\infty} S B_S \left[\frac{S}{k_B T} (J_0 m + J q^{\frac{1}{2}} \alpha + h_a) \right] e^{-\frac{\alpha^2}{2}} d\alpha \tag{3.70}$$

$$q = \frac{1}{\sqrt{2\pi}} \int_{-\infty}^{\infty} S^2 B_S^2 \left[\frac{S}{k_B T} (J_0 m + J q^{\frac{1}{2}} \alpha + h_a) \right] e^{-\frac{\alpha^2}{2}} d\alpha \tag{3.71}$$

where, $h_a = g\mu_B H$ and $B_S(x)$, the Brillouin function for spin S, is given by

$$B_S = \frac{2S+1}{2S} \coth\left(\frac{2S+1}{2S} x\right) - \frac{1}{2S} \coth\left(\frac{x}{2S}\right) \tag{3.72}$$

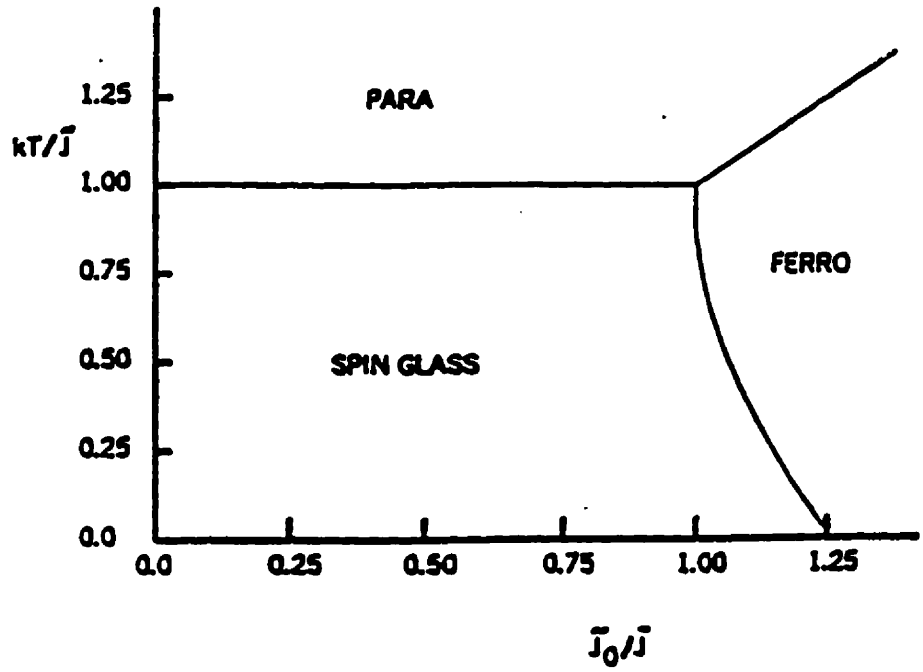

Figure 3.6: Sherrington-Kirkpatrick phase diagram [19].

The phase diagram for this model as a function of $\eta = J_0/J$ and T is given in figure (3.6) For $\eta < 1$ the system is a "spin-glass" at low T but, if the temperature is increased, the system undergoes a transition to a paramagnetic state. An intermediate region $1 < \eta < 1.25$ represents a double transition region with "spin-glass", ferromagnetic and paramagnetic states possible. Finally for $\eta > 1.25$ a ferromagnetic state (at lower T) and paramagnetic state (at higher T) exist. This model gives a qualitative description of disordered systems. The calculated temperature dependence of the susceptibility in a variety of applied fields in the ferromagnetic regime [41] shows

agreement with Scaling theory predictions for the field and temperature dependence of the susceptibility peaks, while critical exponents have mean field values.

3.7 Electronic Transport

The current density $\vec{j}$ and electric field $\vec{E}$ inside a conducting material are related by Ohm's law

$$\vec{j} = \sigma\vec{E} = \rho^{-1}\vec{E}. \tag{3.73}$$

Here ρ represents the resistivity tensor and its inverse σ is the conductivity tensor. In non- magnetic materials the resistivity results from scattering of conduction electrons by impurities and lattice imperfections (ρ_i) and scattering caused by lattice vibrations (ρ_L). The scattering is not present in a perfect lattice [22]. These two contributions to the resistivity are often independent of each other and give additive contributions to the resistivity. This result is known as Matthiessen's rule [23].

$$\rho(T) = \rho_i(T) + \rho_L(T). \tag{3.74}$$

The term $\rho_i(T)$ is dominant at low temperatures (typically $\leq$ 4K) and for low impurity concentrations is usually independent of temperature. The term $\rho_L(T)$ is dominant at higher temperatures ($\sim$ 300K). The resistivity of magnetic materials has an additional term (ρ_m) arising from magnetic scattering and deviations from Matthiessen's rule are also present, especially in the critical region. The magnetic term in the resistivity generally depends on the type of magnetic order present. Above the ordering

temperature (in the paramagnetic region), (ρ_m) is approximately constant and only the phonon term in the resistivity shows a temperature dependence. In the critical region ρ_m decreases and the resistivity exhibits an abrupt change in slope in the vicinity of the critical temperature. At low temperatures, for metals such as Ni, Co, and Fe, it has been found that the resistivity varies with temperature as T^2. Such a dependence is attributed to electron-magnon scattering at low temperature. In an applied magnetic field, the Lorentz force $q\vec{v} \times \vec{B}$ acts on the electrons and curves their path. This causes a small increase in the resistivity when a magnetic field is applied in the low temperature range. At higher temperature, the electron- phonon scattering tends to reduce such cyclotron curvature effects. This effect is appreciable only if the mean free path for electrons is of the same order or greater than the radius of curvature of the electron trajectory [24]. Models which attempt to describe the behavior of ρ_m as well as the temperature and the field dependence of the resistivity are summarized below.

3.7.1 Localized Models

The magnetic contribution to the resistivity in this model arises from scattering of the electrons from moments localized at lattice sites. This scattering is attributed to the exchange interaction between the local moments ($\vec{S}$) and spins of the conduction electrons ($\vec{\sigma}$), written $J\vec{S}\cdot\vec{\sigma}$. Above the critical temperature this yields a temperature

independent (constant) paramagnetic resistivity, given by [25]

$$\rho_m = \frac{k_F (mJ)^2}{4\pi e^2 z \hbar^3} S(S+1) \tag{3.75}$$

Here J is the interaction constant between localized moment and the electron spin, k_F is the Fermi vector and z is the impurity valency. For ferromagnets, lowering the temperature through T_c decreases ρ_m by decreasing spin disorder and the associated scattering rate. This causes an abrupt change in the slope of $\rho(T)$ at T_c. For the region around T_c the resistivity depends on the spin-spin correlation function [25]. As a consequence, critical magnetic scattering yields a peak in $d\rho/dt$ at T_c and the critical behavior is predicted to be the same as that of the specific heat [26]. For impurities with both spin and orbital contributions to their moment the scattering Hamiltonian is given by

$$H_{scatt} = \left[V + J(\vec{\sigma} \cdot \vec{S}) - \frac{D}{k_F^2} \left((\vec{S} \cdot \vec{k})(\vec{S} \cdot \vec{k}') - \frac{S(S+1)}{3} \vec{k} \cdot \vec{k}' \right) + \ldots \right] a_{\vec{k}'}^{+} a_{\vec{k}} \tag{3.76}$$

The first two terms are the Coulomb potential between the electrons and ion cores and the exchange potential, respectively. The third term represents the interaction between electrons and electric quadrupole moment of the impurity which is the first non-negligible term in a multipole expansion of the non-spherically symmetric charge density distribution in central fields. In equation (3.76) D represents the quadrupolar moment, $a_{\vec{k}'}^{+}$ and $a_{\vec{k}}$ are creation and annihilation operators for electrons with wave vectors $\vec{k}'$ and $\vec{k}$. For polycrystalline materials the first two terms in the scattering Hamiltonian are isotropic and the anisotropy in the magnetoresistance is present

only if there is spin-orbit ($L \neq 0$) coupling in the material. This coupling causes the non-spherical quadrupole contribution (D) to rotate with the spin $\vec{S}$ when the field direction is changed, resulting in different scattering cross-sections for electrons. The consequence of such anisotropy is a difference in the resistivity when the relative orientation of the applied field and current is changed from, say, a parallel to a perpendicular configuration. Such effects are investigated by measuring the spontaneous resistive anisotropy (SRA), which is usually defined by the ratio [27]

$$\frac{\Delta\rho}{\rho} = \left[\frac{\rho_{\parallel}(B) - \rho_{\perp}(B)}{\frac{1}{3}\rho_{\parallel}(B) + \frac{2}{3}\rho_{\perp}(B)}\right]_{B\to 0} \tag{3.77}$$

which characterizes the difference between the longitudinal and transverse magnetoresistance of a (technically) single domain ferromagnet extrapolated to zero induction B. The resistivity tensor for a ferromagnetic material is also function of the magnetic induction B. The induction B depends on the applied magnetic field H_a and on the demagnetizing factor D characterizing a particular sample geometry, and is given as

$$B = H + 4\pi M(1 - D) \tag{3.78}$$

For the Hamiltonian given in (3.76), and in a limit of $V >> D$, the resistive anisotropy is given by [31]

$$\frac{\Delta\rho}{\rho_0} = \frac{D}{V}\left(< S_z^2 > - \frac{S(S+1)}{3}\right). \tag{3.79}$$

For $T \gg \mu_B H/k_B$, $< S_z^2 >= S(S+1)/3$, and no anisotropy exists. With decreasing temperature, $< S_z^2 >$ increases, and an anisotropy is observed. The localized model

can be applied to systems with localized magnetic moments, such as rare- earths, while the validity of this model in the case of transition metals is questionable.

3.7.2 Itinerant Model

Localized models assume that the spin ↑ and the spin ↓ electrons carry the same current. However even in such models if there is a spin independent scattering potential V at magnetic sites, in addition to the exchange potential described in the previous section, so that at low temperature the spin ↑ and spin ↓ states are subject to to potentials $V + J\vec{\sigma} \cdot \vec{S}$ and $V - J\vec{\sigma} \cdot \vec{S}$ respectively. This results in different currents for the spin ↑ and spin ↓ conduction electrons [27].

The first model which specifically takes such effects into account - the so called two current model - was proposed by Mott [28] and was used to explain the temperature dependence of the resistivity for transition metal ferromagnets. The model considers the s and d band to be divided into the spin ↑ and spin ↓ sub-bands which conduct in parallel. Accordingly, the total resistivity is given as

$$\rho = \frac{\rho_\uparrow \rho_\downarrow}{\rho_\uparrow + \rho_\downarrow}. \tag{3.80}$$

$\rho_\uparrow$ and $\rho_\downarrow$ are resistivities of each sub-band and they are expressed as the sum [30, 29] of the contribution due to s - s scattering which is an isotropic effect ($\rho_{ss\uparrow} = \rho_{ss\downarrow}$) and the contribution due to s - d scattering which is anisotropic as the d ↑ and d ↓ density of states at the Fermi level are different, resulting in a different s - d scattering rate

for the spin ↑ and spin ↓ conduction electrons ($\rho_{sd\uparrow} \neq \rho_{sd\downarrow}$), namely

$$\rho_{\uparrow} = \rho_{ss\uparrow} + \rho_{sd\uparrow} \tag{3.81}$$

$$\rho_{\downarrow} = \rho_{ss\downarrow} + \rho_{sd\downarrow}. \tag{3.82}$$

The original Mott model has been modified [31, 27, 30, 29, 32] to include spin-flip scattering effects. These effects are due to spin-orbit or electron-magnon scattering. Including the spin-flip effects, the total resistivity is given as [27]

$$\rho = \frac{\rho_{\uparrow}\rho_{\downarrow} + \rho_{\uparrow\downarrow}(\rho_{\uparrow} + \rho_{\downarrow})}{\rho_{\uparrow} + \rho_{\downarrow} + 4\rho_{\uparrow\downarrow}} \tag{3.83}$$

where $\rho_{\uparrow\downarrow}$ is the resistivity associated with the transfer of electron between sub-bands induced by spin-flip scattering processes. The resistive anisotropy is a spin orbit effect and obviously, in this model, s - s scattering does not contribute to the anisotropy, as s state electrons do not possess an orbital moment. All contributions must come from the s -d scattering and spin-flip scattering. A second-order perturbation theory approach to the scattering leads to an approximate expression for the anisotropy in the presence of an exchange field, H_{ex}, between moments [30, 29, 33]

$$\frac{\Delta\rho}{\rho_0} \simeq \frac{\gamma[\rho_{sd\downarrow} - \rho_{sd\uparrow}]^2}{\rho_{\uparrow}\rho_{\downarrow} + \rho_{\uparrow\downarrow}(\rho_{\uparrow} + \rho_{\downarrow})}. \tag{3.84}$$

Here, $\gamma \propto \lambda^2/(K^2 \pm H_{ex}^2)$, and for cubic systems K is the crystalline field anisotropy and is included to prevent the expression from diverging when $H_{ex} \rightarrow 0$ as $T \rightarrow T_c$. The calculated anisotropy vanishes in the non-magnetic regime due to the equality of the spin ↑ and spin ↓ resistivities when $H_{ex} = 0$, while in the magnetic regime

$H_{ex} \neq 0$ and for $\lambda \neq 0$ an anisotropy is present. Near T_c, this anisotropy is expected to vary linearly with temperature in this model.

Chapter 4

Experimental Methods

4.1 Sample Preparation and Characteristics

Samples of $La_{0.67}Pb_{0.33}MnO_3$ (nominal) were prepared by standard ceramics techniques. Stoichiometric quantities of La_2O_3(ultra pure), PbO and MnO_2 were mixed for 24 hours by ball milling in acetone, to get uniform mixture. The dried powder was subsequently pressed into pellet form and heated to 800°C for 24 hours in air; this procedure was repeated three times following intermediate 6 hour periods of ball milling in order that chemical reaction may occur. The powder was then mixed with a binder, pressed into pellet form and annealed at 1100°C in air for 72 hours, a process believed to enhance sintering and enlarge grain size. The resulting pellet was cut using a diamond saw into samples of rectangular shape. The approximate dimensions of the specimen used in transport and magnetic measurements were $(6 \times 1 \times 1)$

mm^3. These rectangular samples were then heated at 1000°C for 20 hrs to relieve the stress introduced by cutting the samples. After removal from this furnace - effectively a quench in air - the samples were treated finally for 72 hours at 600°C in a flow of air to fully oxygenate the sample. Structural characteristics of the specimen were examined by x-ray powder diffraction studies. Room temperature x-ray diffraction revealed a single phase, nearly cubic structure with a = 3.8927 $\mathring{A}$ and a slight rhombohedral distortion, $\beta = 90.30^o$. Such a distorted perovskite structure for this $La_{0.67}Pb_{0.33}MnO_3$ compound was expected according to a calculation of the tolerance factor (eq:2.6) by Jonker and van Santen [1]. These structural features also correlate well with the relatively high paramagnetic to ferromagnetic and metal-insulator transition temperatures ($\sim 340.5K$) for this system via a recent bond-valence analysis of such effect in the manganese perovskites [34].

4.2 Magnetic Measurements

4.2.1 Equipment Description

The dc magnetization and ac susceptibility measurements were performed using a Quantum Design Physical Property Measurement System (PPMS). The main parts of this system are the PPMS probe and the PPMS dewar. The aluminum dewar contains a liquid helium bath into which the PPMS probe is immersed. The outer layer of dewar contains an isolation space. This space is evacuated through a valve

system, and contains activated charcoal to help maintain a vacuum. A set of heat shields is placed around the neck of the helium container. A schematic diagram of the probe is shown in figure (4.1). The PPMS probe incorporates all elements of temperature control hardware, the superconducting magnet, a helium level meter, a variety of electrical contacts, gas lines and sample puck connectors. Two concentric tubes with a sealed, evacuated region in between serve to isolate the sample chamber from the helium bath. Within these two tubes is a sample tube, the lower part of which is made from copper to provide a uniform temperature region. Two temperature sensors and a heater are located at the bottom of the sample tube. A platinum resistance thermometer is used for measuring temperatures above about 80 K, while a negative temperature coefficient (NTC) thermometer is used below about 100 K. NTC thermistors are electronic components, usually ceramic semiconductors, that exhibit a large change in resistance with change of temperature, having a negative temperature coefficient. They are usually used to compensate temperature in a circuit where a positive temperature coefficient prevails. The PPMS utilizes liquid helium for temperature control. Between the sample tube and the inner vacuum tube is a so called cooling annulus. Helium is pulled into this region, through an impedance tube, in order to warm or cool the sample tube evenly. The impedance assembly, which contains a narrow tube, a heater and a thermometer, serves to enable or disable the helium flow from the main dewar into the annulus. When the heater is switched on, bubbles form within the impedance tube and the liquid helium flow is blocked. However, when

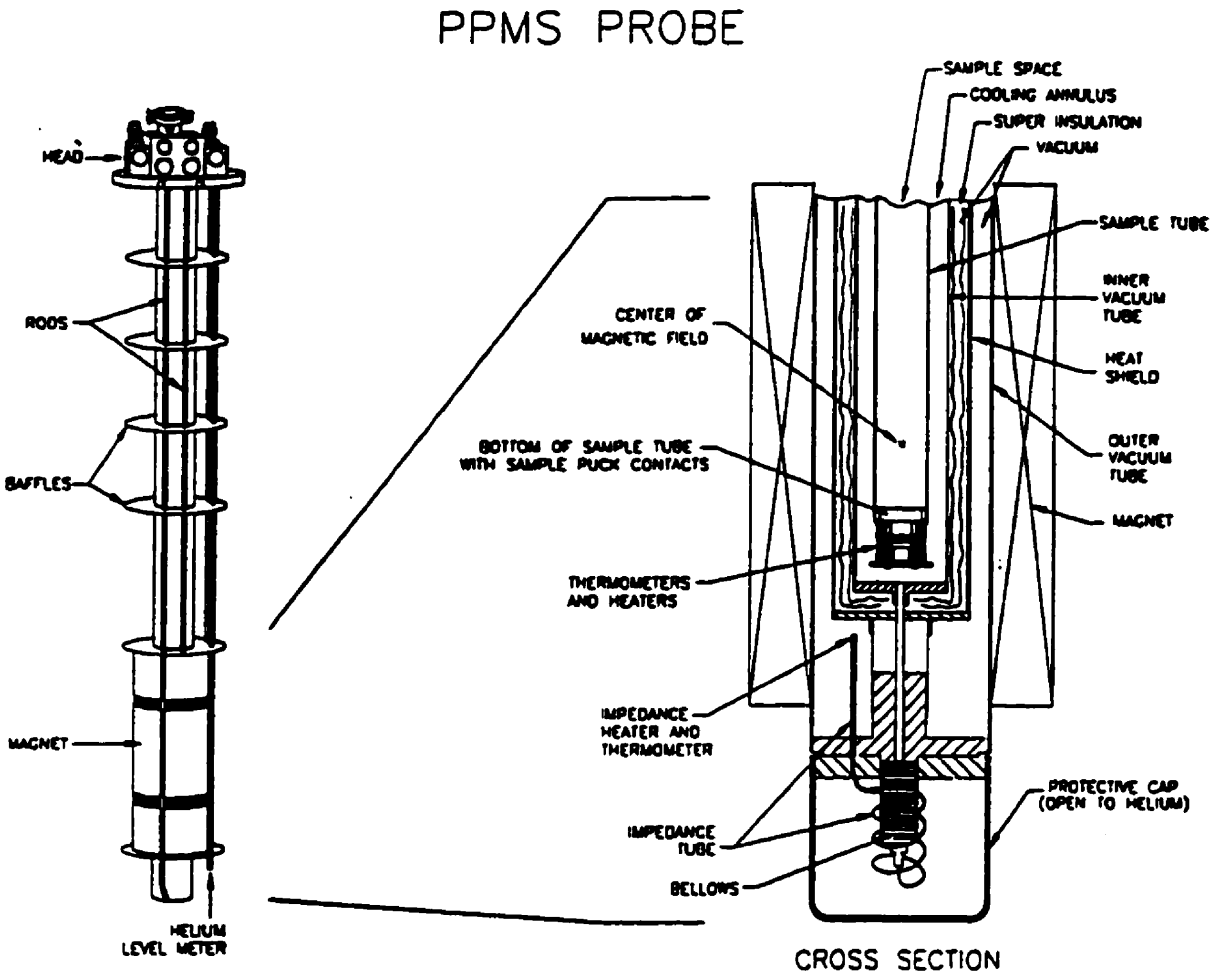

Figure 4.1: The Physical Property measurement system.

the heater is switched off, liquid helium can flow into the annulus where, depending on the pressure inside the annulus, it is vaporized or allowed to fill the annulus. Two different approach modes can be used to attain the desired sample temperature. For samples that exhibit temperature hysteresis the "no overshoot" mode is used, while the "fast settle" mode allows fast changes in temperature to be effected. The superconducting magnet surrounds the probe and is, of course, immersed in liquid helium. The solenoid windings are composed of a Niobium/Titanium alloy embedded in copper. The magnet power supply can be switched into the solenoid itself by a persistent switch, thus allowing a change of magnetic field. The persistence switch consists of a small heater located on a portion of the superconducting wire composing the switch. When constant magnetic fields are applied the magnet operates in a persistent mode i.e. the persistent switch (heater) is turned off allowing a superconducting closed circuit to be formed. The magnet power supply provides a current for the magnet. Charging and discharging the magnet is controlled by setting the current output of the magnet controller (the magnet power supply). Besides persistent mode operation, the magnet can function in a driven mode, which retains the power supply in the magnet circuit in order to drive current, allowing faster field changes than in a persistent mode. Three different charging modes can be used. To minimize the effect of magnetic field relaxation, the oscillate mode, which allows overshoot (or undershoot) of a set point, can be used. The set point can also be approached without changing the charging direction; this is called the "no overshoot" mode and usually is used when

measuring samples that show field hysteretic behaviour. The quickest charging mode is the linear mode, in which the field is fine-tuned after an initial attempt to reach the set point. The probe head is positioned in the top of the PPMS probe. It provides access to the sample chamber, to the two helium fill ports and all the connection ports to attach gas, vacuum and electrical lines to the probe from a controller. The major element of the PPMS is the Model 6000 controller. It houses all of the gas control valves and system electronics. The main parts of the controller are : the CPU board (processor), the motherboard (system integration), the system bridge (temperature readings), the gas valves and gas lines (temperature control), the front panel (user interface) and the rear panel (connections). The Model 6000 controller is used to control all of the PPMS hardware. All functions that the controller can perform, including a recording of measurement values, can be programmed within a sequence file that runs automatically. The AC Measurement System (ACMS), shown in figure (4.2), allows ac susceptibility and dc magnetization measurements to be made. The ACMS insert is installed in the PPMS sample chamber (see figure 4.1) and houses the system's drive and detection coils, thermometers, and electrical connections. Within the insert is a sample space that lies within the uniform field region of the magnet. The sample is mounted on the end of a thin sample rod held within the insert coils. The sample holder can be moved by a dc servo motor, mounted at the top of the PPMS probe. The drive coil is wound longitudinally around the detection coil set, and can generate alternating fields of up to ± 10 Oe in the frequency range 10 Hz to

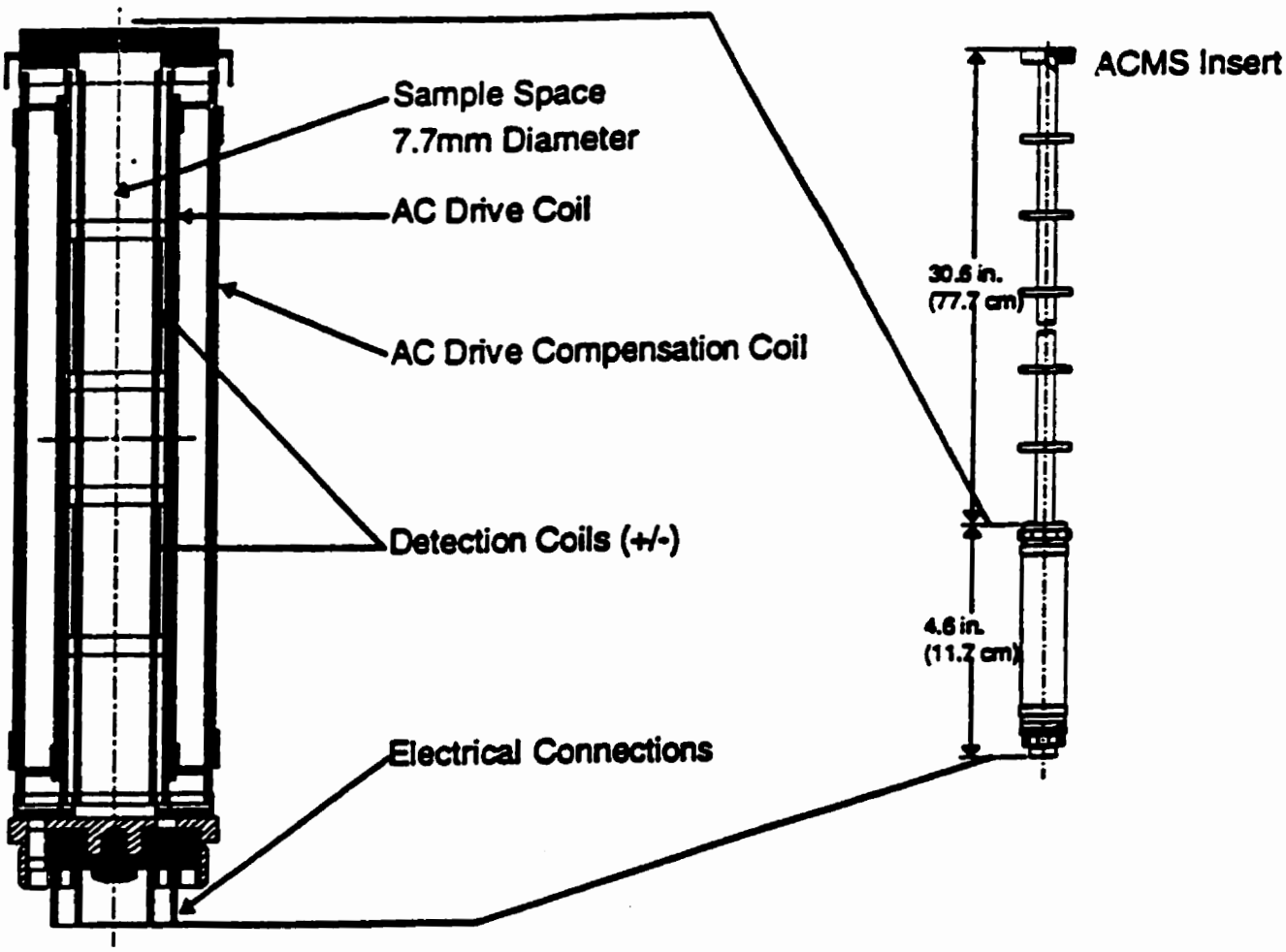

Figure 4.2: The ACMS insert and coil set.

10 kHz, at any temperature. The detection coils are arranged in two counter-wound copper coils connected in series and separated by several centimeters. The ACMS also contains compensation coils, situated outside the ac drive coil, to reduce instrument interaction with any conductive/magnetic material outside the measuring region. In addition to the PPMS thermometers, the ACMS has a thermometer mounted on its coil former. The sample is maintained in close thermal contact with this thermometer using low-pressure helium vapor inside the sample chamber, allowing a fast response time.

4.2.2 AC and DC Measurement Technique and Procedure

When the PPMS is used as a dc magnetometer, it allows measurements of the sample's magnetic moment M in various applied fields at a specific temperature. The dc measuring technique uses the so called "extraction method". In this method a constant field is applied to the measurement region and the sample is moved quickly throughout both sets of coils, inducing a signal in them according to Faraday's law. The signal induced by moving the sample through a set of copper coils is analyzed with a digital signal processor in order to determine the sample's magnetic moment. When the PPMS is used as ac susceptometer, both the amplitude and the phase of the sample's magnetic moment response can be measured. In ac measurements an alternating field is applied to the measurement region and the sample is moved between the centers of each detection coil with the induced signal yielding the incremental

moment. The magnetic response of the sample is then measured, and both the amplitude and phase of this response are recorded. This reported amplitude represents a change in the magnetic moment (dM), and to obtain the ac susceptibility, one must divide the amplitude of the change in moment by the amplitude of the superimposed alternating field (dH). However, to get a "true" susceptibility it is necessary to include the demagnetizing correction, which is discussed in the following section.

Measurements of magnetization and susceptibility involved both the temperature dependence at fixed applied field and the field dependence at constant temperature. Such measurements can depend on the magnetic history of the sample i.e. hysteresis; the latter were removed by demagnetizing the sample. Prior to each run of either temperature or field sweeps, the sample was heated well above the critical temperature, and then cooled to the next measuring temperature in "zero" magnetic field. The purpose of this procedure was to ensure that each run was always started with the sample in the same magnetic state. To ensure a true zero field, the remanent field present in the superconducting magnet was backed off by applying an appropriate field of the same amplitude but opposite direction to the remanent field . It should be noted that the horizontal component of local Earth's field ($\sim 24\mu$ T) was present. However this is inconsequential when doing a high field measurement. The ac susceptibility temperature sweeps were performed in a series of static biasing fields ranging from 30 to 100 mT superimposed on the ac driving field (usually of amplitude 3μT and frequency of 2.4 kHz). Both ac and dc fields were applied along the largest

sample dimension. The dependence of magnetization on temperature was measured simultaneously with the ac susceptibility. Temperature was controlled automatically, and to ensure that the sample temperature was the same as the temperature sensor temperature, the PPMS was programmed to wait prior to each measurement for a reasonable amount of time, ranging from 1-2 minutes during temperature sweeps, to 30 minutes for a field sweeps at constant temperature. The magnetization-field sweeps were taken for two orientations of the sample relative to magnetic field, one along the longest and the other along the second shortest axis, in each case ensuring consistency of the magnetic state by warming the sample above T_c prior to each run. Before beginning any measurement, the sample was centered automatically, thus optimizing the sample position to provide the maximum signal.

4.3 AC and DC Resistivity and Magnetoresistance Measurements

Resistance and magnetoresistance measurements were carried out using a conventional four-probe method using both standard dc and low frequency (37 HZ) ac techniques; in both methods the measuring current flowed along the largest sample dimension. The equipment used for these measurements, as well as the measurement techniques and principles are discussed below.

4.3.1 Measurement Technique

The conventional method for measuring resistivity is the four-probe dc technique. In this method, a known current I is applied to a specimen and the potential drop V across the specimen is measured. The resistivity is then calculated using Ohm's law, R = V/I. To find the specific resistance of a material one must eliminate any dependence on specific sample geometry. This is done by multiplying the resistance by a form factor, namely

$$\rho = R\frac{A}{L}. \tag{4.1}$$

Using the four-probe dc method, the absolute value of the resistivity can be most accurately determined, while for measuring small changes in voltage superimposed on a much larger voltage signal, the ac technique is preferable. In addition, when measuring small changes, the dc method tends to be sensitive to thermal emf's and contact impedance. This can be avoided using the ac difference technique which allows measurement of the fractional change in the output signal as small as a few parts per million. The electronics for the ac method were described in detail by Muir and Ström-Olsen[35]. Figure (4.3) shows the circuit diagram of the system used. An alternating current of low frequency (37 Hz) is supplied to the sample using a General Radio 1311A audio oscillator. The signal generator also provides the reference signal for a Princeton Applied Research HR8 lock-in amplifier and a Kelvin - Varley DP1211 potentiometer. An initial voltage, V_0, tapped off the Kelvin - Varley divider, is subtracted from the sample voltage and the voltage difference

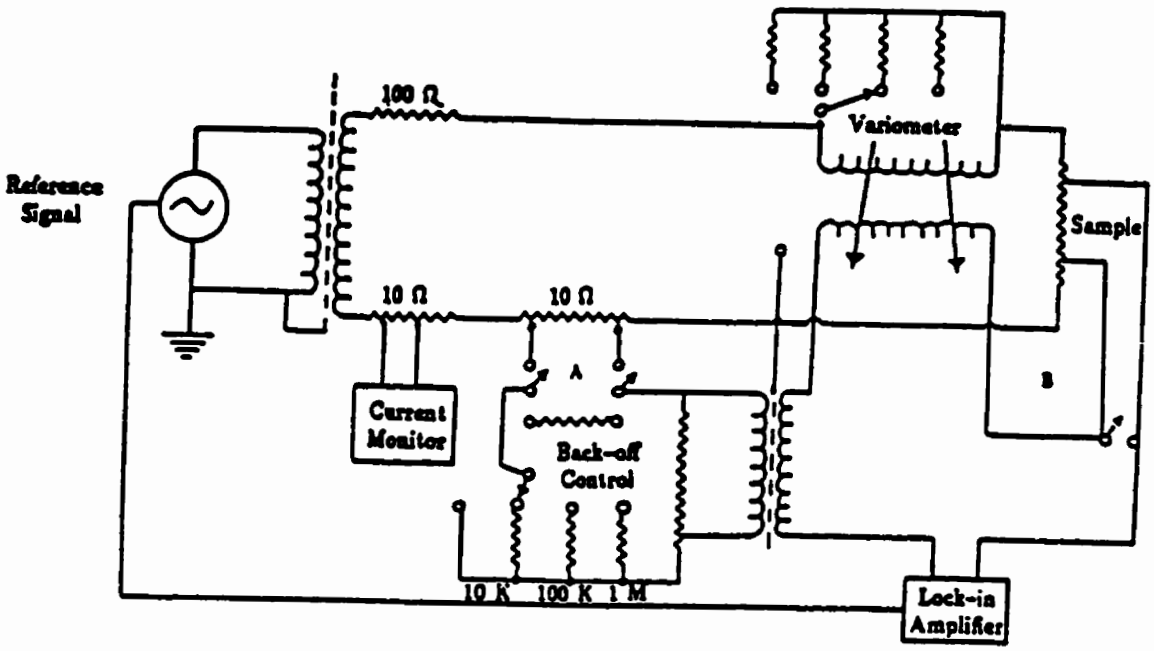

Figure 4.3: Detailed circuit diagram of ac resistivity measurement system [36].

between this potentiometer and the sample is then measured with the precision lock-in amplifier tuned to the driving frequency of the oscillator. In order to obtain a high sensitivity in the measurement, a variometer is also placed in the circuit to remove the effect of the out-of-phase (the quadrature component) in the signal from the system. The variometer consists of a stationary primary coil of 150 turns and two rotatable secondary coils of 250 and 10 turns respectively. This allows coarse and fine adjustment of the out of phase signal. Adjusting the lock-in amplifier to be completely in phase with the reference signal eliminates any effects of the quadrature components on the output signal.

Using the ac method it was possible to measure small changes in signal induced by changes in temperature and/or magnetic field. As was done for ac susceptibility and magnetization measurements, the sample was cooled initially from above its critical temperature in zero magnetic field to liquid helium temperature. The electronic system is tuned, and the reading of the back-off initial voltage was acquired by opening switch A in figure (4.3). Subsequently, this switch was closed again and the lock- in amplifier was set on an appropriate sensitivity. The output from the lock-in amplifier and the current of the magnet power supply or the resistance of the temperature sensor were read using two HP34401 multimeters. Data were collected by a computer with a GPIB card. After removing the sample from the cryostat, the distance between voltage electrical contacts was measured using a Picker traveling microscope in order to determine the form factor.

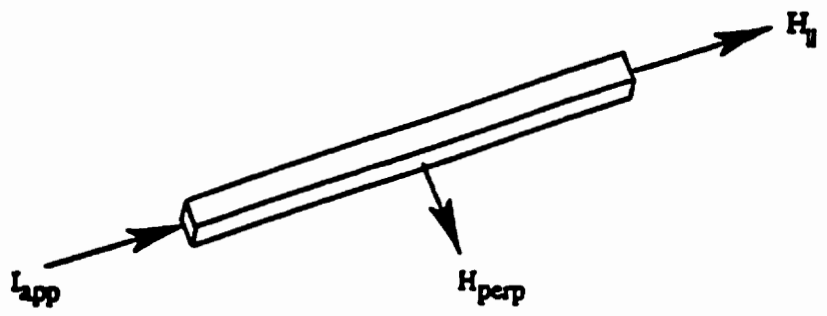

Figure 4.4: Experimental geometry for magnetoresistance measurement.

The experimental geometry of the magnetoresistance measurement is shown in figure (4.4). Magnetoresistance depends on the relative orientation of the magnetic field and the measuring current, and usually just two configurations are considered in an experiment. As depicted in figure (4.4), the current flow is along the longest sample dimension and the magnetic field is then applied either parallel or perpendicular to the current flow. The relative orientation of the current and field can be changed by rotating the sample.

4.3.2 Spontaneous Resistive Anisotropy (SRA) Systems

The spontaneous resistive anisotropy measurements were performed in two different cryostat systems. The ac measuring method was used in the cryostat that allows temperature control in the temperature range of 1.7 to 70 K while the dc method was

used in a cryostat that allows temperature control in the range of 77 to 380 K. The low temperature system has a sample block capable of rotating through 90°, so that the change from a parallel to a perpendicular orientation of current and magnetic field can be achieved easily. The original sample block is roughly circular, with a diameter of 4.8 cm and a thickness of 0.4 cm. It is made from Oxygen-Free High Conductivity (OFHC) copper. A small sample holder, also made of OFHC copper, and of approximate dimension (15 × 10 × 3) mm^3 was attached to the copper block. The sample was electrically isolated from the copper by a fiberglass plate and layers of highly permeable cigarette paper soaked in General Electric 7031b vanish (GE varnish). The GE varnish was used due to its good thermal conductivity down to low temperature. The fiberglass plate has four indium coated electrical contacts, the inner one for voltage and the outer for current connections. The samples were often very fragile, and to ensure no movement of the sample during measurement they were secured with a fiberglass yoke which was secured using screws with small springs around them. The springs were made of a copper-phosphorous alloy wire which maintains its elastic properties at low temperatures. Alternatively, the electrical contacts were made carefully using silver paint and gold wire. For temperature measurement, a Lake Shore Cryogenics CGR-1-2000 calibrated carbon glass resistor was used. The resistor was inserted directly into the sample block to reduce the possibility of thermal gradients between the sample and the thermometer. Temperatures were controlled using a Lake Shore Model 520 temperature controller. A heater, made of Cupron

wire of nominal resistance 25Ω at 77 K, was wound around the sample block. When controlling a constant temperature above 40 K, better temperature control was achieved using an ac phase sensitive Wheatstone Bridge arrangement, with a rectified dc feedback current to the heater. The temperature of the sample was estimated by an Allen-Bradley carbon resistor mounted on the sample block and calibrated using a CGR-1-2000 carbon-glass resistor. The carbon resistor was connected in one arm of the Wheatstone bridge circuit, and a reference resistance in the other. An additional heater, with a room temperature resistance of 500 Ω, was wound on the sample block, and electrically isolated from it using GE varnish and cigarette paper, as described above. This latter system is reproduced schematically in figure (4.5). The sample probe with a rotatable sample block sits isolated within a stainless steel tube 5 cm in diameter extending from the top of the cryostat to a little way above the magnet. A concentric double-walled copper sample can, 6.2 cm in diameter, was soldered to the lower part of this tube. The space between the two walls of the sample serves as an isolation space. A pumping line, connected to a mechanical and diffusion pump, and a helium gas inlet line are connected to the isolation space allowing control of the thermal contact between the sample space and the cooling liquid, by varying the amount of exchange gas in this space. The sample space is centered in the bore of the superconducting magnet, the latter providing magnetic fields up to 3T. The magnet is supported at its rim by hard soldering to the stainless steel tube immediately above the sample can, and additional supporting rods extend from this rim to the

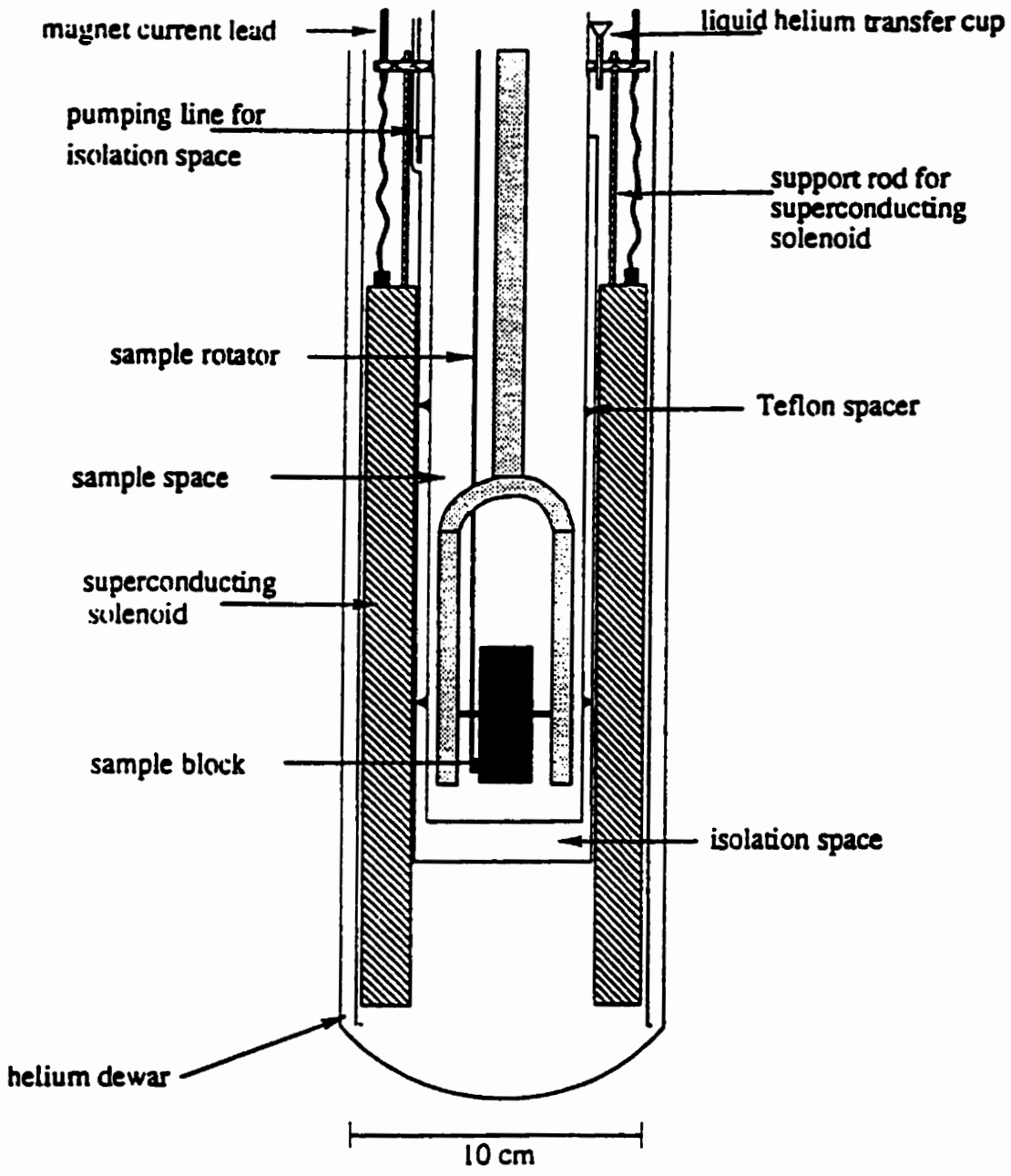

Figure 4.5: The SRA cryostat. Scale is as indicated in the figure.

top of the cryostat. The supporting rods are made from stainless steel tubing and have holes drilled in them allowing free circulation of liquid or gaseous helium. The persistent switch of the solenoid is connected via an electrical feed-through to thin (36 gauge) insulated Cu wires outside the cryostat. The stainless tube and magnet are surrounded by a liquid helium dewar. A number of thin copper plates were soldered to the stainless tube, between the tube and helium dewar, providing radiation shields for heat and preventing the system from vibrating inside the dewar. The helium dewar sits inside a liquid nitrogen dewar and is isolated from it by means of a vacuum space. Initially the system was cooled to liquid nitrogen temperature, and then liquid helium was transfered into the inner dewar. Temperatures lower then 4.2 K (down to 1.7 K) were acquired by condensing helium in the sample space, and then lowering the pressure in the space using a mechanical pump. Temperatures higher than 70 K were not possible to control in this system due to the very fast boiling of liquid helium at such temperatures, the liquid being necessary for operating the superconducting magnet. SRA measurements at temperatures above 70 K were performed in a small cryostat system consisting of a liquid nitrogen dewar 5 cm in diameter isolated by a single vacuum space. The sample was mounted in a sample holder of similar design to that previously described for use in the low temperature SRA system, and placed into a narrow sample space of 1 cm diameter. The sample space was constantly pumped by a diffusion pump. Heating power was provided by a Cupron wire wound around the sample holder. Temperatures were measured using a

copper vs. constantan thermocouple with one junction placed on the sample rod and the reference junction immersed in liquid nitrogen. Magnetic fields up to 1.5 T were obtained using a conventional electromagnet. The constant current to the sample was supplied from KEITHLEY Model 224 Programmable Current Source. Measurements of the potential drop across both the sample and the thermocouple were taken using HP34401 multimeters. Data were collected by a computer with a GPIB card. In order to change the relative orientation of the magnetic field and sample current, the sample rod could be rotated around its axis through 90^0.

Chapter 5

Data Analysis and Discussion

5.1 AC Susceptibility and Magnetization

A detailed study of the ac susceptibility of $La_{0.33}Pb_{0.67}MnO_3$ was done in the region of the paramagnetic to ferromagnetic transition. Through an analysis of the magnetic susceptibility data an accurate value of a transition temperature can be determined, as well values for the critical-point exponents, providing an insight into the magnetic interactions present in this system.

5.1.1 Data Demagnetizing Correction

Before extracting any results from the raw data, these must be corrected for demagnetizing effects. The demagnetizing correction results from the geometrical shape and finite size of the specimen. When a specimen is magnetized by an external

magnetic field (H_a), uncompensated poles appear at its ends producing a so-called demagnetizing field within the specimen.The intensity of this field is proportional to the magnetization (M) with proportionality factor N, called the demagnetizing factor. The internal (actual) field (H_i) of the specimen is given as

$$H_i = H_a - NM \tag{5.1}$$

The demagnetizing factor for an "infinitely" thin specimen magnetized along its long axis is zero, while for a short and thick specimen it is large, $N \to 4\pi$ (1 in SI). The measured $La_{0.33}Pb_{0.67}MnO_3$ (LPMO) specimen has a rectangular shape and the demagnetizing factor along different axes was estimated from the slope of the low-field magnetization isotherms measured close to the critical temperature, shown in the figure (5.1). As the internal field (H_i) for a ferromagnetic material is always less than the applied field (H_a), the shape of the magnetization curves plotted against applied field has a limiting slope - the "shearing" curve. The set of such shearing curves measured at temperatures $\sim T_c$, when fields are applied along the longest axis is shown in figure (5.1). The slope of the initial linear portion of the M vs H_a curve, and the related demagnetizing factor, was determined from,

$$N = \left[\frac{\partial M}{\partial H_a}\right]^{-1}. \tag{5.2}$$

Here, it was assumed that the measured susceptibility has reached a demagnetizing limit of (1/N), a consequence of which is the divergence of the "true" susceptibility $(\partial M/\partial H_i)$(see below). For a specimen of ellipsoidal shape, which can be uniformly

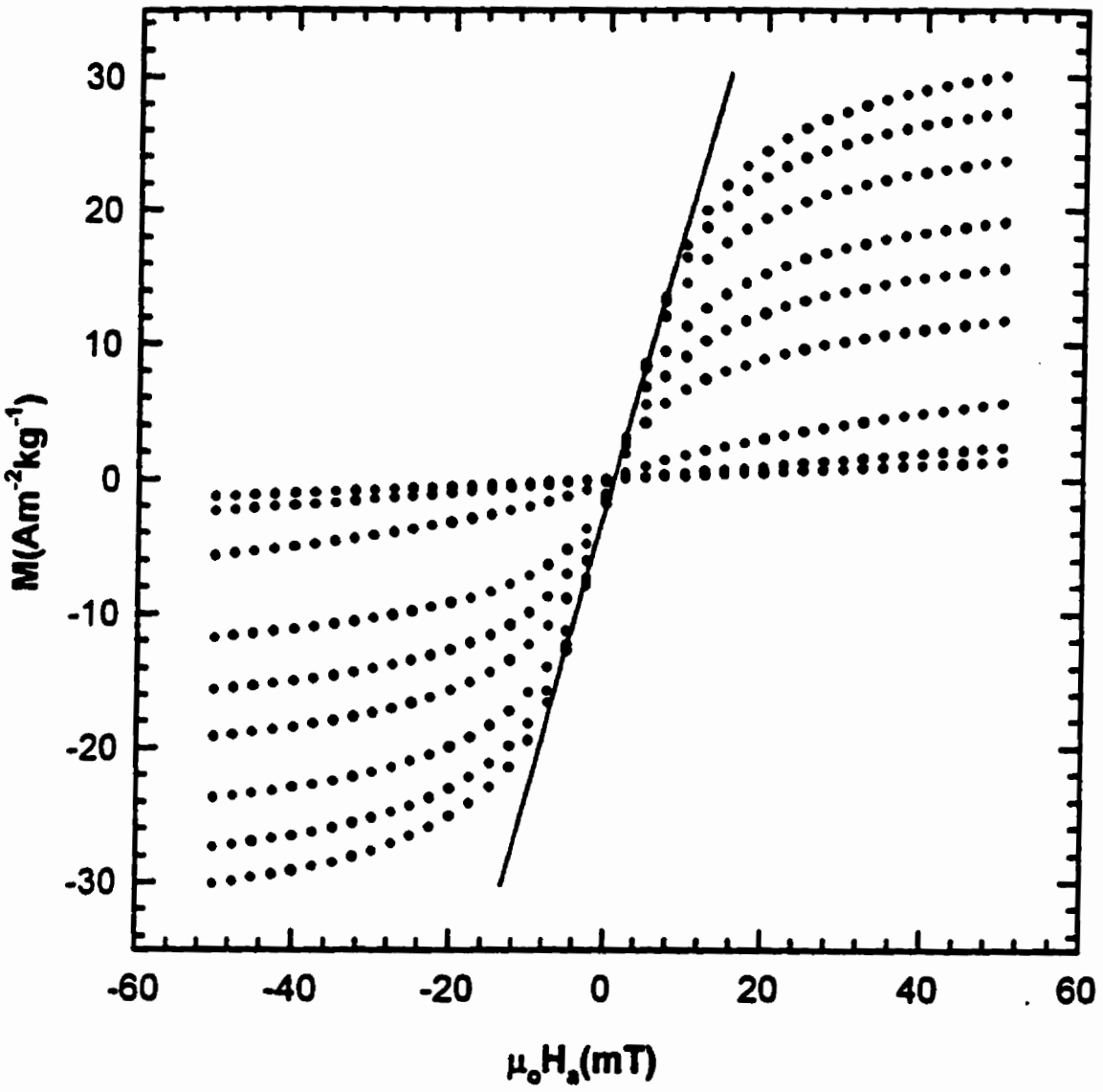

Figure 5.1: The magnetization M (in $Am^{-2}kg^{-1}$) measured in low applied fields $\mu_0 H_a$ (in mT) close to the ferromagnetic transition temperature. Here the applied field is parallel to the largest sample dimension with the solid line estimating the slope of the 'shearing' curve.

magnetized, the demagnetizing factor can be calculated exactly by evaluating the appropriate elliptical integrals [37]. Approximating the rectangular shaped sample by an ellipsoid with principal axes equal to the measured sample dimensions enabled the demagnetizing factors to be calculated. The calculated result for N along the longest axis agrees well with the measured value, while there is a discrepancy between calculated and measured N for the shorter axis. The corresponding calculated and measured values of N for the two configurations are 0.62 and 0.61 (along the longest sample dimension) and 5.13 and 3.93 (along the shorter axis) respectively. The values of the measured N were used to calculate the "true" susceptibility of the LPMO specimen,

$$\chi_t = \frac{\partial M}{\partial H_i} \tag{5.3}$$

as compared to the measured susceptibility,

$$\chi_m = \frac{\partial M}{\partial H_a}. \tag{5.4}$$

Using the expression (5.1) and the above definition for χ_m and χ_t yields

$$\chi_t = \frac{\chi_m}{1 - N\chi_m}. \tag{5.5}$$

Clearly, the measured susceptibility is limited to

$$\chi_m \leq \frac{1}{N}, \tag{5.6}$$

where the equality represents the demagnetizing limit at which the true susceptibility diverges, $\chi_t \rightarrow \infty$. In addition to measurements of the ac susceptibility, measurements

of the magnetization were also performed simultaneously. Knowing the magnetization M at a given temperature and the demagnetizing factor N enables the internal magnetic field to be calculated using the expression (5.1).

5.1.2 Zero-field AC Susceptibility

Before examining the susceptibility versus temperature curves in various applied fields it is interesting to consider the behaviour of the zero-field susceptibility $\chi_0(T)$ for $La_{0.33}Pb_{0.67}MnO_3$. The measurements were done at a frequency of 2.4 kHz with driving field amplitude of 3 μT, and raw data were analyzed as described previously to produce a curve of the true susceptibility versus temperature, which is consequently independent of sample size. The true zero-field susceptibility is shown in the insert in figure (5.2). χ_0(T) increases rapidly as the temperature is lowered through T_c and the system passes through the paramagnetic to ferromagnetic transition. The zero-field susceptibility exhibits a maximum near 320 K before decreasing slowly with further decrease in temperature. The principal maximum (or Hopkinson peak) in the zero-field response [38] results from technical contributions to the susceptibility, such as anisotropy and domain wall effects. The Hopkinson peak does not result from critical effects. It is clear from the insert in figure (5.2) that the zero field susceptibility does not approach its demagnetizing limit of 1/N (see section 5.1.1). This indicates prevailing anisotropy effects, discussed in more detail later in this thesis.

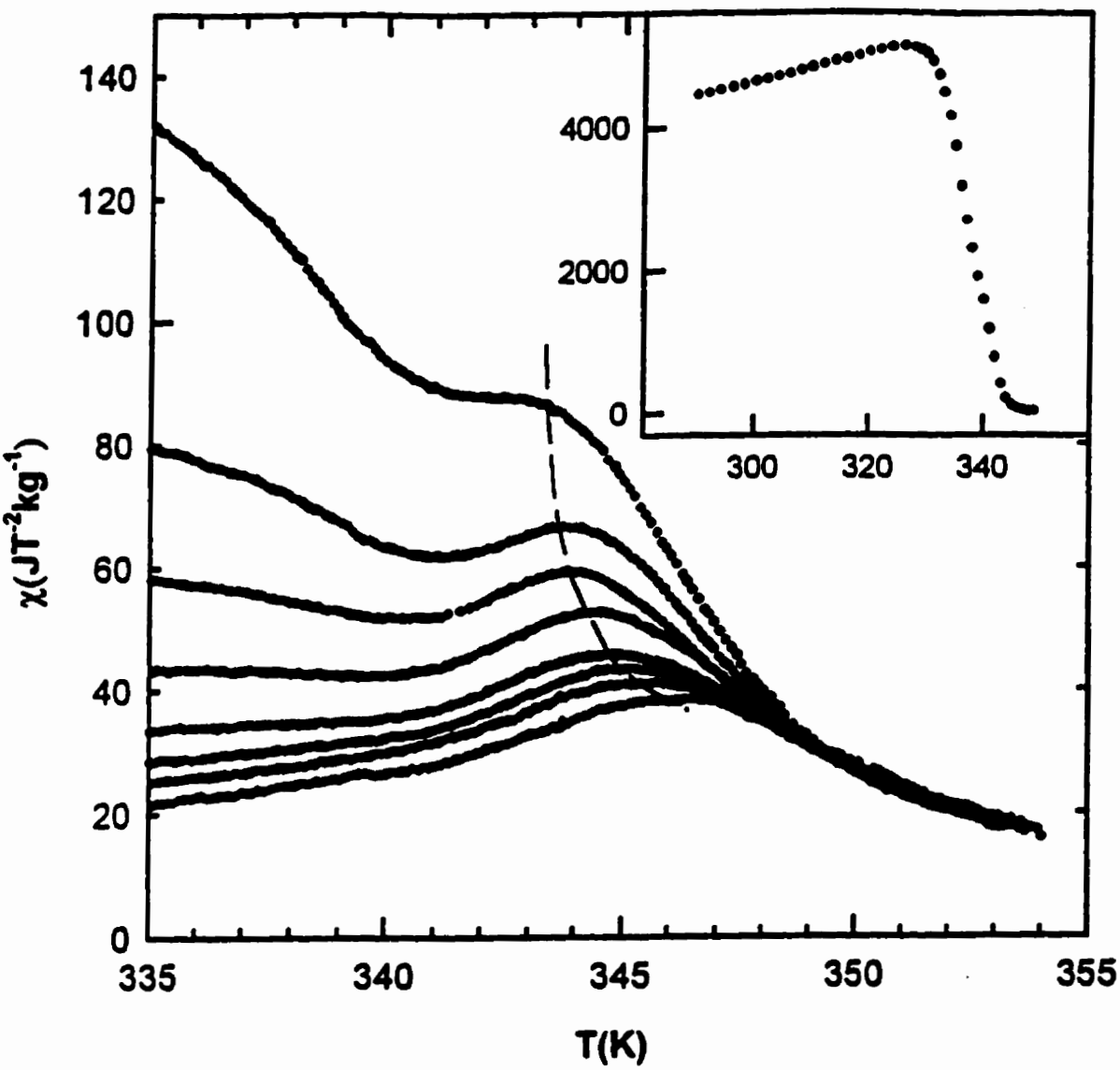

Figure 5.2: The temperature dependence of the ac susceptibility χ (in $JT^{-2}kg^{-1}$) plotted against temperature (in K) in the vicinity of the paramagnetic to ferromagnetic transition. The insert shows the zero-field susceptibility while the data in the main figure were taken in static biasing fields $\mu_0 H_a$ of between 30 and 100 mT increasing (from top to bottom) in steps of 10 mT. The dashed line designates the cross-over line.

5.1.3 AC Susceptibility Critical Behaviour

To observe the effects of critical fluctuations in the vicinity of a continuous magnetic phase transition, static biasing fields of 30 - 300 mT were superimposed on the ac driving field. Both ac and dc fields were applied parallel to the largest sample dimension. Such static fields suppress the technical background (the principal maxima) in both amplitude and temperature, enabling critical peaks to be resolved, as is evident in main body of the figure (5.2). This phenomenon has been reported in a variety of other systems, both metallic and semiconducting [14]. The critical, secondary maxima decrease in amplitude and move upward in temperature ($T_m > T_c$) as the static biasing field H_a increases. The locus of these critical maxima delineates the location of the cross-over line, represented as the dashed line in figure (5.2). Below this line the behaviour of the ac response is field-dominated whereas above this line it is controlled by thermal fluctuations. The fluctuation-dissipation theorem provides a qualitative understanding of the emergence of the critical peaks in finite fields [39], as the following argument shows. Consider the behaviour of the ac susceptibility in two limiting cases, at high temperature and low field, and at temperatures close to the critical temperature in increasing field,using the expression

$$\chi(H,T) \sim \frac{1}{T}\left(\langle S_z\rangle^2 - \left\langle S_z^2\right\rangle\right). \tag{5.7}$$

In the high temperature limit ($t \gg h$), $\chi(H,T)$ obeys the Curie-Weiss law (ch:3) giving $\chi(H,T) \sim 1/T$ as $\langle S_z\rangle \to 0$ and $\langle S_z^2\rangle \to S(S+1)$. Clearly, in this temperature

dominated region $\partial\chi/\partial t < 0$. In the field-dominated region when ($h \gg t$) consider $\lim_{T\to T_c^+} \chi(H_a, T)$ in finite field H_a. Approaching the critical temperature from above ($T \to T_c^+$) the magnetization is driven towards saturation in increasing fields, thus decreasing the (critical) fluctuations, and thus the susceptibility decreases as ($T \to T_c^+$), giving $\partial\chi/\partial t > 0$. This qualitative consideration shows that a maximum - the critical peak - must exist for $T > T_c$ between these two limiting constraints. The result that the temperature T_m of the critical maxima moves upward while the amplitude $\chi(H_a, T_m)$ decreases with increasing field H_a is consistent with the general formalism based on the static scaling law description of such a transition [40], and also with detailed numerical solutions of a particular model - the ferromagnetic phase of Sherrington- Kirkpatrick like (S-K) model [41]. Within the latter, this peak evolution is consistent, as expected, with mean field exponent values.

A quantitative analysis of such data is based on the conventional static scaling law equation of state, which express the (reduced) magnetization m in terms of the usual linear scaling fields ($h \sim H_i/T_c$) and ($t = |T - T_c|/T_c$), where H_i is the internal field and T_c is the critical temperature; i.e.

$$m = t^{\beta} F\left(\frac{h}{t^{\gamma+\beta}}\right) \tag{5.8}$$

Alternatively

$$\chi(h,t) = \frac{\partial m}{\partial h} = t^{-\gamma} G\left(\frac{h}{t^{\gamma+\beta}}\right) = h^{1-\frac{1}{\delta}} H\left(\frac{h}{t^{\gamma+\beta}}\right) \tag{5.9}$$

in which $H(X) = X^{\gamma/(\gamma+\beta)}$, where G is the derivative of the unknown scaling function F, and the Widom equality is assumed to hold ($\gamma = \beta(\delta - 1)$) (sec:3.5). From this

latter form in equation (5.9), it can be seen that susceptibility measurements carried out in fixed field (for which prefactor $h^{1-\frac{1}{\delta}}$ is constant) as a function of temperature map out the dependence of H(X) on its argument X (in which temperature appears in the denominator). Furthermore the assertion of scaling theory that F - and hence H and G - is a universal function of this argument means that any feature evident in H(X), such as the maxima shown in figure (5.2), should appear at the same value X_c of this argument. This leads directly to

$$t_m = \frac{T_m - T_c}{T_c} \propto H_i^{\frac{1}{\gamma+\beta}} \tag{5.10}$$

where T_m is the temperature of the maxima evident in figure (5.2). In addition, as the argument $X = X_c$ is a constant at these maxima, so are the functions $H(X_c)$ and $G(X_c)$ themselves, when, from the initial form of equation (5.2)

$$\chi(h, t_m) \propto t_m^{-\gamma}. \tag{5.11}$$

Thus the peak susceptibility displays the same dependence on temperature as does zero-field susceptibility immediately above T_c. The latter two relationships derived from equation (5.9) describing the behaviour of the critical peaks are considered in the light of the experimental data collected. The expression (5.10) contains two unknowns, namely T_c, the critical temperature, and the so called cross-over exponent $\gamma + \beta$. An estimate for T_c was found by plotting the peak temperature T_m against $H_i^{1/\gamma+\beta}$ as shown in figure (5.3). The internal field H_i ($H_i = H_a - NM$) at each temperature was estimated from the simultaneously measured magnetization and

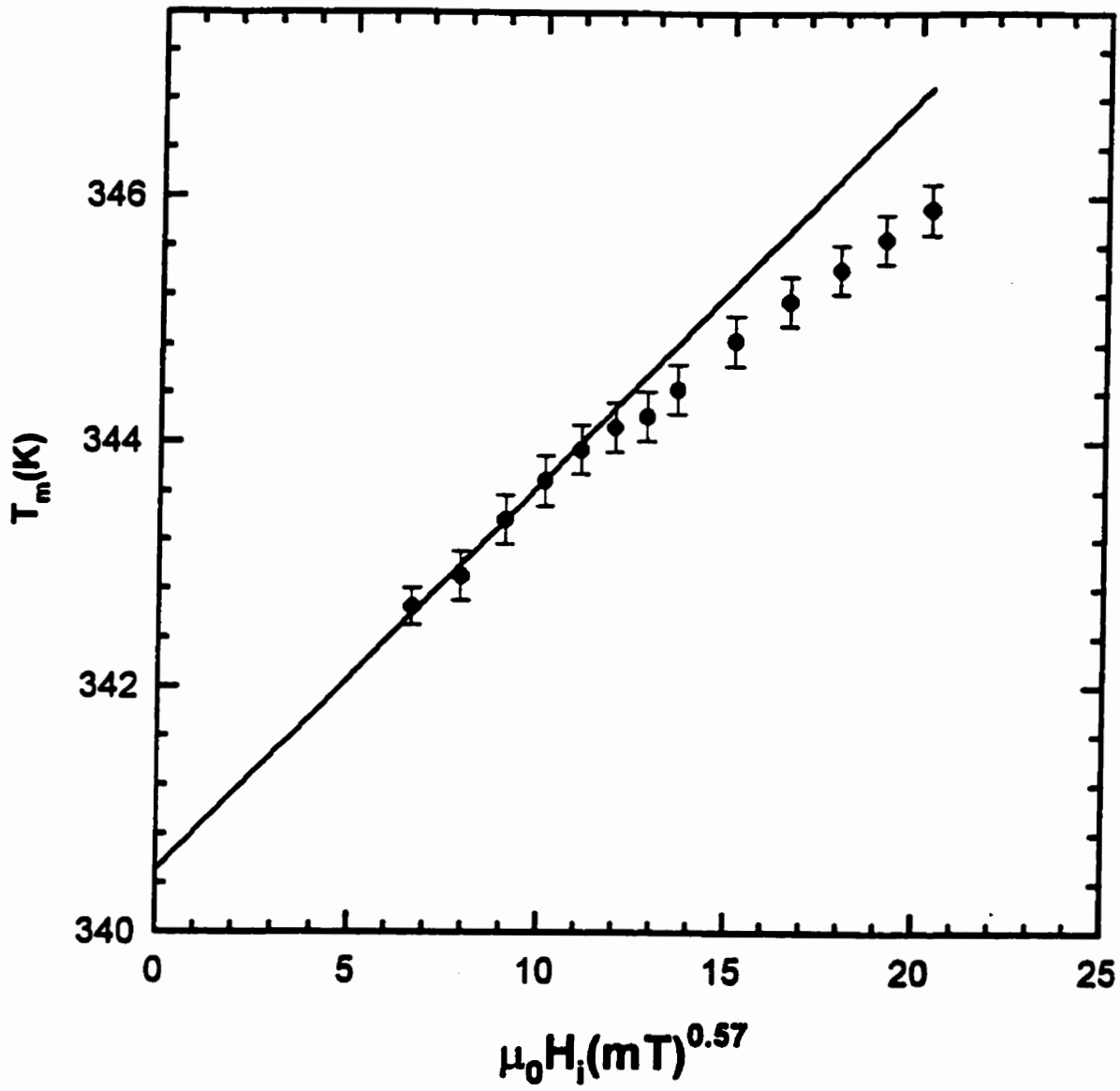

Figure 5.3: The ac susceptibility peak temperature T_p (in K) plotted against $(\mu_0 H_i(inT))^{1/\gamma+\beta}$ where H_i is the internal field and Heisenberg model exponents are adopted ($(\gamma+\beta)^{-1} = 0.57$). The intercept of the straight line drawn yields an estimate for T_c.

the slope (N^{-1}) of the low field (shearing) curves (fig: 5.1). Such plots have been constructed using a wide range of exponent values, although it was initially assumed that the measured system belonged to a particular universality class with appropriate values of $\gamma + \beta$. An initial value for $1/(\gamma + \beta) = 0.5$ was used for a first estimate of T_c from the intercept of the best-fit line , given by

$$T_m \approx const.(H_i)^{.5} + T_c. \tag{5.12}$$

This estimate for T_c was then used in equation (5.10) to find an "improved" value of the exponent $\gamma + \beta$. Such an iteration process was repeated until consistent values for T_c and $\gamma + \beta$ were determined. In figure (5.3) deviations away from the single power-law behaviour summarized in equation (5.10) are evident at higher fields. The best-fit line is fitted through the first six points, i.e. those closest to T_c, which is appropriate considering the asymptotic nature of the scaling law ($h \rightarrow 0, t \rightarrow 0$). The most consistent "fits" are obtained with values of $(\gamma + \beta)$ close to those predicted by the isotropic, nearest-neighbour three dimensional Heisenberg model [42], viz. $\gamma + \beta = 1.75$, which are used in this figure (5.3). The intercept of this "fit" provides an estimate for T_c of 340.5 $\pm$ 0.5 K. At this point it is important to point out that the behaviour reproduced in figure (5.3), in particular the T_c estimate, is essentially independent of the exponent values chosen (mean field, 3-d Heisenberg, etc.). This estimate for the ferromagnetic ordering temperature from the magnetic data is in very good agreement with that deduced from the transport measurements (339.6 $\pm$ 0.4), particularly since these data sets were acquired in different cryostats incorporating

different thermometry (the absolute accuracy of which is typically ± 0.5 - 1 % in either system). The estimate of T_c = 340.5 K was then used in constructing other scaling plots from the magnetic data, as detailed below. An independent value for the critical exponent γ was found using the equation (5.11). The susceptibility peak amplitudes from figure (5.2) are plotted against the reduced temperature t on a double logarithmic scale, as shown in figure (5.4). This plot also depends on the value chosen for T_c. The straight line drawn in this figure is a best fit to the first eleven points, those approaching the asymptotic limit most closely. The straight line fit verifies the power-law prediction of equation (5.11), with a slope yielding $\gamma = 1.39$. This value is in close agreement with the 3-dimensional Heisenberg model prediction of 1.386. This result provided a principal impetus for investigating overall consistency with this latter model exponent values. With the uncertainties evident in figure (5.4), the range of slopes that will fit these data yield

$$\gamma = 1.39 \pm 0.06.$$

Figure (5.5) assesses the applicability of Heisenberg model exponents in describing the field-induced increase in the temperature of the crossover line. The reduced peak temperature t_m ($t_m = T_m - T_c/T_c$) as a function of the internal field H_i is plotted on the double logarithmic scale. An unrestricted best fit to the first five points in this figure yields $(\gamma + \beta)^{-1} = 0.54$. This is somewhat lower than the Heisenberg model value of 0.57, which is actually shown in this figure. The latter provides an acceptable fit, although deviations are evident. As can be seen in figure (5.5), there

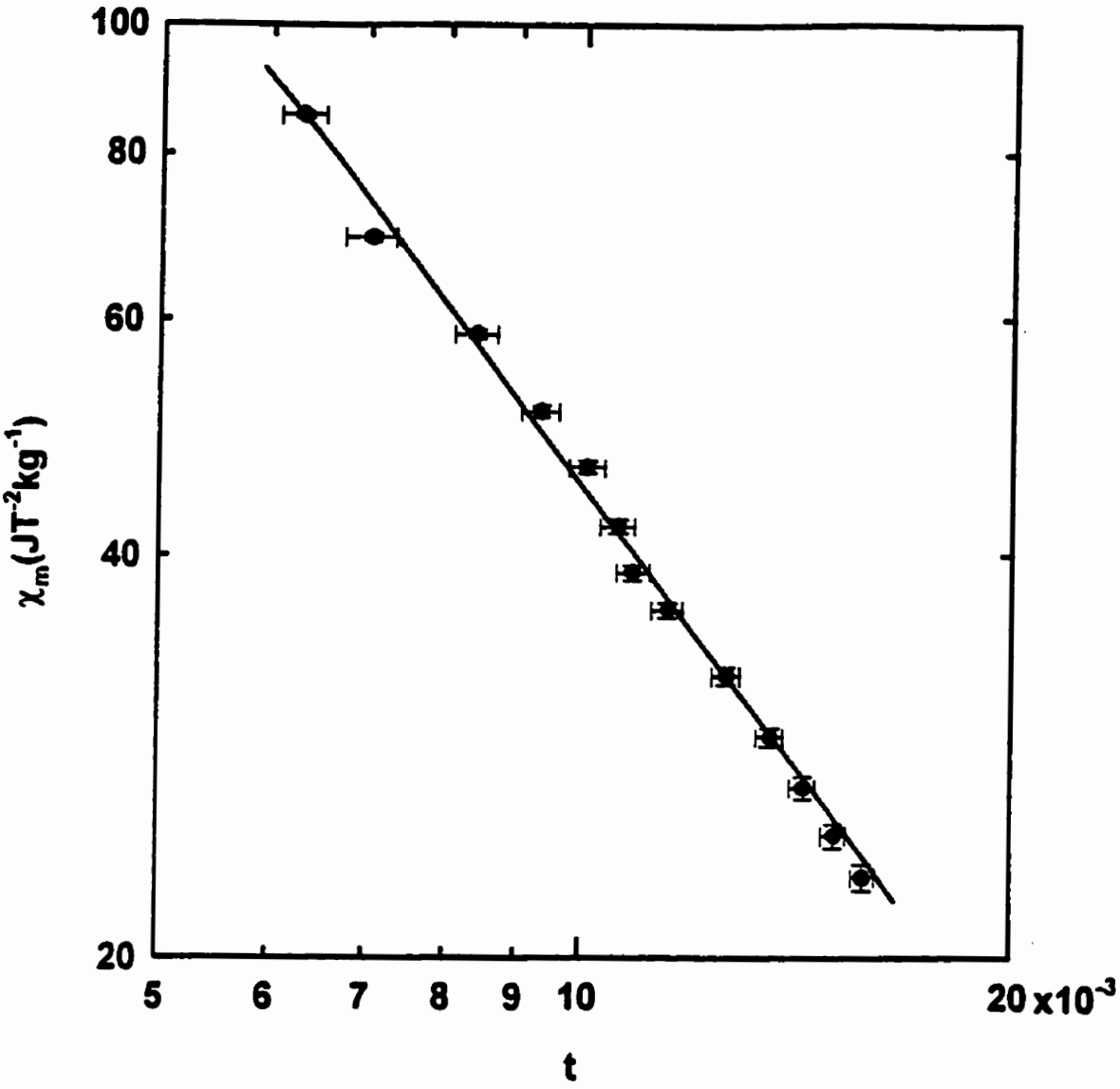

Figure 5.4: The field dependent ac susceptibility peak amplitude χ_p (in $JT^{-2}kg^{-1}$) - taken from data similar to those shown in figure (5.2) - and plotted against the reduced temperature t on a double logarithmic scale. The slope of the line drown not only confirms the power-law prediction of eq:. (5.11) but also yields $\gamma = 1.39$.

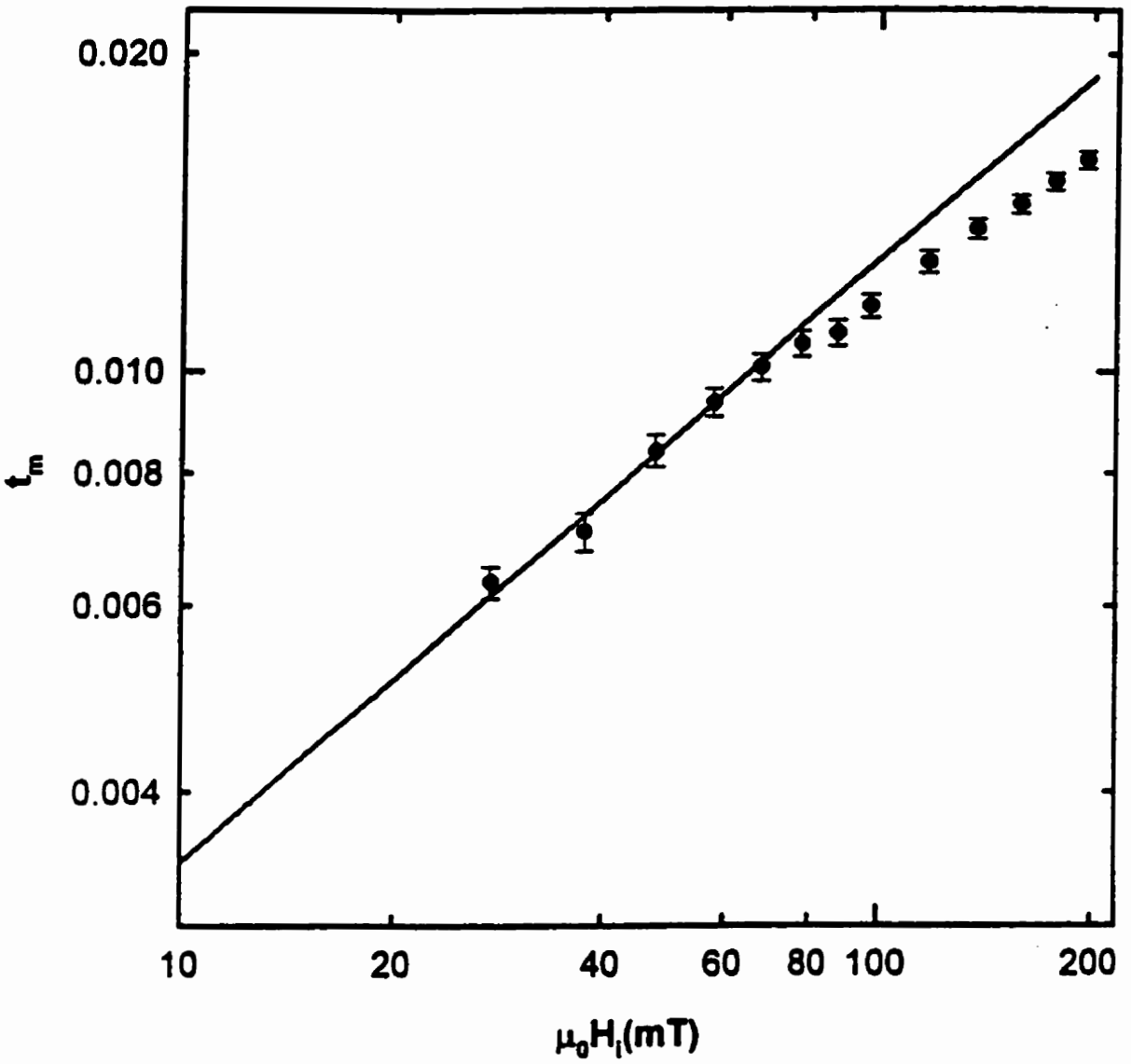

Figure 5.5: The field dependent ac susceptibility peak temperature t_m plotted against the internal field $\mu_0 H_i$ (in mT) on a double logarithmic scale. The straight line drawn corresponds to the power-law prediction of eq:. (5.10) with Heisenberg model exponents

is some curvature in the plot at high field values, so that fitting the entire data set would clearly reduce the estimate for $(\gamma+\beta)^{-1}$. The effective susceptibility exponent γ^*, also known as the Kouvel-Fisher susceptibility exponent, is defined as

$$\gamma^*(t) = \frac{d[\ln \chi(0,t)]}{d[\ln t]}. \tag{5.13}$$

γ^*, shown in figure (5.6), can be found by plotting the zero-field susceptibility $\chi(0,T)$ against reduced temperature t, $(T > T_c)$ on a double logarithmic scale, and then finding the local slope of the curve. Finally, the exponent δ was determined, aided by a knowledge of the critical temperature. Figure (5.7) reproduces the magnetization data acquired along the critical isotherm and plotted on a double logarithmic scale against the internal field. The straight line drawn confirms the power law prediction of equation (5.8) for this isotherm, viz

$$m \propto H_i^{\frac{1}{\delta}} \tag{5.14}$$

with the slope of the line drawn corresponding to $\delta = 4.2(\pm 0.15)$ for $20 \leq H_i \leq 10^3$ mT. The latter is well below the 3-dimensional Heisenberg model value of 4.80, and possible reasons for this are discussed below. An estimate of the coercivity of the material at various temperatures within the ferromagnetic region were taken from "butterfly loop" measurements, viz. measurements of the susceptibility as a function of applied field (fig:5.8). Such measurements essentially represent the local slope of the hysteresis loop for the material. Assuming that the region of highest slope in the hysteresis loop is at the coercive field H_c, the separation between the two peaks

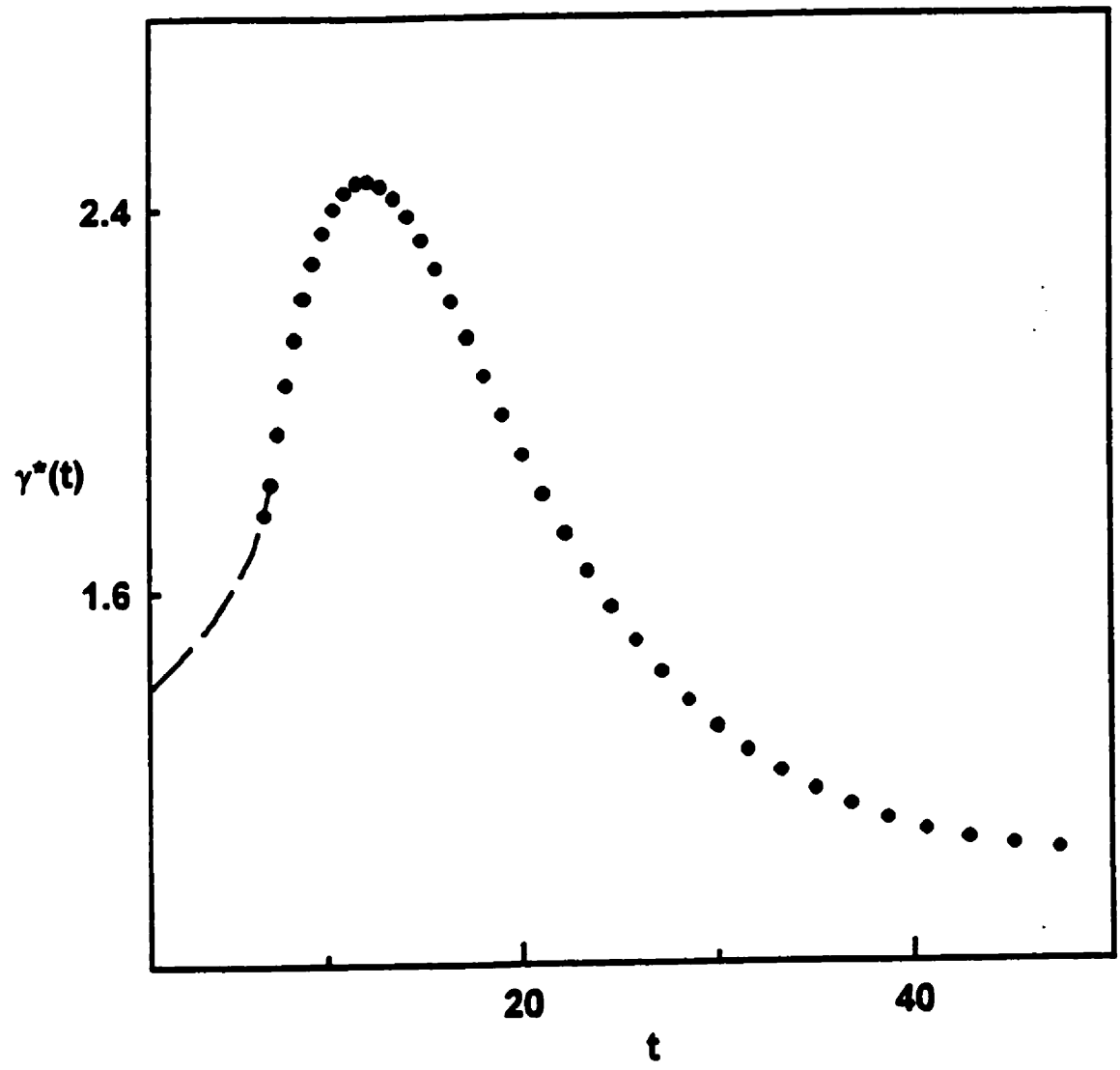

Figure 5.6: The behaviour of the effective Kouvel-Fisher (zero-field) susceptibility exponent γ^*.

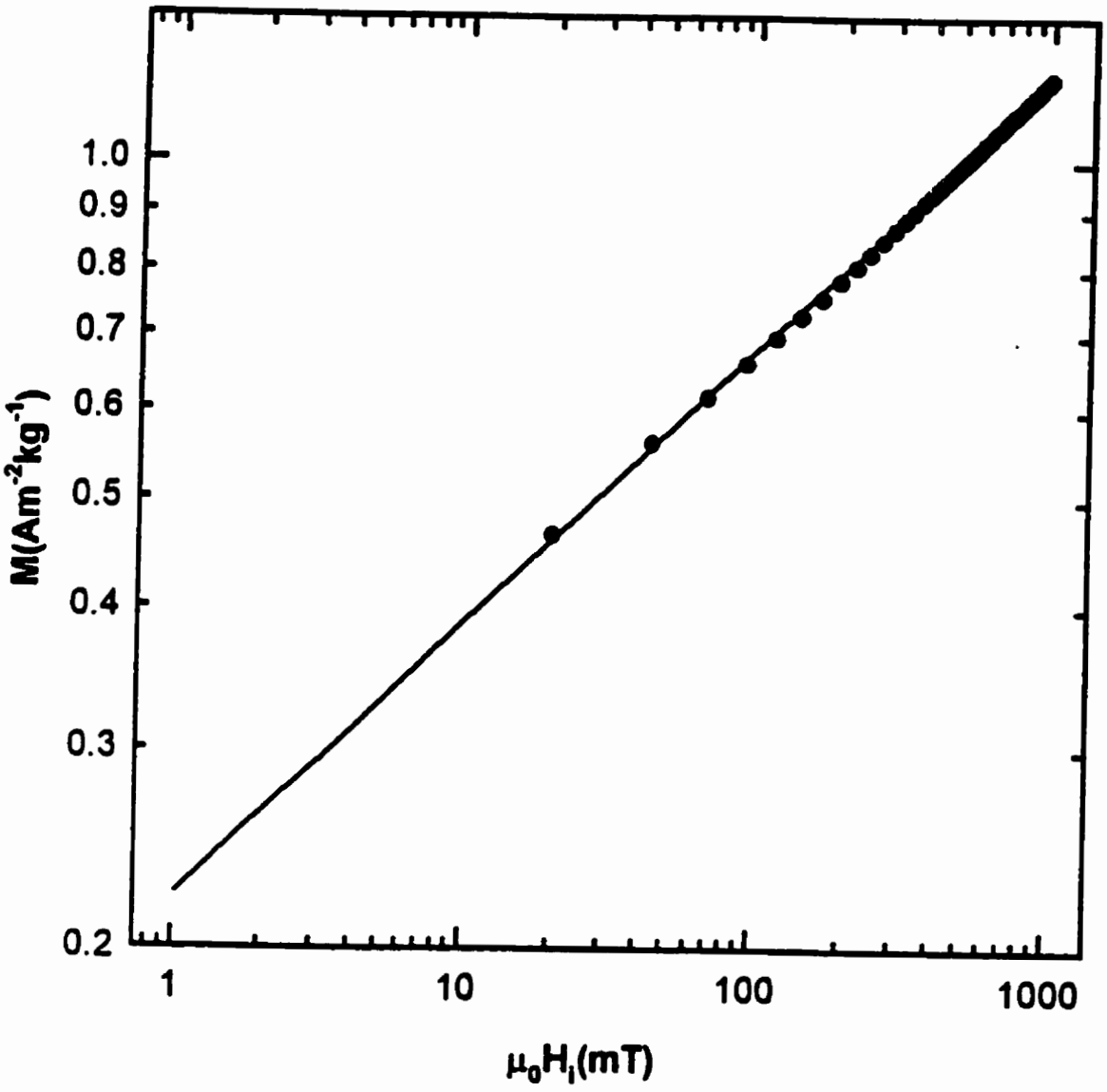

Figure 5.7: The magnetization M (in $Am^{-2}kg^{-1}$) measured along the critical isotherm, plotted against the internal field $\mu_0 H_i$ (in mT) on a double logarithmic scale. The slope of the line drawn yields $\delta = 4.2$.

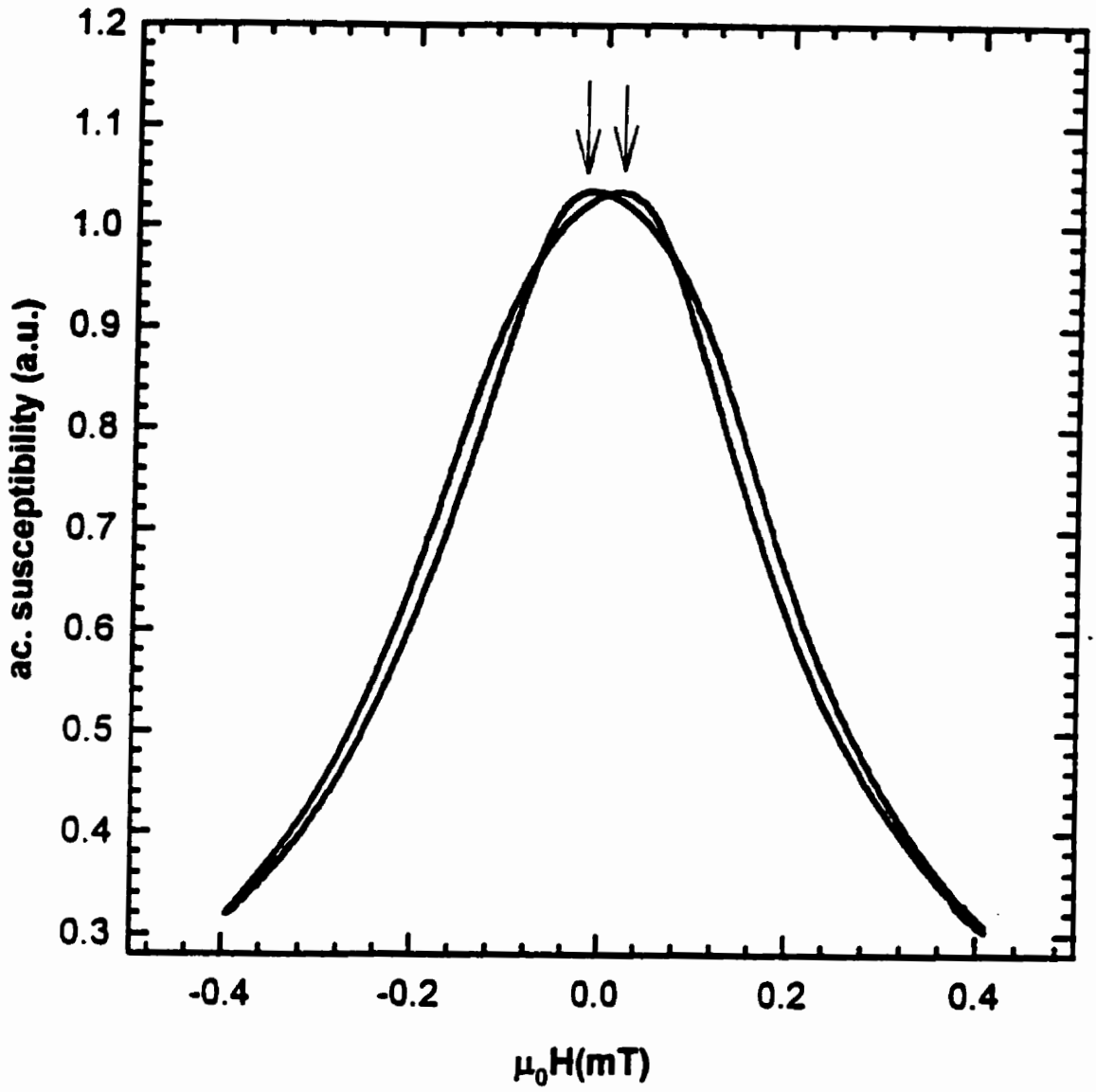

Figure 5.8: Butterfly plot of the ac susceptibility versus applied field at 77 K The splitting between the peaks is taken to be twice the coercive field.

in the "butterfly loop" plots is twice the coercive field. Figure (5.9) reproduces the temperature dependence of the estimated coercive field H_c. The coercive field H_c collapses to zero near $T_c \simeq 340$ K, and saturates at a value of about 1.6 mT below 250 K, somewhat lower than that reported recently for a similarly prepared ceramic $La_{0.67}Ca_{0.33}MnO_3$ bulk sample [43], and roughly an order of magnitude lower than LCMO films [44].

5.1.4 Discussion: Critical Behaviour

Having decided to investigate the overall applicability of Heisenberg model exponents, at this point it is appropriate to discuss possible causes of the deviations from the values of this model. Consider the deviation of the power-law behaviour evident in figure (5.5) at higher fields. Indeed, close examination of figure (5.4) also indicates an increase in slope and hence in the effective susceptibility exponent γ^* (fig: 5.6) beyond $t \simeq 5 \times 10^{-2}$, while the data in figure (5.5) display marked concave curvature above $t_m \sim 10^{-2}$ consistent with an increase in the sum of the corresponding effective exponents $(\gamma^* + \beta^*)$ beyond that point. The effective exponent β^* is also given through a Kouvel-Fisher type expression, as follows

$$\beta^* = \frac{d[\ln m(0,t)]}{d[\ln t]}. \tag{5.15}$$

Effective exponent values which change with increasing temperature or field are an established feature of coupled spin systems in which the spin-spin exchange coupling constants display some variance about a mean value. The previous investigation of

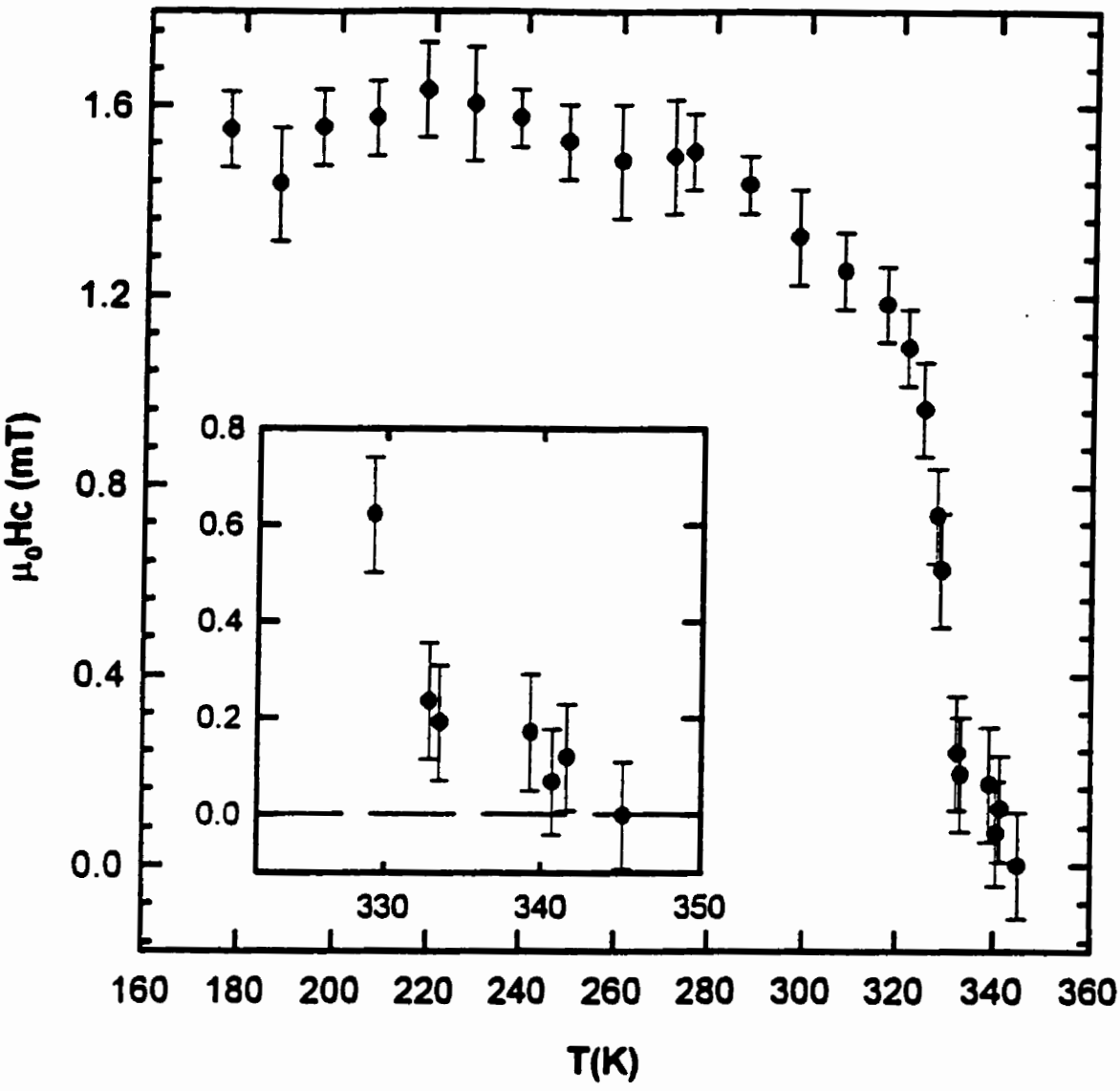

Figure 5.9: The coercive field $\mu_0 H_i$ (in mT), estimated from butterfly loop measurements, plotted against temperature (in K). The insert shows the behaviour close to the ferromagnetic transition temperature T_c.

metallic systems with such characteristics [14, 45, 46] indicate that the "disorder" - measured typically by the variance in the distribution of coupling strengths - is an irrelevant scaling field at the critical point (t = 0, h = 0), so that the asymptotic exponent values are unchanged from the "pure" system in agreement with the Harris criterion. The "disorder" does however cause the effective exponent values to change as field and/or temperature is varied away from the critical point [14, 45, 46]. Various model calculations of such effects have been performed, and figures (5.10) and (5.11) reproduce the temperature dependence of $\beta^*(h)$ and $\delta^*(h)$ in the S-K model mentioned previously [47] The initial increase in $\beta^*(h)$ from its asymptotic value (β_0) shown in figure (5.10) is qualitatively consistent with the behaviour of the data reproduced in figure (5.5). The S-K - like model is based on a mean-field approach and yields consequently an asymptotic value for $\beta_0 = 0.5$. Such calculations thus reproduce correctly the trend observed experimentally, although the mean-field nature of the S-K model cannot reproduce the correct asymptotic value for β_0 (0.5 in S-K model, c.f. 0.365 in the Heisenberg model). It should also be noted that these calculations utilize a Gaussian distribution of exchange coupling constants (sec:3.6), whereas that characterizing the present system is likely bimodal. The dominant component in this latter distribution is ferromagnetic, arising from double exchange between Mn^{4+} and Mn^{3+} ions, while the other component is antiferromagnetic, resulting from Mn^{3+} - Mn^{3+} interactions. The latter interaction is the so called t_{2g} - O($2p_\pi$) - t_{2g} superexchange interaction and it is prevalent in the undoped host. In the "bimodal" distribution

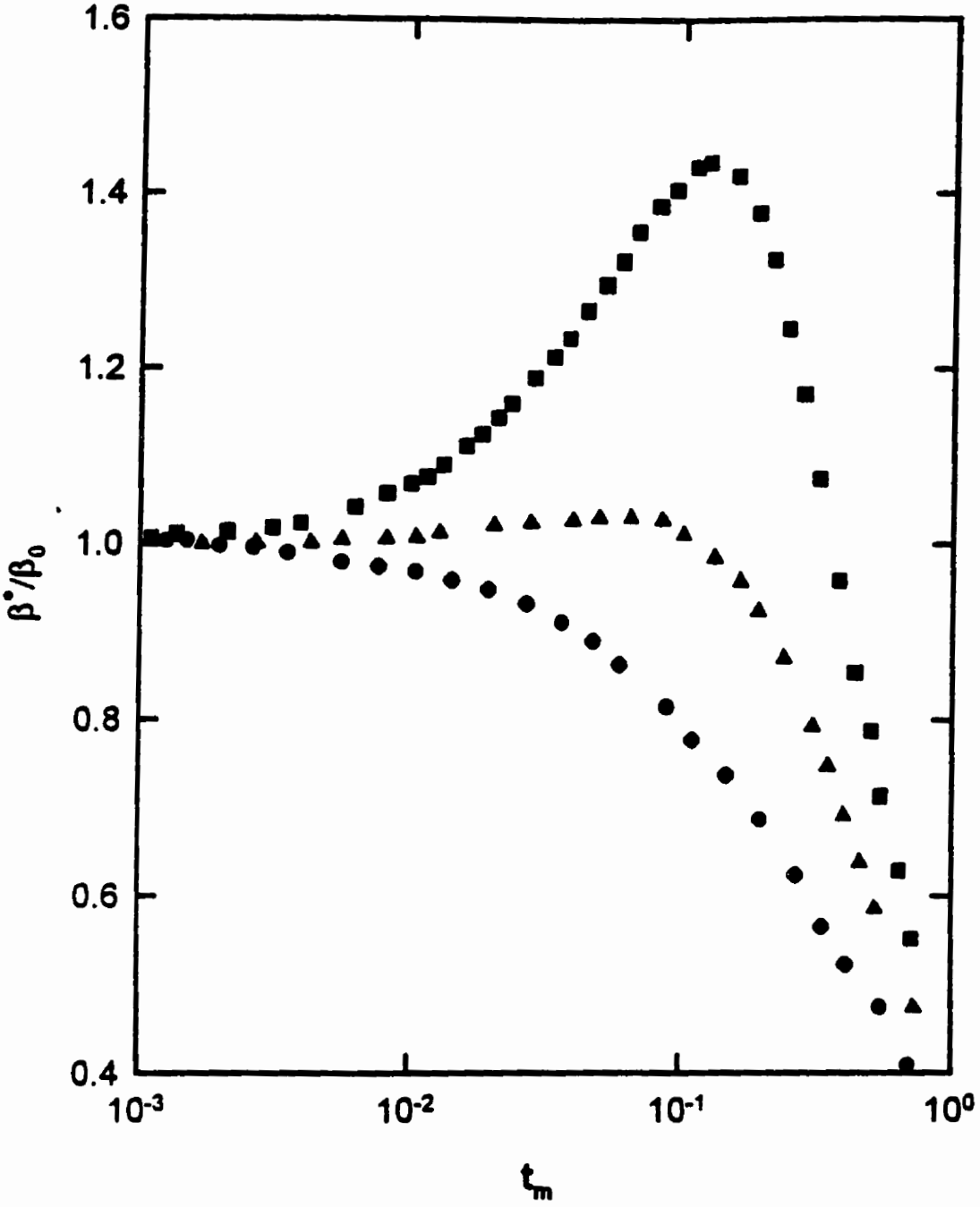

Figure 5.10: The ratio of the effective Kouvel-Fisher exponent β^* to its asymptotic value β_0 calculated from the ferromagnetic phase of an S-K like model, plotted against the reduced susceptibility peak temperature t_m. The symbols correspond to (■)η = 1.27, (▲)$\eta = 2$, (•)$\eta = \infty$

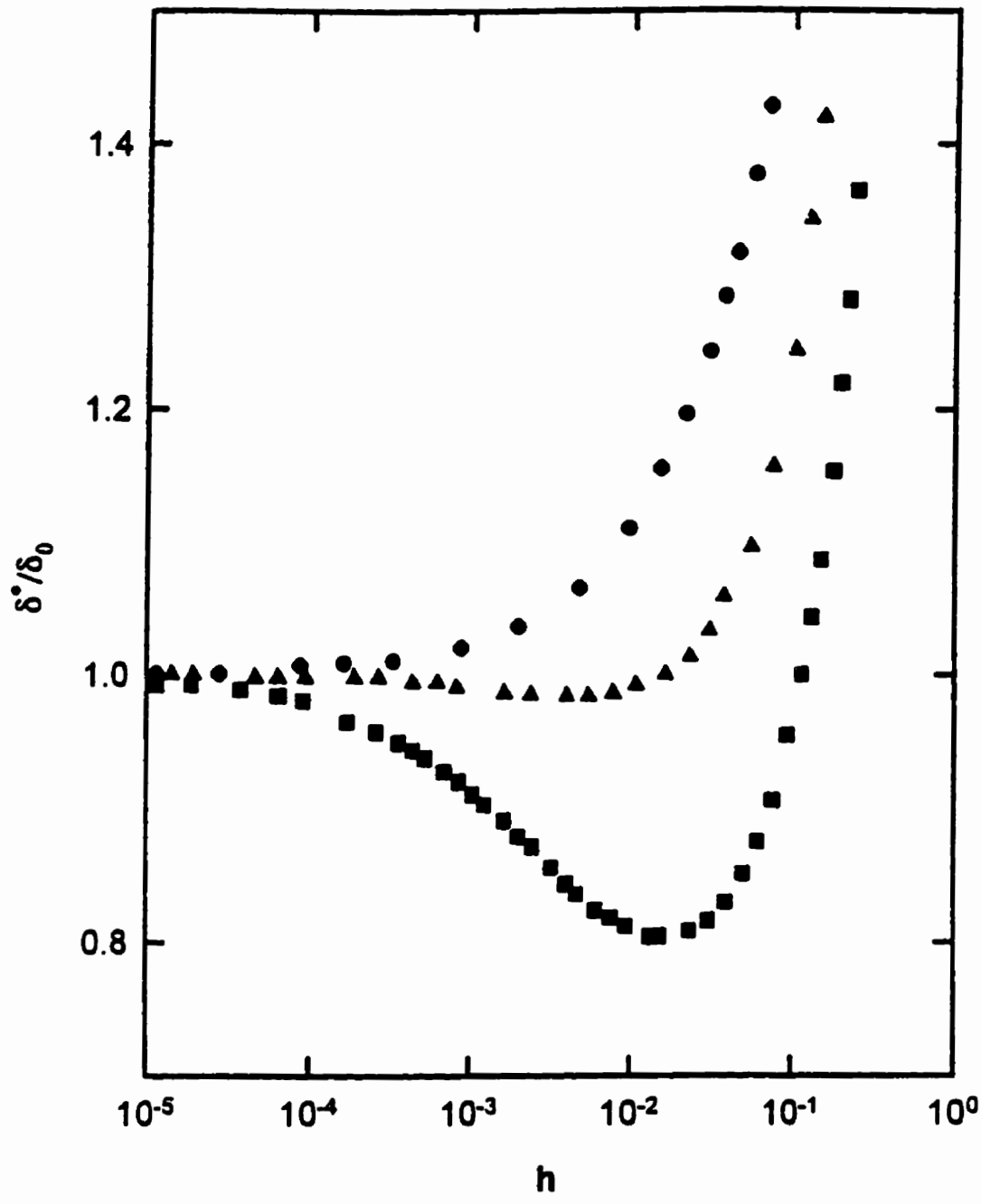

Figure 5.11: The ratio of the effective exponent δ^* to its asymptotic value δ_0 calculated from the local slope of the critical isotherm at the ferromagnetic boundary in an S-K like model; symbols as in figure (5.10).

each interaction is weighted appropriately by the proportion of Mn^{3+} and Mn^{4+} ions, i.e. the doping level. Thus in the inhomogeneous mixed valent state (Mn^{3+} - Mn^{4+}) of these perovskites, in those regions that are statistically rich in the dopant species (Pb here) and hence in Mn^{4+} sites, double exchange and consequently ferromagnetic correlations would predominate. By contrast in environments in which Pb is statistically deficient, Mn^{3+} - Mn^{3+} interactions would predominate thus nucleating antiferromagnetic coupling. Available calculations [48] suggest that differences in the distribution profiles should not influence significantly the trends described above. The mean field nature of the S-K model, in which $\gamma(T) = \gamma^*(T)$, cannot reproduce the trends evident in figure (5.6) for $\gamma^*(T)$, although other approaches incorporating exchange coupling disorder have been invoked [49]. To summarise, the analysis of the magnetic data given above admits the following alternatives.

An unrestricted best fit to data closest to the critical point ($t = 0, h = 0$) yields

$$\gamma = 1.39 \pm 006; \beta = 0.41 \pm 0.02; \delta = 4.2 \pm 0.15$$

These estimates satisfy the Widom equality ($\gamma = \beta(\delta - 1)$) within experimental uncertainty ($\delta - 1 - \gamma/\beta = 0.2 \pm 0.27$), however they do not agree with the predictions of any specific model. Nevertheless the estimates for δ and β agree, again within listed uncertainty, with the corresponding estimates reported recently [50] for single crystal $La_{0.7}Sr_{0.3}MnO_3$ ($\delta = 4.25 \pm 0.2, \beta = 0.37 \pm 0.04$), although the estimate for γ in that system (1.22 ± 0.03) is lower than that found here.

Alternatively, arguments incorporating the effects of exchange bond disorder, as out-

lined above, appear to suggest that asymptotic estimates for γ and β in the present system might be compatible with Heisenberg model predictions. This can be also extended to δ value estimates. Specifically, as depicted in figure (5.11), the effect of "disorder" depresses the estimate for this exponent below its true asymptotic value for data acquired away from the critical point, $h = 0$. A reduction in the effective δ^* value of some 13 % from its (assumed) asymptotic value would reproduce the measured value, and while this reduction is considerable the model calculation reproduced in figure (5.11) shows that this is achievable for $\eta \sim 1.3$ ($\eta = J/J_0$ being the ratio of the first to second moment of the distribution of exchange coupling constants) in the fields utilized here ($h = g\mu_B H_i/k_B T_c$). It is, furthermore, not inconsistent with the variations displayed by the other effective exponents. In conclusion, both of the above suggestions must remain as possible explanations of the magnetic response of this Pb-doped manganite. This situation could be resolved, in principle, by measurement closer to the critical point. Such measurements are, however, precluded by the presence of a significant regular (i.e. noncritical) contribution(s) to the response which obscures the emerging critical peak structure and hence the critical response, as is clearly apparent in figure (5.2). Applied fields in excess of 20 - 30 times the coercive field H_c (fig:5.9) values are necessary for the first observation of the critical peak structure, more than an order of magnitude larger than those required in conventional systems. In general the coercive field H_c provides a measure of the applied field necessary to suppress the regular response; past experience suggests that

in the vicinity of T_c applied fields of roughly two to three times H_c are usually sufficient. This result is emphasized in figure (5.12); here each constant field susceptibility curve or isokap, normalized to its corresponding maximum value, is plotted against the scaling function argument $(t/h^{1/\gamma+\beta})$. This procedure should produce a universal curve, i.e. an experimental determination of the functional dependence of H(X) given in equation (5.9). It is evident in this figure that data above the maximum, in the thermally dominated regime, scale onto a universal curve, while those below this maximum in the field dominated domain do not. It should be noted that for conventional soft ferromagnets [51] experimental data do collapse onto a universal curve in both regimes. In many non-perovskite systems previously studied, the presence of such a regular component, which is not driven to technical saturation in relatively low fields, has been associated with an anisotropy/coercivity arising from single ion spin -orbit coupling [14, 45, 52]. It would be tempting to attribute this coercivity to the presence of Mn^{3+} ions (Mn^{4+} is not Jahn-Teller ion), a corollary of which would be that this system should also display a spontaneous resistive anisotropy, already reported for the other divalent dopants, and which is considered in the following section.

5.2 Transport Measurements

The resistance of the Pb-doped manganite specimen was measured as function of the temperature at various fields and, also as a function of the magnetic field at various temperatures for two different configurations of the magnetic field and current. Both

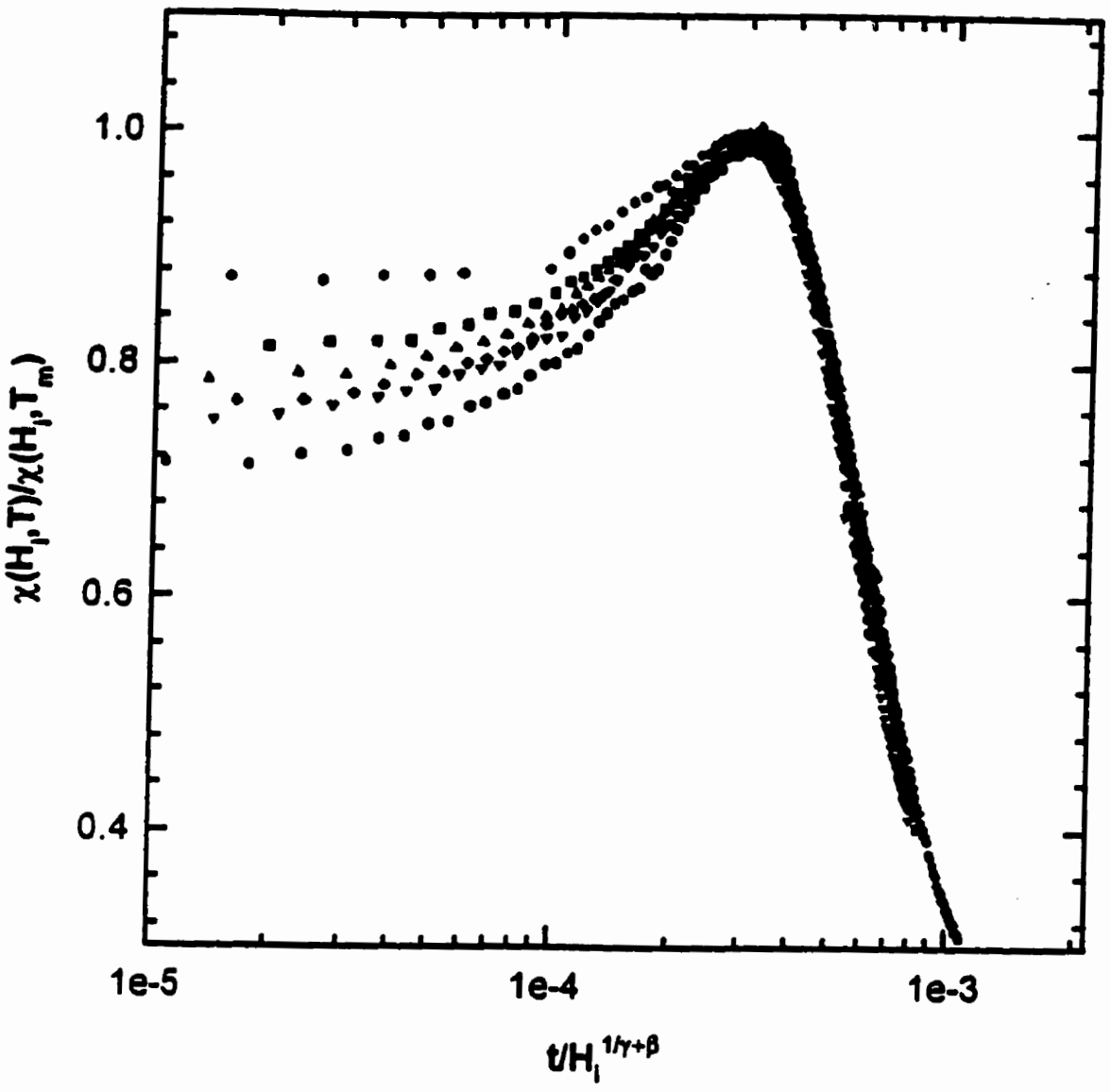

Figure 5.12: The 'scaling plot' for $La_{0.33}Pb_{0.67}MnO_3$. These data are the "isokaps" shown in figure (5.2) with the susceptibility normalized to the respective peak values, plotted against the argument $t/h^{1/\gamma+\beta}$ of the scaling function. Note that the data do not collapse to the universal curve in the field dominated region below the peak.

$\rho(T)$ and $\rho(H)$ in temperature range from 1.7 to 70 K were measured using the relative difference ac method (sec:4.3.1); here, having measured the voltage drop V_0 across the sample at some predetermined initial temperature (usually 4.2 K), the voltage change $\Delta V(H_a)$ induced by a change in magnetic field ΔH_a and also the change $\Delta V(T)$ due to a change in temperature ΔT are estimated with a high precision. By the simple addition of the changes of the latter type, $V_0(T)(= V_0 + \sum \Delta V(T))$ and $V_0(H)(= V_0 + \sum \Delta V(H_a))$ can be found, and corresponding resistivities $\rho(T)$ and $\rho(H)$ estimated by knowing the sample current and the conventional form factor. Above 70 K a dc technique was used and the raw data were converted to the corresponding resistivities using Ohm's law and a knowledge of the form factor. In addition, detailed analysis of the Spontaneous Resistive Anisotropy (SRA) was performed. Magnetoresistance measurements for the parallel ($\|$) and perpendicular ($\perp$) configuration of the applied magnetic field and current were taken. The resistance was calculated from raw data, as described above and the spontaneous resistive anisotropy (SRA) was found using the approach indicated in figure (5.13). The SRA is usually defined by the ratio [27]

$$\frac{\Delta\rho}{\rho_0} = \left[\frac{\rho_{\|}(B) - \rho_{\perp}(B)}{\frac{1}{3}\rho_{\|}(B) + \frac{2}{3}\rho_{\perp}(B)}\right]_{B\to 0} \tag{5.16}$$

which characterizes the difference between the longitudinal and transverse magnetoresistance of a technically single domain ferromagnet extrapolated to zero induction, roughly the transport equivalent of the spontaneous magnetization. The extrapolation implicit in equation (5.16) is usually performed from a field region sufficiently high to technically saturate the sample. The arrows in figure (5.13) show the region

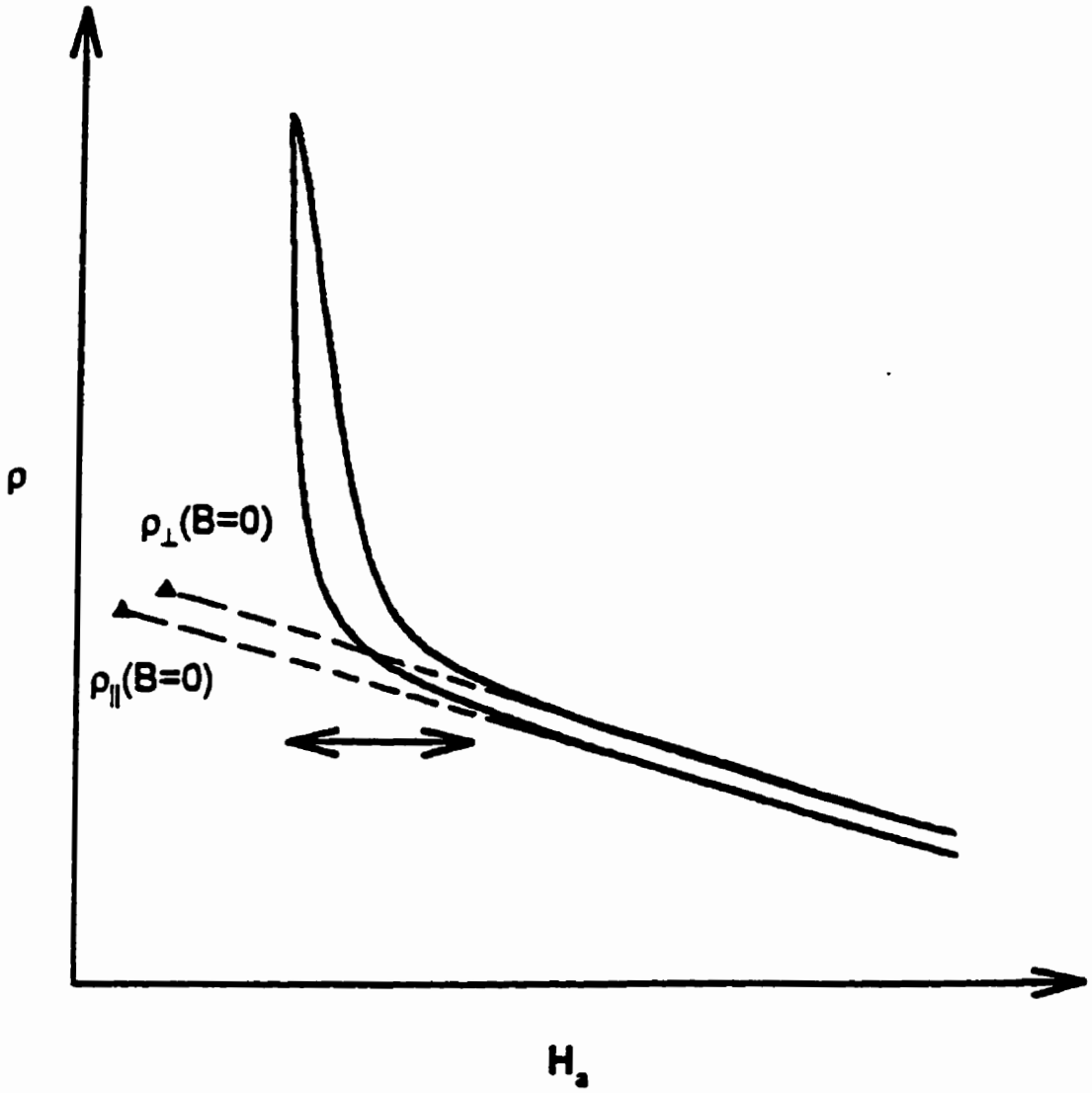

Figure 5.13: Schematic extrapolation for a $\rho(H)$ resistivity curves to B=0. The heavy lines indicate observed resistivity as function of field when the field is applied parallel ($\|$) or perpendicular ($\perp$) to the current direction. The arrows show the region of incomplete technical saturation. Dotted line indicate extrapolation from the saturated region to the respective B=0 (▲) points.

of incomplete saturation. The change in resistivity in the low field region depends on the exact domain structure and is not well defined. Dashed lines in figure (5.13) extrapolate the resistivity from the saturated region to the respective point of zero induction, calculated from

$$0 = \mu_0 H_a + M(\mu_0 - N). \tag{5.17}$$

N is the demagnetizing factor for transverse or longitudinal fields, estimated from "shearing" curves as described previously. The magnetization M was estimated by plotting the measured magnetic moment (for both configurations of magnetic field and current) against H_a^{-1} and extrapolating the data to the limit $H_a^{-1} \rightarrow 0$. The average magnetization, used in equation (5.17), was found from

$$\bar{M} = \frac{1}{3} M_{\parallel} + \frac{2}{3} M_{\perp}. \tag{5.18}$$

5.2.1 Zero-Field Resistivity

Figure (5.14) reproduces the temperature dependence of the zero-field resistivity $\rho(T)$ of the polycrystalline ceramic $La_{0.33}Pb_{0.67}MnO_3$ specimen, the same as the one used in magnetic measurements, between 1.7 and 380 K. These data are in good overall agreement with existing measurements on this system [53], so little comment on them is necessary. This specimen displays semiconducting behaviour ($d\rho/dT < 0$) above 350 K, the latter being the temperature of the resistivity maximum, below which an abrupt transition to metallic-like transport ($d\rho/dT > 0$) occurs. The weak,

broad "bulge" between 150 and 300 K is attributable to sample granularity [54, 56, 55]. The resistivity is believed to be influenced by the presence of the grain boundaries which act as strong spin-scattering centers for conduction electrons [54]. In addition the probability for conduction electrons to cross a boundary may also be lowered by interfacial tunneling due to differences in magnetic order between the grain surface and grain core [56]. The insert in the figure (5.14) shows the derivative of these data in the temperature range 330 - 345 K, an interval that embraces the onset of the metal-insulator transition. This derivative peaks at 339.6±0.4 K, giving a transition temperature that is in good agreement with the critical temperature, deduced from magnetic measurements (T_c = 340.5 K) and, emphasizing a correlation between magnetic and transport properties for the perovskites.

5.2.2 Magnetoresistance and Spontaneous Resistive Anisotropy

Having briefly discussed the zero field transport data (fig:5.14), the detailed behaviour of the effects of an external magnetic field on this $La_{0.33}Pb_{0.67}MnO_3$ specimen are now presented. Figure (5.15) displays the longitudinal ($\rho_{||}$) and transverse ($\rho_{\perp}$) magnetoresistance at 4.2 K in fields up to 3 T. In both orientations the low field magnetoresistance ($\mu_0 H_a < 0.5T$), falls sharply, as shown in the insert, an effect often attributed to grain boundary effects [44], with the large difference evident between the two orientations originating principally from demagnetizing field effects (estimated to

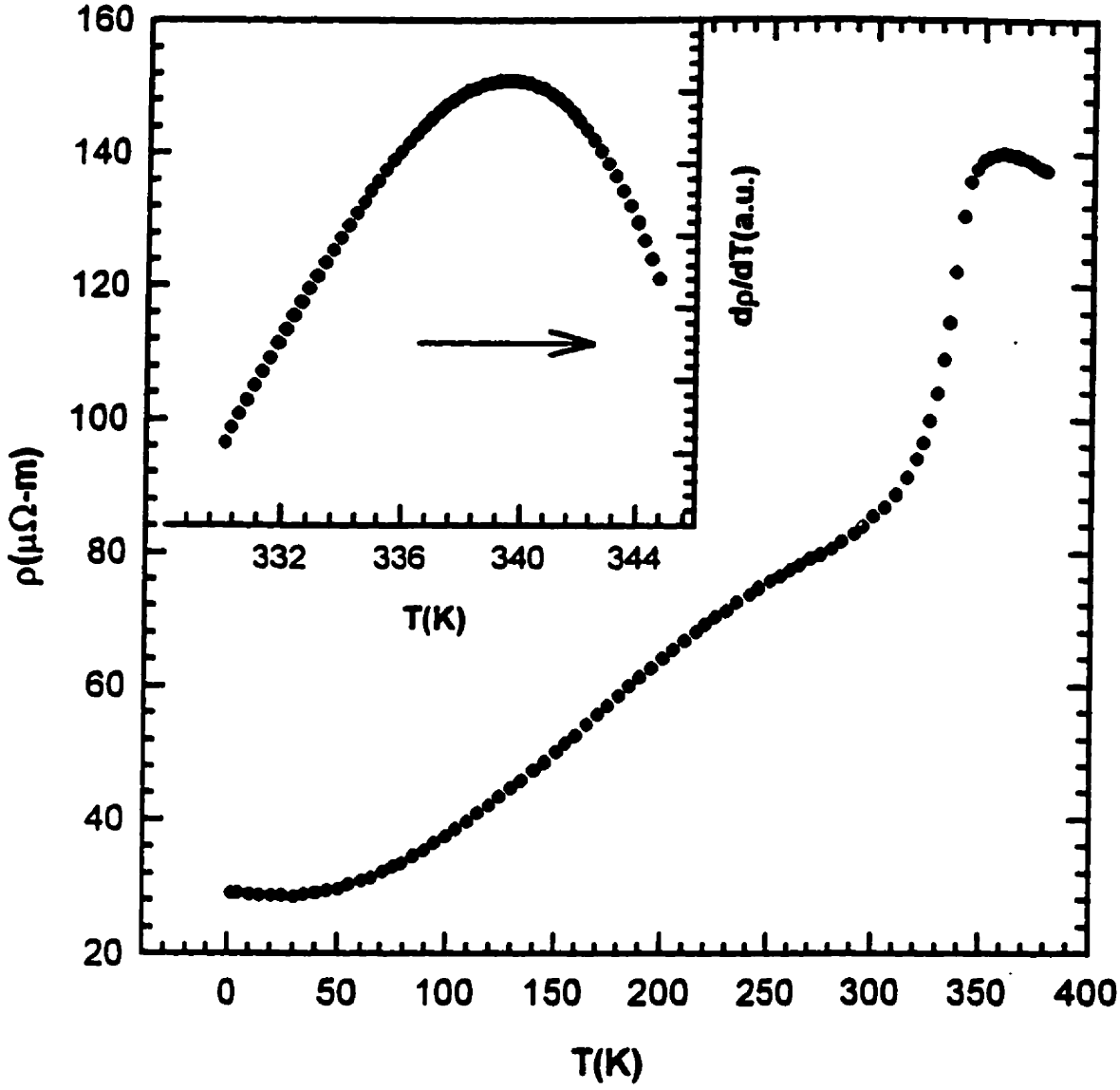

Figure 5.14: The zero-field resistivity ρ (in $\mu\Omega - m$) plotted against temperature (in K); the insert shows the derivative $d\rho/dT$ (in arbitrary units) in the vicinity of the metal-insulator transition.

be about $\leq$ 0.2 T). At higher fields ($\geq$ 1 T) there is a much smaller, essentially linear decrease in $\rho(H_a)$ with increasing field H_a. The low field region of the curves shown in the insert in the figure (5.15) depends on the prevailing domain structure which is, in turn, history dependent and hence not well defined [27]. The extrapolation shown by the dashed lines in this figure, are fits to the data beyond $\mu_0 H_a \sim 1T$ where a simple linear, essentially parallel, fit reproduces the data for both orientations very well. The difference in demagnetizing factor for the two orientation results in the condition B = 0 being attained in applied fields $\mu_0 H_a$ differing by the $\sim$ 0.2 T as mentioned above. The value estimated for SRA at 4.2 K using this approach is -0.2(1) $\pm$ 0.03 %. Since a non-vanishing SRA requires both a polarizing field and spin -orbit coupling at scattering sites in either an itinerant [27, 30, 29] or a localized model approach [27, 57], this result is qualitatively consistent with the presence of Mn^{3+} ions. Both the sign and magnitude of this effect in the Pb-substituted system is similar to that reported for epitaxial films of $La_{0.67}Sr_{0.33}MnO_3$ at the same temperature [58] and for post-annealed films of $La_{0.7}Ca_{0.3}MnO_3$ on $SrTiO_3$ at higher temperatures [44].

Before discussing both the size and the temperature dependence of the SRA in this substituted perovskite, two further comments on the behaviour evident in figure (5.15) are appropriate. First, in metallic ferromagnets the change in $\rho_{||}$ and $\rho_{\perp}$ with applied field beyond technical saturation is usually attributed to Lorentz force considerations resulting from cyclotron curvature effects. The latter cause $\rho_{||}$ and $\rho_{\perp}$ to increase with field whereas the opposite trend is evident here; furthermore cyclotron curvature ef-

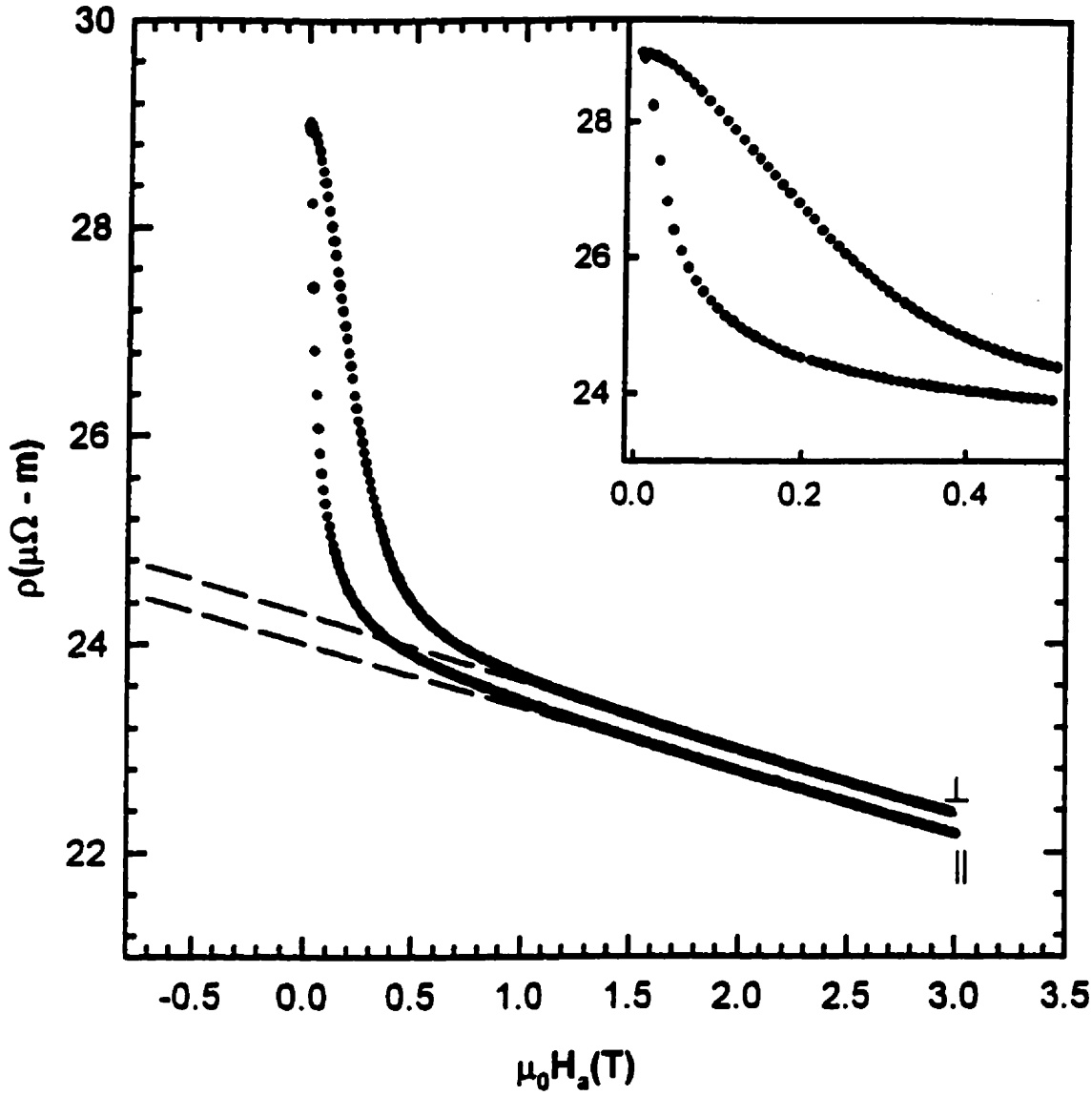

Figure 5.15: The resistivity ρ (in $\mu\Omega - m$), measured in the transverse ($\perp$) and longitudinal ($\parallel$) configurations at 4.2 K, plotted against the applied field $\mu_0 H_a$ (in T). The dashed lines are linear extrapolations from the high field region. The insert shows low field behaviour in more detail.

fects are generally very small in the present field range for residual resistivities greater than $10^{-2} - 10^{-1}\mu\Omega m$ [59]. The decrease in magnetoresistivities beyond $\mu_0 H_a \sim 1T$ evident in figure (5.15) likely arise from some degree of non-collinearity in the spin system, as confirmed qualitatively by the corresponding magnetization data (fig: 5.16). Qualitatively however, the fractional change in the magnetoresistance between 1 and 3 T is nearly an order of magnitude larger then the corresponding magnetization change. Secondly, the low field magnetoresistive behaviour reproduced in the insert in figure (5.15) indicates that while the behaviour evident in this regime indicates a clear anisotropy in this response, a quantitative characterization of these effects from such data might be misleading since they can appear exaggerated by demagnetizing effects. The field sweeps for both configurations, parallel and perpendicular, were measured in the temperature range between 1.7 and 360 K. Figures (5.17) and (5.18) showed selected curves of the magnetoresistivities at a variety of temperatures between 10 and 330 K, from which the SRA has been estimated in the manner described above. These data also indicate a monotonic decrease in the low field magnetoresistance with increasing temperature, a feature referred to later. Figure 19 summarizes the temperature dependence of the SRA so obtained.

5.2.3 Discussion: Spontaneous Resistive Anisotropy

Such data have been interpreted using two complementary models both relying on the existence of spin-orbit coupling and a polarizing field at scattering sites. One

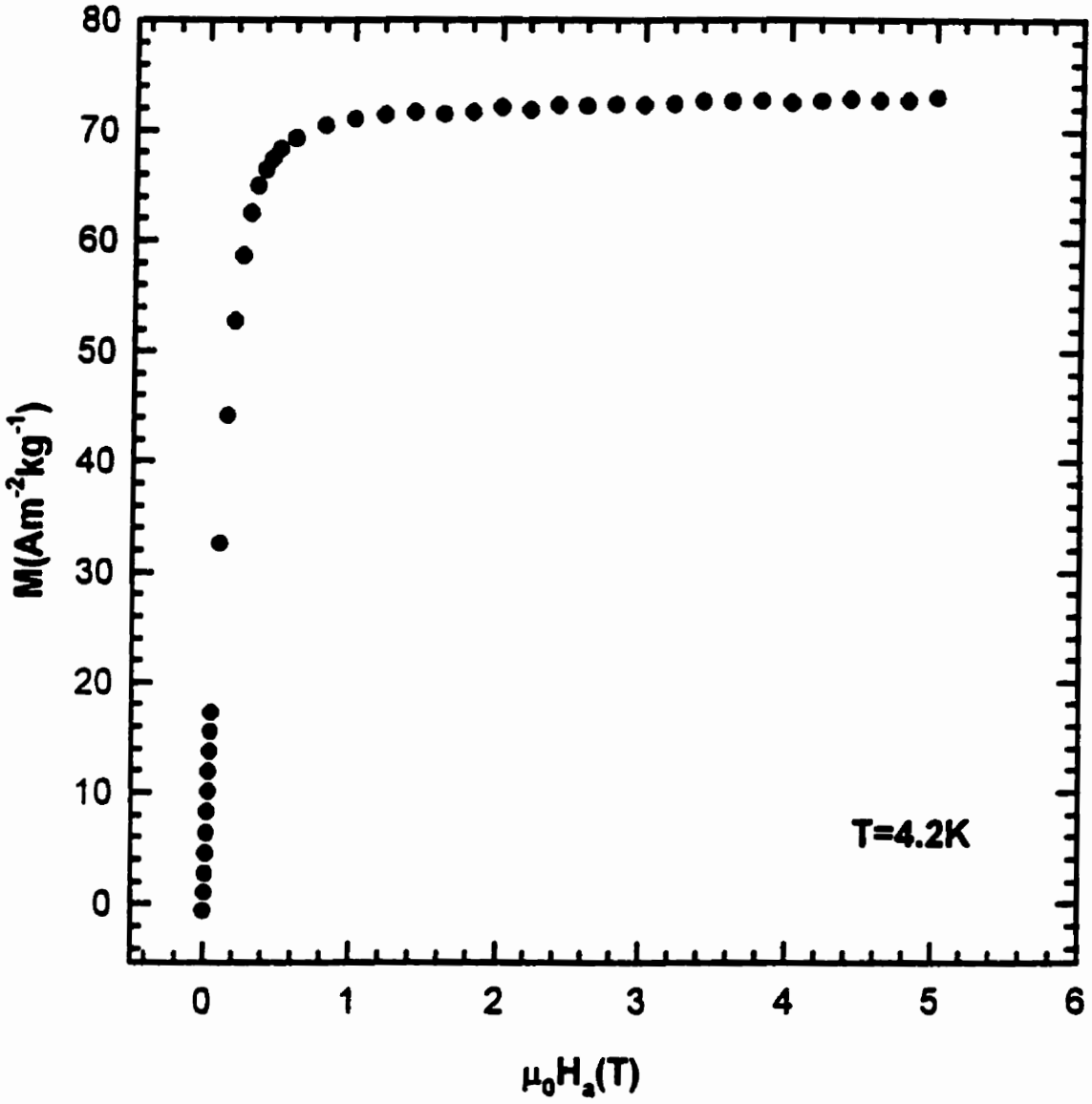

Figure 5.16: The magnetization M (in $\mathrm{Am}^{-2}kg^{-1}$) measured at 4.2 K, plotted against the applied field $\mu_0 H_a$(in T) with the latter applied parallel to the largest sample dimension.

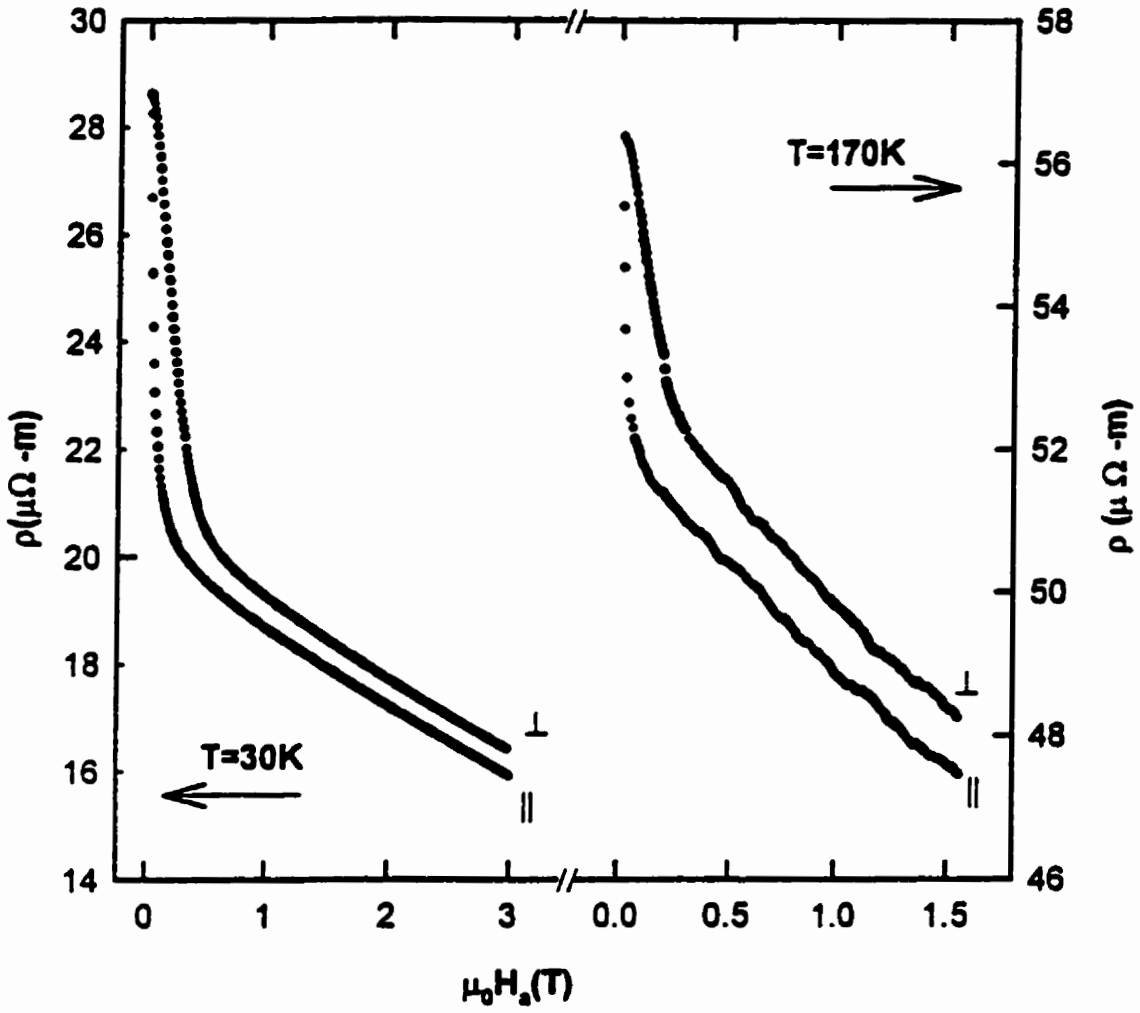

Figure 5.17: The resistivity ρ (in $\mu\Omega - m$), measured in the transverse ($\perp$) and longitudinal ($\parallel$) configurations at 30 and 170 K, plotted against the applied field $\mu_0 H_a$ (in T).

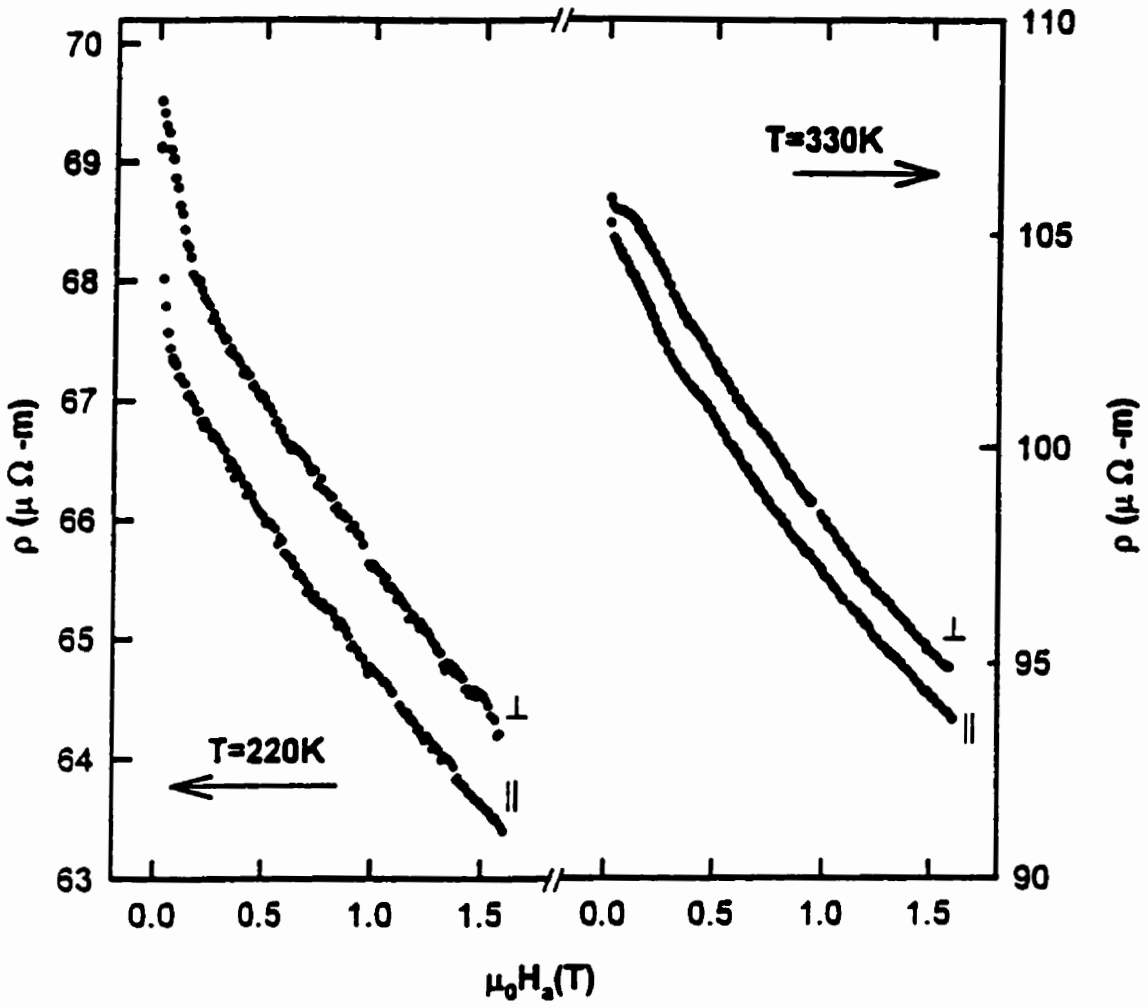

Figure 5.18: The resistivity ρ (in $\mu\Omega - m$), measured in the transverse ($\perp$) and longitudinal ($\|$) configurations at 220 and 330 K, plotted against the applied field $\mu_0 H_a$ (in T).

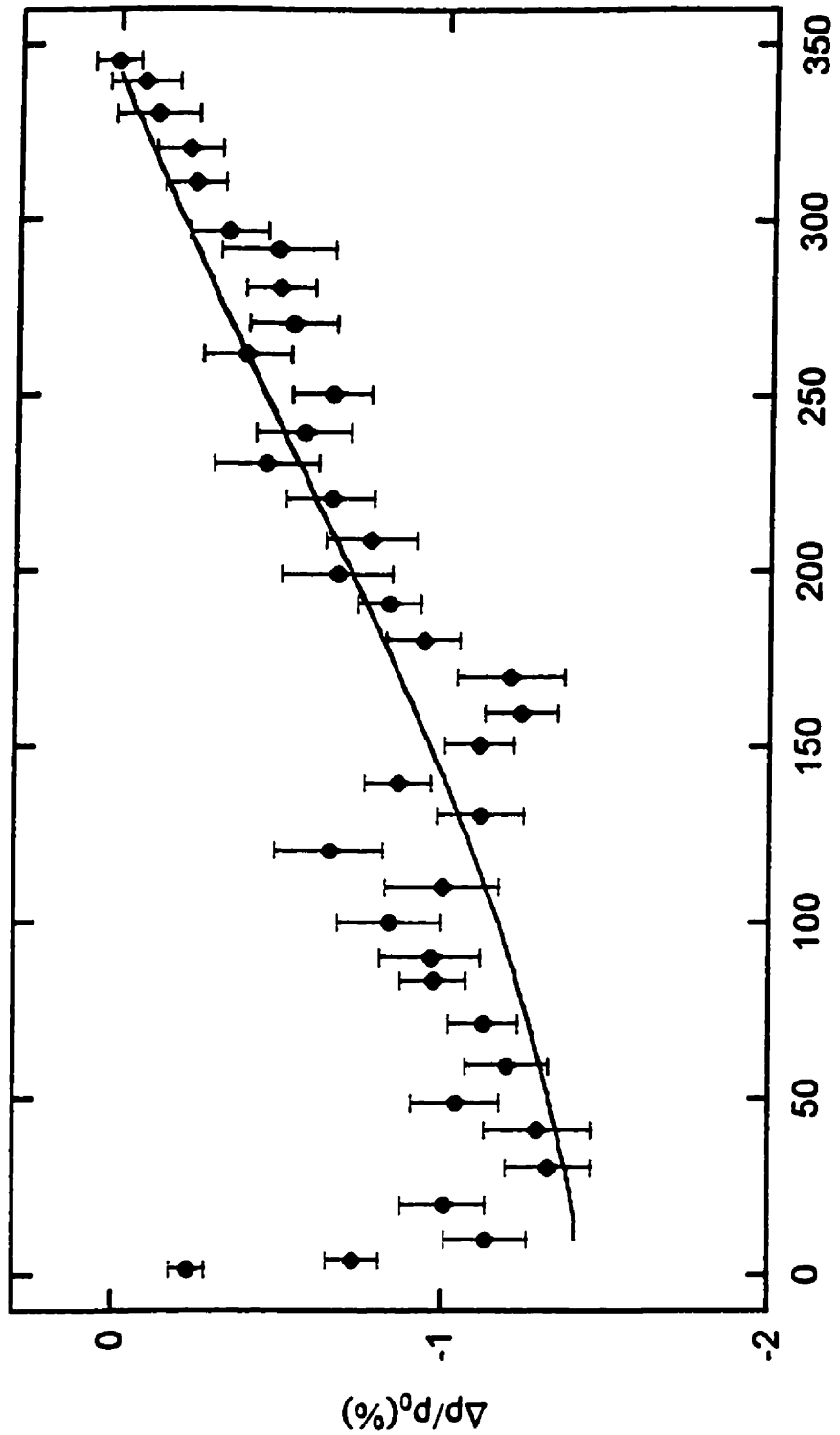

Figure 5.19: The temperature dependence of the estimated SRA ($\Delta\rho/\rho_0$, in %). The solid line is the theoretical model prediction.

is based on an itinerant picture, the so called two current model, which has been utilized widely to describe extensive sets of measurements on dilute alloys based on ferromagnetic transition hosts [59, 27, 30, 29, 60], the second uses the opposite extreme, a localized picture, and has been used principally to interpret the SRA induced in paramagnetic systems such as AuHo by externally applied fields [57].

Both models have been discussed previously (sec:3.7), and their main predictions in the light of the experimental data collected are presented here. Indeed, a recent calculation of the SRA in an itinerant model approach incorporating conduction within the single spin-polarized $e_g \uparrow$ sub-band generally believed to apply to the manganese perovskites yielded [44]

$$\frac{\Delta\rho}{\rho_0} = -\frac{3}{2}\left[\frac{\lambda^2}{(H_{ex}-\Delta_{CF})^2} - \frac{\lambda^2}{\Delta_{CF}^2}\right] \tag{5.19}$$

where λ is spin-orbit coupling constant, H_{ex} the exchange field and Δ_{CF} the crystal field splitting. With the latter estimated at 2 and 1.5 eV respectively and $\lambda \simeq 4\times10^{-2}$ eV, the predicted value for the SRA is -0.85% [44]. The low temperature data displayed in figure (5.19) are in good agreement with this estimate, in both sign and magnitude (SRA = -0.2(1)±0.03% at 4.2 K, essentially the same as at 1.5 K, but climbing abruptly to -1.3±0.1% near 30 K).

Next, the temperature dependence of the SRA is addressed. The low temperature anisotropy is an intraband effect, that is, it arises from the diagonal term ($\lambda L_z S_z$) in the spin-orbit interaction ($\lambda\vec{L}\vec{S} = \lambda L_z S_z + \lambda/2(L^+S^- + L^-S^+)$). The off-diagonal terms involve coupling to the $e_g \downarrow$ sub-band; such processes are inelastic (the man-

ganese perovskites are "strong" ferromagnets) and are frozen out at low temperature. However with increasing temperature some thermal occupation of the $e_g \uparrow$ sub-band likely occurs, particularly as T_c is approached from below and the exchange splitting between spin-up (with resistivity $\rho \uparrow$) and spin-down ($\rho \downarrow$) sub-bands collapses. Furthermore, close to T_c an expansion of the sub-band resistivities in terms of the exchange field H_{ex} leads to [61]

$$\rho \uparrow, \rho \downarrow \simeq \rho(0) \pm sH_{ex} \ldots \tag{5.20}$$

where s is the derivative of the sub-band resistivity with respect to the exchange field, and the profile of both sub-bands has been taken to be similar close to T_c. With s being determined primarily by the slope of the corresponding density of states near the Fermi energy E_F, $(dN/dE)_{E_F}$,

$$\frac{\Delta\rho}{\rho} \sim \frac{(\lambda/\Delta_{CF})^2 (dN/dE)^2_{E_F} H^2_{ex}}{\rho_\uparrow \rho_\downarrow + \rho_{\uparrow\downarrow}(\rho_\uparrow + \rho_\downarrow)} \tag{5.21}$$

in which $\rho_{\uparrow\downarrow}$ represents spin-flip scattering between the two sub-bands. Using collective electron (band) theory in which the thermal average of the magnetization $\langle M \rangle_T$ is proportional to $(T_c - T)^{1/2}$, then in the mean field approximation in which $H_{ex} \propto \langle M \rangle_T$, one obtains

$$\frac{\Delta\rho}{\rho} \propto \frac{(\lambda/\Delta_{CF})^2 (dN/dE)_{E_F} (T_c - T)}{\rho_\uparrow \rho_\downarrow + \rho_{\uparrow\downarrow}(\rho_\uparrow + \rho_\downarrow)}. \tag{5.22}$$

Such an expression can reproduce the essentially linear decrease in the resistive anisotropy between T_c and about 100 K, provided the spin-flip and sub-band resistivities display a weak temperature dependence in this region; this is, however,

an unlikely scenario within currently accepted pictures of the conduction process in the manganese perovskites. Furthermore, while the abrupt decrease exhibited by the SRA below 50 K could be modelled, for example, by some particularly sharp feature in the density of states, such arguments, along with these given above , are obviously qualitative and a realistic comparison between experiment and the predictions of this model would necessitate incorporating realistic band structure details into the several components of equation (5.22) [61].

By contrast, localized models reproduce the linear temperature dependence of the resistive anisotropy immediately below T_c more directly. Briefly, in this model the polarizing field aligns the spin dipole moment ($\vec{S}$) which, through spin-orbit coupling, in turn preferentially orients the orbital component ($\vec{L}$). With $L \neq 0$, the attendant non-spherical charge distribution results in a slightly different (charge) scattering cross-section being experienced by itinerant electrons which constitute the current as the orientation between this current and the field are changed. The analysis is effected by performing a multipole moment expansion of this spherical charge distribution, from which the asymmetry, in lowest order, results from electric quadrupole (D) scattering. The resulting anisotropy ratio is given by [57]

$$\frac{\Delta\rho}{\rho_0} \simeq \left(\frac{D}{V}\right)\left[\left\langle S_z^2\right\rangle - \frac{S(S+1)}{3}\right] \tag{5.23}$$

in which V ($\gg D$) characterizes the residual/zero field resistivity and is usually attributed to deviations in the lattice potential from periodicity in substituted systems. Conduction band details are effectively eliminated by taking this ratio, with the

quadrupole term displaying the expected $(3\cos^2\theta - 1)$ angular variation associated with axial symmetry about a field direction [27].

The solid line in figure (5.19) is a result of calculating $\langle S_z^2 \rangle$ from the S-K model discussed previously [62] using $\eta = 2$ and S = 2; however since the calculation is scaled by the (unknown) ratio (D/V), model parameters cannot be specified from a single data set. Nevertheless this fit clearly provides a good representation of these data over the range 30K to $T_c \simeq 340K$ using reasonable estimates for η and S. However the decrease in the SRA below 30 K clearly cannot be reproduced. The near linear decrease in the resistive anisotropy below T_c is a feature reported in a variety of other amorphous [62] (i.e. high resistivity) and crystalline systems [61], with amorphous $Fe_{90}Zr_{10}$ also displaying a decrease in this ratio at low temperature. However, of more direct relevance is the result that the present data do not display a maximum in the magnitude of the SRA just below T_c where colossal magnetoresistance is present in these systems. This results conflicts with recent reports on LCMO films, although there the anisotropy was estimated from low field data and not the extrapolation procedure utilized here.

Figure (5.20) summarizes the temperature dependence of the isotropic magnetoresistance measured in an applied field of 1.5 T of the same bulk ceramic $La_{0.33}Pb_{0.67}MnO_3$ utilized in all the measurements reported here. This magnetoresistance peaks in the vicinity of T_c as expected, falls to a low value between 200 and 300 K, and then climbs monotonically with decreasing temperature to 1.5 K. If the low field decrease in the

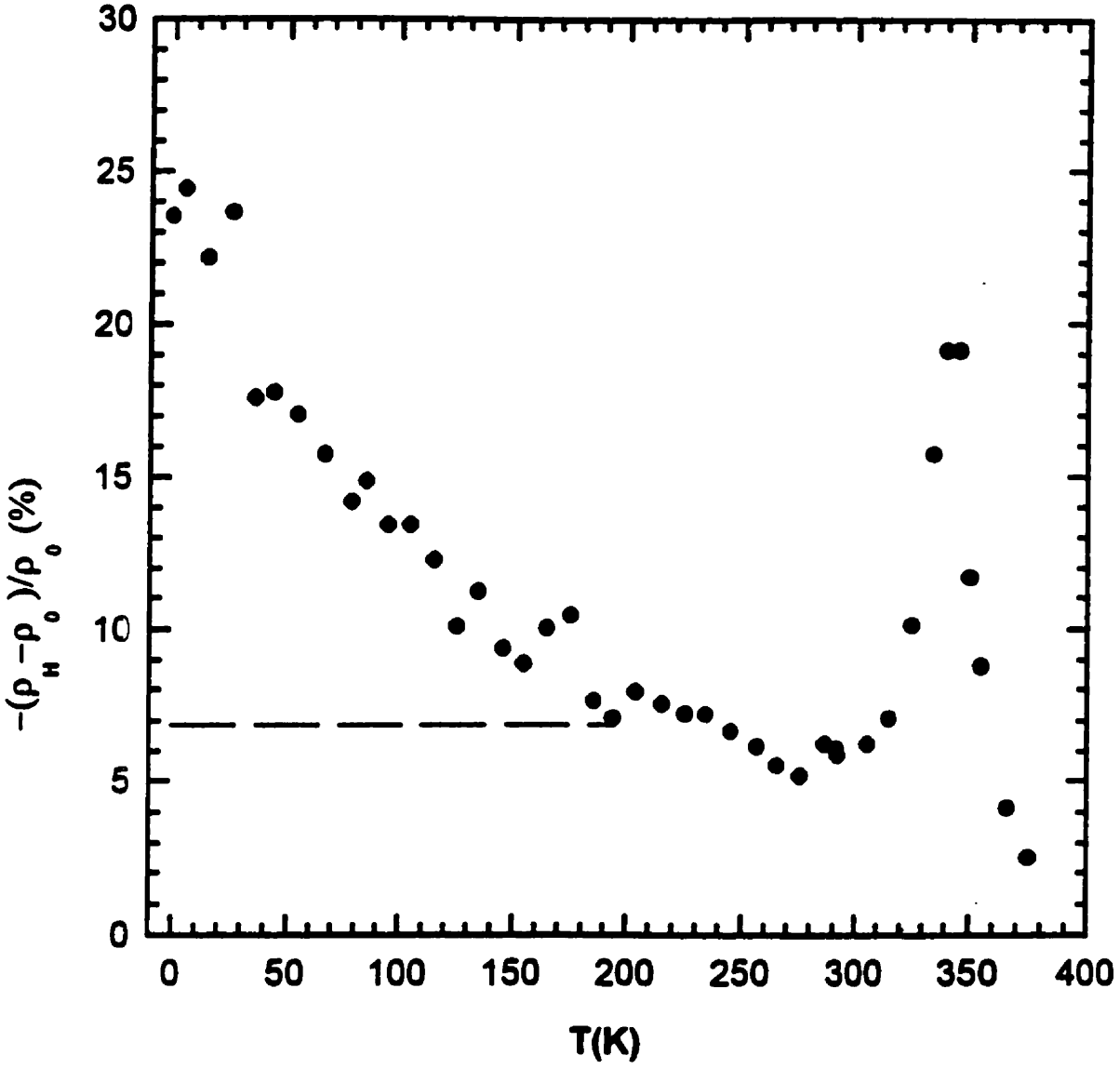

Figure 5.20: The temperature dependence of the isotropic magnetic-resistance measured in an applied field of 1.5T. The dashed line indicates the effect of removing the low field contribution from this ratio.

magnetoresistance discussed previously, and attributed to grain boundary scattering, is subtracted from the data in this figure so that only intrinsic mechanisms are considered [44], then these data remain essentially constant below 200 K as the dashed line indicates. The SRA is also believed to be an intrinsic property of these systems [44]. Indeed the extrapolation procedure used here to estimate this quantity ensures that by removing the low field contribution. Then a comparison between the SRA data in figure (5.19) and isotropic magnetoresistance data in figure (5.20) indicates little correlation between these two effects in this Pb-substituted system. An immediate conclusion that can be drawn from the latter is that the scattering mechanisms that determine the anisotropic magnetoresistance and the (isotropic) colossal magnetoresistance are not necessarily the same in all doped perovskites, a corollary of which would be that the dopant series itself, not just the presence of Mn^{3+} ions, might play some role in these systems.

Chapter 6

Conclusion

The analysis of detailed measurements of the field and temperature dependent magnetization and susceptibility of a ceramic $La_{0.33}Pb_{0.67}MnO_3$ sample confirms the occurrence of a paramagnetic to ferromagnetic phase transition at $T_c = 340.5K$, while the analysis of transport measurements of the same specimen reveal the metal-like ($d\rho/dT > 0$) to insulator-like ($d\rho/dT < 0$) behaviour occurs at $T_c = 339.6K$, very close to the magnetic ordering temperature. This indicates that the transition in the resistivity is related to the magnetic transition, as expected from DE theory. An attempt to estimate the critical exponents describing the paramagnetic to ferromagnetic transition from data acquired closest to the critical point yield

$$\gamma = 1.39 \pm 0.06, \beta = 0.41 \pm 0.02 \text{ and } \delta = 4.2 \pm 0.15.$$

Despite the detailed nature of these measurements, the universality class of the magnetic phase transition of this system remains uncertain. The presence of spin - spin

coupling disorder, indicated by the deviation from the expected power law behaviour when field and/or temperature are varied away from the critical point (and hence the effective exponent values), as well as a significant regular component in the response, all conspire to suggest the possibility that the asymptotic exponents might be those predicted by the 3-dimensional Heisenberg model.

Arguments incorporating various contributions to the exchange coupling indicate that the system studied likely has an exchange coupling distribution which is bimodal. The dominant interaction is double exchange between Mn^{3+} and Mn^{4+} ions, resulting in ferromagnetic order. The other interaction between Mn^{3+} - Mn^{3+} ions, so called $t_{2g} - O(2p_\pi) - t_{2g}$ super exchange , favours antiferromagnetic order. The latter interaction prevails in the regions that are statistically deficient in the dopant species (Pb), while the double exchange and consequently ferromagnetic order are prevalent in the regions statistically rich in the dopant species and thus in Mn^{4+} ions.

Comparing the data to the prediction of the scaling hypothesis, the expected collapse of the experimental data onto a universal curve is present only in the thermally dominated region, i.e. the regime above the cross-over line, while in the field dominated region scaling does not occur. Furthermore a significant regular component obscures the emergence of the critical peaks at relatively low fields, precluding the measurements closer to the critical point ($h \to 0, t \to 0$) and consequently the determination of the asymptotic behaviour is limited.

The transport measurement confirms the presence of an anisotropy in the magnetore-

sistance, indicating the existence of an orbital moment, and thus spin-orbit coupling, at the magnetic site. This result is qualitatively consistent with the presence of Mn^{3+} ions. The spontaneous resistive anisotropy (SRA) has also been measured as a function of temperature, and while the low temperature value for this quantity is in good agreement with a recent itinerant model calculation, the linear decrease in the SRA between T_c and about 30 K is well accounted for in a localized approach.

The temperature dependent isotropic magnetoresistance peaks near the critical temperature as expected. Comparing this with the SRA, (both of which are believed to be an intrinsic property of these systems) indicate little correlation between these two effects, so that the mechanisms controlling the colossal magnetoresistance and SRA in this system appear to be different.

At present the variation in the results reported by different investigators, specifically related to the universality class for the manganites, and the absence of theoretical predictions for the values of the critical exponents for the double exchange ferromagnets, clearly indicate that further theoretical work and experimental measurements are required before the magnetic and transport properties of such substituted perovskites are comprehensively understood.

Bibliography

[1] Jonker G H and Van Santen J H 1950 *Physica***16** 337

[2] Ramirez A P 1997 *J. Phys.: Condens. Matter* **9** 8173

[3] Kaplan T A and Mahanti S D *"Physics of Manganites"* Proc. of the Int. Conf. on Physics of Manganites (New York : Plenum)

[4] Park J H et al 1998 *Phys. Rev. Lett.* **81** 1953

[5] Zener C 1951 *Phys. Rev.* **81** 440

[6] Anderson P W and Hasegawa H 1955 *Phys. Rev.* **100** 675

[7] De Gennes P-G 1960 *Phys. Rev.* **118** 141

[8] Wollan E O and Koehler W C 1995 *Phys. Rev.* **100** 545

[9] Abragam A and Bleaney B *"Electron paramagnetic resonance of transitions"*, Clarendon Press, Oxford (1970)

[10] Inoue J 1998 *J. Phys. D: Appl. Phys.* **31** 643

[11] Millis A J *Nature* **392** 147

[12] Schiffer P et al 1995 *Phys. Rev. Lett.* **75** 3336

[13] Tomioka Y et al 1996 *Phys. Rev.* **B53** R1689

[14] Williams G 1991 *"Magnetic Susceptibility of Superconductors and Other Spin Systems"* ed R A Hein et al (New York: Plenum) p475 et seq

[15] Stanley H E *"Introduction to Phase Transitions and Critical Phenomena"*, Clarendon Press, Oxford (1971)

[16] Plischke M and Bergersen B 1989 *"Equilibrium Statistical Physics"* Prentice-Hall, Inc.

[17] Morrish A H 1965 *"The Physical Principles of Magnetism"* John Wiley & Sons, Inc.

[18] Onsager L 1994 *Phys. Rev.* **65** 117.

[19] Sherrington D and Kirkpatric S 1975 *Phys. Rev. Lett.* **B35** 1792

[20] Southern B W 1976 *J. Phys. C* **9** 4011

[21] Roshko R M and Williams G 1985 *J. Mag. Mag. Mat.***50** 311

[22] Kittel C 1986 *"Introduction to Solid State Physics"* John Wiley &Sons, Inc. New York

[23] Mattheisen A and Vogt G 1964 *Pogg. Ann.* **122** 19

[24] Smit J 1951 *Physica XVI* **6** 613

[25] De Gennes P-G and Friedel J 1958 *J. Phys. Chem. Solids* **4** 71

[26] Fisher M E and Langer J S 1968 *Phys. Rev. Lett.* **20** 665

[27] I. A. Campbell and A. Fert 1982 *"Ferromagnetic materials"* Ch 9 Vol 3. ed. E.P. Wohlforth. North Holland, Amsterdam

[28] Mott N F 1936 *Proc. Roy. Soc.* **A153** 699

[29] Malezemoff A P 1985 *Phys. Rev.* **B32** 6080

[30] Malezemoff A P 1986 *Phys. Rev.* **B34** 1853

[31] Fert A, Asomoza R, Sanchez D H, Spanjaard D and Friederich A 1977 *Phys. Rev.***B16** 5040

[32] Nagai S 1984 *J. Phys. Soc. Jpn.* **53** 3532

[33] Stampe P A et al 1994 *J. Phys: Condensed Matter* **6** 3045

[34] Rao G H, Bärner K and Brown I D 1998 *J. Phys.: Condens. Matter* **10** L757

[35] Muir W B and Ström-Olsen J O 1976 *J. Phys. E* **9** 163

[36] Wang Z 1991 Ph.D. Thesis, University of Manitoba

[37] Osborn J A 1945 *Phys. Rev.* **67** 351

[38] Chikazumi S 1997 *"Physics of Ferromagnetism"*
2nd edition (Clarendon, Oxford) p486

[39] Kunkel H P et al 1988 *Phys. Rev.* **B37** 5880

[40] Urushibara A et al 1995 *Phys. Rev.* **B51** 14103

[41] Roshko R M and Gwyn Williams 1984 *J. Phys. F: Metal Phys.* **14** 703

[42] Le Guillou L C and Zinn-Justin J 1980 *Phys. Rev.* **B21** 3976

[43] Kumar P S A, Joy P A and Date S K 1998 *J. Phys.: Condens. Matter* **10** L487

[44] Ziese M and Sena S P 1998 *J. Phys.: Condens. Matter* **10** 2727

[45] Zhou X Z et al 1997 *Phys. Rev.* **B56** R12714

[46] Kaul S N and Mohan C V 1994 *Phys. Rev.* **B50** 6157

[47] Kornik K et al 1990 *Solid State Commun.* **76** 993

[48] Loewen C and Roshko R M 1985 *Phys. Rev.* **B31** 4663

[49] Fähnle M 1987 *J. Magn. Mater.* **65** 1
Fähnle M and Holey T 1987 *Phys. Stat. Sol. (b)* **141** 253

[50] Ghosh K et al 1998 *Phys. Rev. Lett.* **81** 4740

[51] Wang Z Kunkel H P and Williams G 1992 J. Phys.: Condens. Matter **4** 10385

[52] Wang Z et al 1990 *J. Phys.:Condens. Matter* **2** 4173;

Kunkel H P et al 1989 ibid **1** 3381, 1987 *J. Phys. F.: Metal Phys.* **17** L157

[53] Searle C W and Wang S T 1969 *Can. J. Phys.* **f47** 2703; 1970 ibid **48** 2023

[54] Gupta A et al 1996 *Phys. Rev.* **B54** R15629;

[55] Zhao J H et al 1999 *Phys. Rev.* **59** 8391

[56] Zhang N et al 1997 *Phys. Rev.* **B56** 8138

[57] Freiderich A and Fert A 1972 *Phys. Rev. Lett.* **33** 1214

[58] Li X W et al 1997 *Appl. Phys. Lett.* **71** 1124

[59] Dorleijn J W F 1976 *Phylips Res. Rep.* **31** 287

[60] Campbell I A et al 1970 *J. Phys.* **C3** S595

[61] Stampe P A et al 1995 *Phys. Rev.* **B52** 335;

1994 *J. Phys.: Condens. Matter* **6** 3045

[62] Stampe P A et al 1993 *J. Phys.: Condens. Matter* **5** L625